

High-order electromechanical couplings in ferroelectrics

THÈSE N° 6266 (2014)

PRÉSENTÉE LE 15 JUILLET 2014

À LA FACULTÉ DES SCIENCES ET TECHNIQUES DE L'INGÉNIEUR
LABORATOIRE DE CÉRAMIQUE
PROGRAMME DOCTORAL EN SCIENCE ET GÉNIE DES MATÉRIAUX

ÉCOLE POLYTECHNIQUE FÉDÉRALE DE LAUSANNE

POUR L'OBTENTION DU GRADE DE DOCTEUR ÈS SCIENCES

PAR

Alexander KVASOV

acceptée sur proposition du jury:

Prof. H. Hofmann, président du jury
Prof. A. Tagantsev, directeur de thèse
Prof. J. Hlinka, rapporteur
Prof. I. Kornev, rapporteur
Prof. N. Marzari, rapporteur



ÉCOLE POLYTECHNIQUE
FÉDÉRALE DE LAUSANNE

Suisse
2014

"Gravitation is not responsible for people falling in love."
– Albert Einstein

To Bárbara...

Acknowledgements

I would like to express my high gratitude to my thesis director Prof. Alexander Tagantsev who guided me throughout my thesis. Always available for discussion, always ready to help and explain, he taught me how to solve the problems and moreover how to solve difficult problems myself. His profound understanding and knowledge of almost all areas of physics in combination with his unique talent of explaining complex problems and ideas in a simple way makes him not only an excellent scientist, but also a very good supervisor. Without him this work would never have been accomplished.

I would like to thank the members of my thesis jury: Prof. Heinrich Hofmann (EPFL), Prof. Nicola Marzari (EPFL), Prof. Igor Kornev (École Centrale Paris) and Prof. Jirka Hlinka (Institute of Physics, Academy of Sciences of the Czech Republic)

I also would like to thank people from Ceramics Laboratory, especially Arnaud Crassous, Leo Mc Gilly, Maxim Gureev, Kaushik Vaideeswaran, Peter Yudin, many others, for interesting and useful discussions in the lab and even more interesting free time out of the lab.

I want to acknowledge people from THEOS laboratory especially Dr. Giovanni Pizzi and Prof. Nicola Marzari for their valuable help with the first principals calculations.

I am thankful to the secretary of the doctoral school Erika Menamkat and the secretary of LC Yuko Kagata who were always very friendly and ready to help.

I am grateful to all my friends for their support in different aspects of my life during my PhD study.

Finally, I would like to thank my family and, of course, Barbara, without whom my life would never be the same.

Lausanne, 24 April 2014

A.K.

Abstract

The thesis deals with electromechanical phenomena in ferroelectrics. High-order electromechanical couplings, in contrast to the ordinary low-order electrostrictive coupling (coupling which is linear in deformation and quadratic in polarization), were usually neglected in theoretical consideration. This thesis will be focused on the investigation of the systems where these couplings are of importance, e.g. ferroelectric thin films, tunable Film Bulk Acoustic wave Resonators (FBARs), and problems involving the flexoelectric effect. This work was accomplished through a combination of two approaches: ab initio methods and phenomenological Landau theory.

We demonstrate that high-order electromechanical couplings are of importance for strained ferroelectric films. It is shown that theoretical methods can suffer from a substantial inaccuracy unless these higher-order electromechanical interactions are taken into account. This statement is illustrated with an example of a temperature - misfit strain phase diagram of a BaTiO₃ (BTO) thin film derived with high-order electromechanical interactions evaluated with the help of first principles calculations.

Another domain where high-order electromechanical interactions are important is tunable FBARs, where the antiresonance frequency tuning is governed by the high-order electromechanical coefficient. The non-linear electrostrictive coefficient was for the first time calculated for BTO and SrTiO₃ (STO) using ab initio methods. Then, taking into account the small difference of obtained values for BTO and STO these results were linearly interpolated to the Ba_xSr_{1-x}TiO₃ (BST) compositions. The obtained values are consistent with previously made order-of-magnitude estimates. Using parameters obtained with first principles calculations, we simulate the resonance behaviour of BST based tunable FBARs. Resulting antiresonance tuning is smaller than expected due to the compensation of two competing terms conditioned by linear and non-linear electrostrictions. Our calculations also confirm that, for tunable FBAR modeling, it is important to use a polarization-based Landau free energy expansion taking into account both non-linear electrostriction and background permittivity.

It is demonstrated that for classical perovskites in the paraelectric phase, such as BTO, STO, and PbTiO₃ (PTO), electrostrictive strain induced by an electric field may not obey traditionally considered "extension along the field and contraction perpendicular to it" behaviour if the applied electric field is directed obliquely to the cubic crystallographic directions. A remarkable behaviour is predicted for bars of bulk BTO, STO, and PTO cut along the [111] crystallographic cubic direction. In this case, for an electric field parallel to the bar, some expansion along all its three dimensions is expected. The situation with the [110] cut is also unusual, the electrostrictive

Abstract

tive effect from a field along the bar will result in a contraction in one transversal direction and an expansion in the other. In terms of the effective "polarization-strain" electrostrictive coefficients of the sample, this means a positive transversal electrostriction coefficient for some sample orientations.

The related effects take place in differently oriented perovskite thin films. Here, we identify the manifestation of the angular dependence of electrostriction in the phase diagrams of thin films with the example of BST 30/70. We study the behaviour of the ferroelectric phase transition temperature of the film depending on its orientation. It was found that, for some film orientations, the phase transition temperature can be less than that in the bulk material. Ferroelectric properties of materials can be markedly changed through strain engineering, therefore the use of the thin films grown in different orientations gives more flexibility for engineering and provides a broader range of operating temperatures.

The flexoelectric effect is a response of electric polarization to a mechanical strain gradient. It represents a higher-order effect with respect to piezoelectricity. Often this effect can be neglected, however, at the nanoscale, where large strain gradients are expected, the flexoelectric effect becomes appreciable. A significant number of recent publications devoted to flexoelectricity shows an increasing interest in the phenomenon. In this work, we demonstrate the possibility of the extraction of the bulk flexoelectric tensors from the phonon spectrum. For this, we exploit a model phonon spectrum of STO, which was calculated using first principles methods. The dynamic flexocoupling coefficient, which was customarily not taken into account, but which gives a substantial contribution to the total flexocoupling coefficient, was for the first time obtained using ab initio calculations.

Finally, antiphase domain boundaries (APB) in antiferroelectric PbZrO_3 are studied using ab initio full relaxation calculations. Following transmission electron microscopy experiments, where the polarity in APB was originally found, our calculations confirm the presence of local polarity and, moreover, show the bistability of the APB structure. Taking into account the above results, one can conclude that the phenomenon observed at the APB is a signature of local ferroelectricity. Ferroelectric APBs in antiferroelectrics are of high interest since they can be potentially viewed as functional 1-10 nm wide elements, which carry the information.

Key words: ferroelectrics, ferroelectricity, flexoelectricity, thin films, electrostriction, Landau theory, ab initio calculations

Résumé

Cette thèse traite des phénomènes électromécaniques dans les ferroélectriques. Les couplages électromécaniques d'ordre élevé, au contraire du couplage électrostrictif de bas ordre (couplage linéaire avec la déformation et quadratique avec la polarisation) sont généralement négligés dans les modèles théoriques. Cette thèse se concentre sur l'étude des systèmes dans lesquels ces couplages sont importants, tels que les films minces ferroélectriques et les résonateurs acoustiques ajustables, et les problèmes impliquant l'effet flexoélectrique. Ce travail a été réalisé en combinant deux approches : des calculs *ab initio* et la théorie phénoménologique de Landau.

Nous avons démontré que les couplages électromécaniques d'ordre élevé sont importants pour les films ferroélectriques contraints, et que les modèles théoriques utilisés peuvent souffrir d'imprécisions substantielles à moins de les prendre en compte. Cette affirmation est illustrée par un diagramme de phases de la température en fonction de la contrainte épitaxiale de films minces de BaTiO₃ (BTO). Celui-ci a été calculé à l'aide des couplages électromécaniques d'ordre élevé à partir de calculs des premiers principes.

Un autre domaine dans lequel les interactions électromécaniques d'ordre élevé sont importantes est les résonateurs acoustiques ajustables pour lesquels ils contrôlent la fréquence d'antirésonance. Le coefficient électrostrictif non-linéaire a été calculé pour la première fois pour BTO et SrTiO₃ (STO) en utilisant des méthodes *ab initio*. En prenant en compte les faibles différences de valeurs pour BTO et STO, les résultats ont ensuite été linéairement interpolés pour les compositions de Ba_xSr_{1-x}TiO₃ (BST). Les valeurs obtenues concordent avec les estimations faites précédemment. En utilisant les paramètres obtenus à partir des calculs des premiers principes, nous avons simulé le comportement à la résonance de résonateurs ajustables à base de BST. L'ajustement de l'antirésonance dans ce système est plus faible qu'attendu à cause de la compensation de deux termes en compétition qui sont conditionnés par l'électrostriction linéaire et non-linéaire. Nos calculs confirment aussi que pour modéliser un résonateur acoustique ajustable, il est important d'utiliser le développement de l'énergie libre de Landau en prenant en compte à la fois l'électrostriction non-linéaire et la permittivité. Il a été démontré que pour les perovskites classiques dans leur phase paraélectrique, telles que BTO, STO et PbTiO₃ (PTO), la contrainte électrostrictive induite par un champ électrique n'obéit pas nécessairement au comportement traditionnel « extension le long du champ et contraction perpendiculairement à celui-ci » si le champ est appliqué de façon oblique aux axes cristallographiques cubiques. Un comportement remarquable est prédit pour des barres de matériaux massifs de BTO, STO et PTO découpées le long de l'axe cristallographique cu-

bique [111]. Pour un champ électrique appliqué parallèle à la barre, une extension dans les trois dimensions est attendue. Le cas d'une découpe suivant l'axe [110] est aussi inhabituel, l'effet électrostrictif pour un champ appliqué le long de la barre résulte en une contraction suivant une des directions transverses et à une extension suivant l'autre. En termes de coefficients électrostrictifs effectifs « polarisation-contrainte » de l'échantillon cela signifie que certains sont positifs pour des orientations données.

Des effets similaires se produisent dans des films minces de perovskites. Ici, nous identifions la manifestation de la dépendance angulaire de l'électrostriction dans les diagrammes de phases de films minces en prenant comme exemple BST30/70. Nous avons étudié le comportement de la température de transition de phase ferroélectrique en fonction de l'orientation du film. Nous avons trouvé que pour certaines orientations, la température de transition de phase peut être inférieure à celle du matériau massif. Les propriétés ferroélectriques du matériau peuvent être notablement modifiées en ajustant la contrainte. Le choix de l'orientation du film pendant sa croissance permet d'ajuster ses propriétés et d'augmenter sa plage opérationnelle de températures.

L'effet flexoélectrique est la réponse de la polarisation électrique à un gradient de contrainte. Il est d'ordre plus élevé que l'effet piézoélectrique et est souvent négligé. A l'échelle nanométrique cependant, ou des gradients importants sont attendus, l'effet flexoélectrique devient non négligeable. Nombre de publications récentes lui sont dévouées ce qui confirme l'intérêt croissant pour le phénomène. Dans cette thèse, nous démontrons la possibilité d'extraire les coefficients flexoélectriques des spectres de phonons. Pour cela nous exploitons le spectre de phonons de STO, calculé à partir de calculs fondamentaux. Le coefficient dynamique de flexocouplage, qui n'est habituellement pas pris en compte, donne une contribution substantielle au coefficient flexoélectrique total et a été calculé pour la première fois en utilisant une méthode *ab initio*.

Finalement, les parois de domaines d'antiphase (PDA) de l'antiferroélectrique PbZrO_3 sont étudiées en utilisant des relaxations complètes *ab initio*. En partant des observations par microscopie électronique à transmission, où la polarité des PDA a originellement été trouvée, nos calculs confirment la présence d'une polarité locale et, de plus, révèlent une bistabilité de la structure des PDA. En prenant en compte ces résultats, nous avons conclu que le phénomène observé est la signature d'une ferroélectricité locale. Les parois de domaines d'antiphase dans les antiferroélectriques sont particulièrement intéressantes car elles peuvent potentiellement être vues comme des porteuses d'information de seulement 1-10nm de large.

Mots clefs: ferroélectriques, ferroelectricité, flexoelectricité, films minces, electrostriction, théorie de Landau, simulations *ab initio*

Contents

Acknowledgements	v
Abstract (English)	vii
Résumé (Français)	ix
Contents	xii
List of figures	xix
List of tables	xxii
Table of Notations	xxiii
Introduction	1
1 State of the art	7
1.1 Non-linear electrostrictive couplings and strain engineering	7
1.2 Flexoelectric effect	8
2 Can we trust thin film diagrams?	13
2.1 Strain engineering	13
2.2 Scalar model	14
2.3 Landau theory of thin films with high-order electrostrictive couplings	16
2.4 Legendre transformation of high-order electrostrictive coefficients	17
2.5 Thin film phase diagrams	20
2.6 Bulk - thin film renormalization of high-order coefficients	20
2.7 Ab initio calculations	22
2.8 Experimental estimates of R coefficients	26
2.9 Results and discussion	27
2.10 Conclusions	30
3 FBARs tuning from first principles	31
3.1 Introduction to Film Bulk Acoustic wave Resonators	31
3.2 Description of FBARs tuning	33
3.3 Ab initio calculations	36

Contents

3.4	Results and discussion	39
3.5	Conclusions	43
4	Positive effective electrostrictive coefficients in perovskites	45
4.1	Effective electrostrictive coefficients in perovskite crystals	46
4.2	Effective electrostrictive coefficients in perovskite thin films	49
4.3	Conclusions	55
5	Flexoelectric effect	57
5.1	Description of the bulk flexoelectric effect in crystals	57
5.1.1	Static flexoelectric effect	58
5.1.2	Dynamic flexoelectric effect	59
5.2	Determination of flexoelectric tensors using phonon dispersion	61
5.2.1	Introduction	61
5.2.2	Ab initio calculations of phonon dispersion curves	64
5.2.3	Results	66
5.3	Determination of flexoelectric tensors using lattice dynamics	71
5.3.1	Introduction	72
5.3.2	Ab initio calculations of interatomic force constants	74
5.3.3	Results	74
5.4	Discussion and comparison with experiment	78
5.5	Conclusions	79
6	Ferroelectric antiphase boundaries in antiferroelectric materials	81
6.1	Introduction	81
6.2	Theory of ferroelectricity in antiferroelectric domain walls	82
6.2.1	Antiphase boundaries in lead zirconate - candidates for ferroelectricity .	83
6.2.2	The thickness of antiphase boundaries in ferroics	85
6.3	Electron microscopy experiments	88
6.4	Ab initio simulations	91
6.4.1	Ab initio calculations of bulk lead zirconate	92
6.4.2	Ab initio calculations of APB in lead zirconate	92
6.5	Discussion	94
7	Conclusions and Outlook	97
7.1	Conclusions	97
7.2	Outlook	99
	Bibliography	109
	List of publications	111
	Curriculum Vitae	113

List of Figures

1	Perovskite structure of ABO_3 on example of $BaTiO_3$. The material can exist in different phases: (a) cubic phase, (b) tetragonal phase, (c) orthorhombic phase, and (d) rhombohedral phase. The direction of polarization in different phases is shown with the green arrow.	2
2	Perovskite ABO_3 unit cell of $BaTiO_3$ illustrating 180° polarization reversal for two of the six possible polarization states of the tetragonal phase produced by displacement of the central cation in the tetragonal phase.	3
1.1	Temperature - misfit strain phase diagrams of a single-domain (001)-oriented $BaTiO_3$ taken from Ref. [1]. The phases are denoted as (i) the c-phase, polarization is out-of-plane ($P_1 = P_2 = 0, P_3 \neq 0$); (ii) the aa-phase, where polarization is in-plane ($P_1 \neq 0, P_2 \neq 0, P_3 = 0$); (iii) the ac-phase where $P_1 \neq 0, P_2 = 0, P_3 \neq 0$; (iv) r-phase, where all components of polarization are non-zero; and (v) paraelectric phase, polarization is 0.	8
1.2	PFM (Piezoresponse Force Microscopy) images illustrating the impact of stress on polarization switching behaviour of the (111)-oriented PZT capacitors, taken from Ref. [2]. (a) and (b) - images of PFM amplitude and phase after tensile stress application, (c) and (d) - PFM amplitude and phase after compressive stress application.	10
1.3	Diagrammatic sketch of a flexoelectric piezoelectric composite made of truncated pyramidal blocks of BST ceramics. Taken from Ref. [3].	11
2.1	Modeled stress σ_1 on strain ϵ_1 dependence for $BaTiO_3$. Obtained with VASP keeping the mmm symmetry of the structure.	24
2.2	Modeled stress σ_1 on strain ϵ_1 (a) and square of polarization P_1^2 on strain ϵ_1 (b) dependences for $BaTiO_3$. Obtained with VASP full relaxation calculations keeping the $4mm$ tetragonal symmetry of the structure.	25

2.3	Temperature - misfit strain phase diagrams of a single-domain (001)-oriented BaTiO ₃ . ϵ_0 - biaxial parent misfit strain, T - temperature. The phases are denoted as (i) the c-phase (yellow), polarization is out-of-plane ($P_1 = P_2 = 0, P_3 \neq 0$); (ii) the aa-phase (red), where polarization is in-plane ($P_1 \neq 0, P_2 \neq 0, P_3 = 0$); (iii) the ac-phase (brown) where $P_1 \neq 0, P_2 = 0, P_3 \neq 0$; (iv) r-phase (red), where all components of polarization are non-zero; and (v) paraelectric phase (blue), polarization is 0. (a) Original Pertsev's diagrams built with coefficients from Ref. [1]. (b) Developed with coefficients set from Ref. [1] appended with high-order M_{ijklmn} , R_{ijklmn} and N_{ijklmn} coefficients. The hatched regions demonstrate the shift of the transition lines within the error bars of the coefficients.	29
3.1	A schematic drawing of the TE mode resonator. The DC bias E^{DC} and polarization P^{DC} is parallel to the direction of the traveling acoustic wave with the wave vector k	33
3.2	Modeled stress σ_1 on strain u_1 (a) and square of polarization P_1^2 on strain u_1 (b) dependences in the vicinity of zero strain for SrTiO ₃ . Obtained with VASP full relaxation calculations keeping the $4mm$ tetragonal symmetry of the structure.	38
3.3	Modeled dependences of resonance (a) and antiresonance (b) frequency tuning on relative tunability n_r for the tunable FBAR using the [001]-oriented thin film of different BST compositions. Parameters used in calculations like stiffness, linear and non-linear electrostriction are taken from Table 3.1. Other used parameters are taken from Ref. [4]: $\alpha = \frac{1}{\epsilon_0} \frac{T-T_0(x)}{C_{CW}(x)}$, $T = 300\text{K}$, $T_0(x) = (42 + 439.37x - 96x^2)\text{K}$, $C_{CW}(x) = (0.86 + 1.1x^2)10^5\text{K}$, $\beta = 8(1 - x)10^9 \frac{\text{m}^5}{\text{C}^2\text{F}}$, and $\epsilon_b = 7\epsilon_0$	41
3.4	Modeled dependences of the antiresonance frequency tuning on relative tunability n_r for the tunable FBAR using the [001]-oriented thin film of BST with $x = 0.25$. Dashed lines show the antiresonance behaviour without taking into account m_{111} and the behaviour resulting from "D-expansion" of Landau free energy.	42
3.5	Modeled dependences of the resonance (a) and antiresonance (b) frequency tuning on applied DC bias for the tunable FBAR using the [001]-oriented thin film of different BST compositions. Parameters used in calculations like stiffness, linear and non-linear electrostriction are taken from Table 3.1. Other used parameters are taken from Ref. [4]: $\alpha = \frac{1}{\epsilon_0} \frac{T-T_0(x)}{C_{CW}(x)}$, $T = 300\text{K}$, $T_0(x) = (42 + 439.37x - 96x^2)\text{K}$, $C_{CW}(x) = (0.86 + 1.1x^2)10^5\text{K}$, $\beta = 8(1 - x)10^9 \frac{\text{m}^5}{\text{C}^2\text{F}}$, and $\epsilon_b = 7\epsilon_0$	43
4.1	Direction of polarization described by angle θ and the rotated reference frame (x'_1, x'_2, x'_3) associated with it. The polarization direction changes in plane going from [001] to [111] and then to the [110] direction.	46

4.2	Effective Q_{11}^{θ} coefficient as a function of the cut direction θ for three perovskites materials BaTiO ₃ (pink), SrTiO ₃ (blue) and PbTiO ₃ (green). The data for electrostrictive constants are taken from Table 4.1.	49
4.3	Dependence of $\frac{Q_{12}^{\theta}}{Q_{11}^{\theta}}$ ratio on the cut direction θ . Q_{11}^{θ} - longitudinal effective electrostrictive coefficient, $Q_{12}^{\theta(1)}, Q_{12}^{\theta(2)}$ - two transversal effective electrostrictive coefficients (see (4.4)). (a) plotted for BaTiO ₃ with coefficients from [5]. (b) for SrTiO ₃ from [6]. (c) for PbTiO ₃ from [1].	50
4.4	Experimental dependance of out-of-plane permittivity on temperature of two BST 30/70 thin films of (111) and (100) orientations. Provided by Yamada Tomoaki, Tokyo Institute of Technology, Japan	51
4.5	Orientation of the film described by the normal to the film plane which differs from [001] crystallographic axis by angle θ . The rotated reference frame (x'_1, x'_2, x'_3) is associated with the film with Ox'_3 axis parallel to the normal.	52
4.6	Schematically shown thin film temperature - misfit strain phase diagrams for different film orientations of BST 30/70 film. θ - orientation (deposition) angle of the thin film with respect to [001] crystallographic axis. Parameters (T_C, Q_{ij}, s_{ij} , etc.) of bulk BaTiO ₃ and SrTiO ₃ materials were as taken from [5–7] and interpolated for BST 30/70.	53
4.7	Ferroelectric phase transition temperature depending on the film orientation under the compressive strain of 0.8% for BST 30/70 thin film. θ - orientation (deposition) angle of the thin film with respect to [001] crystallographic axis. Parameters (T_C, Q_{ij}, s_{ij} , etc.) of bulk BaTiO ₃ and SrTiO ₃ materials were as taken from [5–7] and interpolated for BST 30/70.	54
5.1	Temperature dependence of dispersion curves for transverse acoustic (TA) and soft-mode optic (TO) phonons with wavevector $q = \frac{\pi}{a}(\xi, 0, 0)$ in KTaO ₃ , where a is the lattice constant. Taken from ref. [8].	62
5.2	Calculated phonon dispersion of transverse acoustic (TA) and soft-mode transverse optic (TO) branches with wavevector $q = \frac{\pi}{a}(\xi, 0, 0)$ for cubic SrTiO ₃ stabilized by pressure. The blue lines correspond to the lower pressure ($p = 69$ kBar, $a = 3.89$ Å) when the flexoelectric interaction between the TO and TA branches is strong and one can observe lowering of the TA. The grey lines correspond to the high pressure ($p = 135$ kBar, $a = 3.85$ Å) when the interaction is weak.	65

List of Figures

- 5.3 Calculated dependence of square of phonon frequency on square of wave vector of transverse acoustic (TA) and soft-mode transverse optic (TO) branches with wavevector $q = \frac{\pi}{a}(\xi, 0, 0)$ for cubic SrTiO₃ stabilized by pressure. Blue and red lines correspond to the hydrostatic pressure 69 kBar and 135 kBar correspondingly. The red TO branch (high pressure) is out of the figure. 67
- 5.4 The lhs of the expression (5.30) with the ω corresponding to the TA branch with wavevector $q = \frac{\pi}{a}(\xi, 0, 0)$ for cubic SrTiO₃ stabilized by 69 kBar hydrostatic pressure. Blue and purple curves correspond to the "+" and "-" signs in (5.30), correspondingly. The dashed lines are tangent lines, which were used to find M coefficient. 68
- 5.5 Calculated dependence of square of phonon frequency on square of wave vector of transverse acoustic (TA) and soft-mode transverse optic (TO) branches for cubic SrTiO₃ for direction [110], $q = \frac{\pi}{a}(\xi, \xi, 0)$. The two modes, with displacement and polarisation vectors parallel to [001] direction (TA1 and TO1) and with displacement and polarisation vectors parallel to $[1\bar{1}0]$ (TA2 and TO2), are shown with orange and green colours correspondingly. 69
- 5.6 Calculated dependence of square of phonon frequency on square of wave vector of transverse acoustic (TA) and soft-mode transverse optic (TO) branches for cubic SrTiO₃ for direction [111], $q = \frac{\pi}{a}(\xi, \xi, \xi)$. Green lines correspond to the low pressure ($p = 69$ kBar), black lines - high pressure ($p = 135$ kBar). 70
- 5.7 Convergence of IFCs (a) and momentum of IFCs (b) with the cell number n_1 . $\Phi_{11,11}^{(n_1,0,0)-(0,0,0)}$ represents a IFC between atom "1" (Sr) in the direction Ox_1 sitting in the $(n_1, 0, 0)$ cell and second atom "1" in the direction Ox_1 being in the "central" $(0, 0, 0)$ cell. $R_p^{(n_1,0,0)}$ is a radius vector to p -th atom in the $(n_1, 0, 0)$ cell. $n_1 = \pm 5$ corresponds to a cell at the edge of supercell. 75
- 5.8 Convergence of momentum of IFCs with the cell number n_1 . $\Phi_{11,11}^{(n_1,0,0)-(0,0,0)}$ represents a IFC between atom "1" (Sr) in the direction Ox_1 sitting in the $(n_1, 0, 0)$ cell and second atom "1" in the direction Ox_1 being in the "central" $(0, 0, 0)$ cell. $R_p^{(n_1,0,0)}$ is a radius vector to p -th atom in the $(n_1, 0, 0)$ cell. $n_1 = \pm 5$ corresponds to a cell at the edge of supercell. (a) the moments of the edge cells are counted in the sum (5.50), (b) the moments of the edge cells are counted with the factor 1/2, (c) the moments of the edge cells are not counted. 77

- 6.1 Structure of lead zirconate. a. The cubic unit cell. Lattice modes relevant to the phase transition into the orthorhombic phase; b. Lead displacements in the Σ -mode. c. Oxygen-octahedron rotations in the R -mode. In b and c, the projections of the orthorhombic unit cells onto the ab plane (rectangles) are shown. The crystallographic axes of the orthorhombic phase ($[100]$ and $[010]$) and of the pseudo-cubic phase (x_c and y_c) are shown. 83
- 6.2 Mapping of the translational domain states and boundaries inside a single orientational domain of PbZrO_3 onto the plane of the complex order parameter. Circles - translational domain states. Lines - translational boundaries. The boundaries linking the domain state marked by empty circle with the other states are shown with numbered lines. (a) Naturally expected translational boundaries. The phase shifts $\Delta\phi$ of the modulation of the lead displacements in the walls are: line 1 - the $\pi/2$ wall, $\Delta\phi = \pi/2$; lines 2 and 3 - the π walls (antiphase boundary), $\Delta\phi = \pi$; line 4 - the $3/2\pi$ wall, $\Delta\phi = 3/2\pi$. In the π -wall (line "3") the order parameter passes through zero. In view of the above discussion, in such wall the suppressing effect of the order parameter on the ferroelectric instability is minimal making the π -wall the most favorable for the occurrence of local ferroelectricity. (b) Mappings of possible $\pi/2$ walls onto the plane ($\text{Re } \xi, \text{Im } \xi$) of the complex amplitude of the order parameter in PZ - solid lines 1 and 2. Mappings of possible ferroelectric walls onto the plane (q_1, q_2) of the two-component order parameter in GMO - solid lines 1 and 2. 85
- 6.3 Antiphase boundary (APB) in a "non-ferroic" vs. APB in a ferroic. (a) 2D schematic of an APB in a "non-ferroic". Here only one chain of atoms parallel to the Ox direction is shown and the whole 2D "crystal" can be obtained by repeating this chain in the Oy direction with a period c . Regions "domain I" and "domain II" have both a perfect crystalline structure with period a . Yet, in order to superpose elementary cell of region I onto region II, a vector is needed, which differs from a translational vectors by $a/2$. This vector does not belong to the set of elementary lattice translation vectors of the structure, all equal na , n being integer numbers. The antiphase boundary w_1 is marked grey and its width is about $a/2$. (b) 2D schematic of a structural phase transition in a ferroic. In each phase, only one chain of atoms is shown; the whole 2D "crystal" can be obtained by repeating the chain in the perpendicular direction with the period c . At the transition, the period in the direction of the chain changes from $a/2$ to a . (c) Schematic of an APB in the 2D ferroic introduced in Fig. 6.2(b). The thickness of the APB consistent with its primary definition (*definition-0*) is w_3 . According to *definition-1* one would attribute to the APB the thickness w_2 86

List of Figures

- 6.4 Morphology of translational boundaries in the antiferroelectric PZ crystal. (a) Dark-field image with superposed orthorhombic axes shows morphology of the translational boundaries (dark lines). Topological features of these boundaries are marked by the red circles: "1" - annihilation of two antiphase boundaries (APBs), "2" - annihilation of one APB and two $\pi/2$ walls, and "3" - split of an APB into two $\pi/2$ walls. (b) Atomic-resolution image of an APB between two translational domains recorded under NCSI conditions with the incident electron beam parallel to the [001] direction. In two domains, two identically defined orthorhombic unit cells are highlighted. Lead atom displacements are represented in the schematic orthorhombic blocks to the left (domain I) and the right (domain II) of the image. By shifting the orthorhombic cell, the APB (the shaded cyan area) can be evidenced by the conflict of half a unit cell in between these two domains. The scale bar in (a,b) is 200 nm and 1 nm, respectively. 89
- 6.5 Atomic displacements of translational boundaries in the antiferroelectric PZ crystal. (a) and (b) displacements of Pb and Zr atoms with respect to the atomic positions of the cubic phase, averaged over the planes along x direction as function of the plane positions along y direction. Blue squares: in-plane (the x direction, [100] in Fig. 6.1) displacements parallel to the wall; pink circles: out-of-plane (the y direction, [010] in Fig. 6.1) displacements normal to the wall. (c) Dipole moment density obtained by averaging the dipole moments of a "sliding" orthorhombic unit cell plotted as a function of the centers of the sliding cells. Red squares: in-plane polarity; green circles: out-of-plane polarity. 90
- 6.6 Schematic diagram of the "sliding" orthorhombic unit cell. Based on the structure model derived from the image simulation, the spontaneous polarization is calculated for each unit cell, then the cell is shifted by $b/4$ 91
- 6.7 Calculated bulk structure of PZ. The calculations reproduce the features of the real material such as antiparallel lead atom displacements and antiphase correlated rotation of the oxygen octahedra. The displacements of Pb atoms are schematically shown with arrows. 92
- 6.8 Ab initio calculation of antiphase boundary in PZ. The two end cells of the supercell have a fixed orthorhombic structure corresponding to that of the PZ inside the adjacent domains. The inner 3.5 orthorhombic cells are relaxed. The displacements of Pb atoms are schematically shown with arrows. 93
- 6.9 Results of ab initio calculations. (a) and (b) Displacements of Pb and Zr atoms with respect to the atomic positions of the cubic structure, squares: in-plane (x direction) displacements parallel to the wall, circles: out-of-plane (y direction) displacements normal to the wall. (c) Dipole moment density for the "sliding" orthorhombic unit cell plotted as a function of the centers of the sliding cells; squares: in-plane polarity, circles: out-of-plane polarity. 94

6.10 Pb atom displacements from cubic positions along [100] direction in the APB region. There are 2 equivalent configurations (a) and (b) corresponding to the same energy confirming the bistability of the structure. 95

List of Tables

- 2.1 Some experimental material parameters of BaTiO₃. d_{ij} - piezoelectric coefficients, the values are taken from Ref. [9]. ϵ_{S_i} is the spontaneous strain, $\epsilon_{S3} = \frac{c-a_0}{a_0}$ and $\epsilon_{S1} = \frac{a-a_0}{a_0}$, where $c = 4.034 \text{ \AA}$ and $a = 3.992 \text{ \AA}$ are the lattice parameters of the tetragonal cell, $a_0 = 4.003 \text{ \AA}$ is the lattice constant of cubic BaTiO₃ extrapolated to room temperature [10], ϵ_{S5} is recalculated from the distortion angle $\beta = 89^\circ 51.6'$ [10] of orthorhombic cell. Q_{ij} and R_{ijk} are linear and non-linear electrostriction calculated from experimental data. 27
- 2.2 Some materials parameters of BaTiO₃ obtained from ab initio calculations. s_{ij} and N_{ijk} are linear and nonlinear elastic compliance, Q_{ij} and M_{ijk} are linear and high-order electrostrictive tensors respectively. Experimental values of c_{ij} (from [7]) and Q_{ij} (from [1]) are also given for comparison. 28
- 2.3 Renormalization of the coefficients of the P^6 -terms when passing from the thermodynamic potential of a bulk material G to the effective potential of a film \tilde{G} . All values are given in $10^9 \frac{\text{m}^9}{\text{C}^4\text{F}}$ at 300K. a_{ijk}^{bulk} are coefficients of the expansion G for bulk and mechanically free BaTiO₃. Δa_{ijk} are corrections to corresponding a_{ijk}^{bulk} coefficients representing an addition to a_{ijk}^{bulk} (for example, $a_{333}^{\text{film}} = a_{111}^{\text{bulk}} + \Delta a_{333}$). a_{ijk}^{film} are coefficients of the \tilde{G} energy of the (001)-oriented clamped film. 28
- 3.1 Data obtained with the first principles calculations. c_{11} - stiffness, q_{11} and m_{111} - linear and nonlinear electrostriction coefficients. (a) Experimental data were taken or recalculated from Ref. [11]. (b) Data were taken or recalculated from Landolt and Bornstein [7]. 40
- 4.1 Electrostrictive coefficients which were used for calculations, for BaTiO₃ coefficients were taken from [5], for SrTiO₃ from [6], and PbTiO₃ from [1]. The Q_{44} values are written taking into account the factor of 2 as defined in Landolt-Bornstein [7]. 48

List of Tables

5.1	Material parameters obtained from analysis of phonon dispersions of cubic STO ($a = 3.89 \text{ \AA}$) under pressure 69 kBar. c^{eff} is effective value of mechanical stiffness obtained from the tangent of the TA branch at Γ -point. f and M are static and dynamic flexocoupling coefficients. ρ is the density of STO, $\rho = 5174 \frac{\text{kg}}{\text{m}^3}$, calculated by the mass of atoms in the unit cell divided by the volume.	71
5.2	Dielectric suitability, χ , and dynamic flexocoupling coefficient, M , obtained from the analysis of phonon dispersion curves and calculated from Interatomic Force Constants (IFCs).	75
5.3	Material parameters of STO obtained joining the two methods based on phonon dispersions and IFCs. χ/ϵ_0 is relative dielectric susceptibility. f and M are static and dynamic flexocoupling coefficients. μ is static flexoelectric tensor.	78

Table of Notations

P_i	Polarization
ϵ_{ij}	Dielectric constant
χ_{ij}	Dielectric susceptibility
E_i	Electric field
D_i	Dielectric displacement
σ_{ij}	Mechanical stress
ϵ_{ij} or u_{ij}	Mechanical strain
ρ	Density
G	Thermodynamic energy in terms of polarization and stress
a, a_{ij}, a_{ijk}	Dielectric stiffness and higher-order dielectric stiffness in G
s_{ijkl}	Elastic compliances
N_{ijklmn}	Nonlinear elastic compliances
Q_{ijkl}	ordinary electrostriction in G
M_{ijklmn}, R_{ijklmn}	High-order electrostriction tensors in G
F	Thermodynamic energy in terms of polarization and strain
b, b_{ij}, b_{ijk}	Dielectric stiffness and higher-order dielectric stiffness in F
c_{ijkl}	Stiffness
n_{ijklmn}	Non-linear stiffness tensor
q_{ijkl}	Electrostrictive tensors
m_{ijklmn}, r_{ijklmn}	High-order electrostrictive tensors in F
f_R	Resonance frequency
f_{AR}	Antiresonance frequency
n_r	Relative tunability
ω	Frequency of phonon
q_i	Wave vector of phonon
t	Time
U_i	Displacement
e_{ijk}	Piezoelectric coefficient
μ_{ijkl}	Flexoelectric coefficient
f_{ijkl}^{tot}	Total bulk flexoelectric coefficient
f_{ijkl}	Static bulk flexoelectric coefficient
M_{ij}	Dynamic bulk flexoelectric coefficient

Introduction

Electromechanical effects control a large amount of physical properties and, nowadays, are widely used in many technical applications. Since the first electrical relays used in the telegraph at the end of 18th century devices based on electromechanical effects are everywhere. The devices based on electromechanical effects such as sensors, actuators, radio filters, switchers, etc. are part of modern devices and tools: radio and TV sets, mobile and landline phones, ultrasonic medical equipment, and millions of others.

Speaking about electromechanical effects one usually means piezoelectric effect (or converse piezoelectric effect). The piezoelectric effect was discovered in 1880 by the brothers Pierre and Jacques Curie. They were doing experiments with tourmaline, quartz, topaz, cane sugar and Rochelle salt and they found out that a mechanical stress can cause electricity, moreover the measured voltage was proportional to the mechanical stress. The converse effect was however discovered later by Gabriel Lippmann in 1881 using the thermodynamic aspect of the theory of piezoelectricity. These two phenomena were called piezoelectric and converse (inverse) piezoelectric effect respectively from Greek's "piezein" which means "to press" or "to squeeze".

The understanding of the concept of piezoelectricity in solids begins with the understanding of the internal structure of the material. Let us consider for simplicity a single crystal material. This material is made up of atoms with positive or negative charge that are constrained to occupy positions in a specific repeating relationship to each other building up the structure or lattice of the crystal. The symmetry of a crystal internal structure governs the symmetry of its external properties, it is so called Neumann's principle. Namely, the specific symmetry possessed by the structure determines whether it is possible for piezoelectricity to exist in the crystal. All crystals can be divided into 32 different classes or point groups utilizing these symmetry elements. These 32 point groups are subdivisions of seven basic crystal systems that are, in order of ascending symmetry, triclinic, monoclinic, orthorhombic, tetragonal, rhombohedral (trigonal), hexagonal, and cubic. Of the 32 point groups, 21 classes are non-centrosymmetric (a necessary condition for piezoelectricity to exist) and 20 of these are piezoelectric.

The piezoelectric effect is a linear interaction between the mechanical and the electrical state in crystalline materials with no inversion symmetry. The piezoelectric effect represents the

Introduction

creation of the electrical charge on the surface of the free standing material resulting from an applied mechanical force, in terms of dielectric displacement D_i and stress σ_{jk} , it is expressed as:

$$D_i = d_{ijk}\sigma_{jk}. \quad (1)$$

Hereafter, when needed, we apply the Einstein dummy suffix summation convention. The converse piezoelectric effect (the appearance of a mechanical strain ϵ_{jk} resulting from an applied electrical field E_i) could be described as:

$$\epsilon_{jk} = d_{ijk}E_i. \quad (2)$$

The two effect always coexist, and the proportionality constant d_{ijk} is the piezoelectric constant.

There are 10 out of a possible 20 piezoelectric crystal classes that are designated as pyroelectric. This group of materials possesses the unusual characteristic of being permanently polarized within a given temperature range. Unlike the more general piezoelectric classes that produce a polarization under stress, the pyroelectrics possess this polarization permanently. This polarization also changes with temperature, hence, the term pyroelectricity. Pyroelectric crystals, such as tourmaline and wurtzite, are often called polar materials, thus referring to the polar axis which direction cannot be changed within the symmetry operations of the material. The total dipole moment varies with temperature, leading to a change in sign for the current flowing out of a short-circuited crystal.

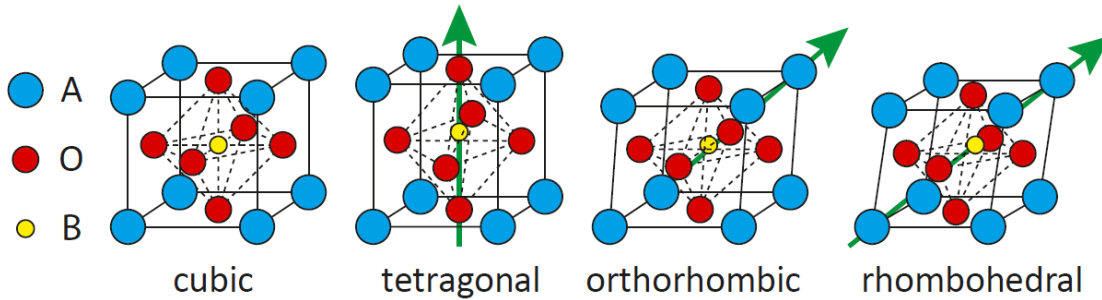


Figure 1: Perovskite structure of ABO_3 on example of $BaTiO_3$. The material can exist in different phases: (a) cubic phase, (b) tetragonal phase, (c) orthorhombic phase, and (d) rhombohedral phase. The direction of polarization in different phases is shown with the green arrow.

If a material possesses a phase transition from non-polar to polar phase, accompanied with the lowering of the symmetry, this material is called ferroelectric. One of the most important groups of ferroelectrics is perovskites. In perovskites in the ferroelectric phase, there exist more than one polar state, and the orientation of the polarization can be reoriented by an electric field of some magnitude. A typical perovskite ABO_3 cubic unit-cell structure is given in Fig. 1. For example, the unit cell of $BaTiO_3$ (BTO) consists of a corner-linked network of

Ba^{2+} atoms (A sites) and Ti^{4+} ions occupying sites (B sites) within the octahedral cage of O^{2-} octahedra.

In most cases, however, depending on temperature, the simple cubic structure of perovskites undergoes several phase transitions. In BTO, there are cubic paraelectric and three ferroelectric phases (tetragonal, orthorhombic, and rhombohedral) shown in Fig. 1. These ferroelectric phases are described by direction of polarization and associated distortion of the cubic unit cell.

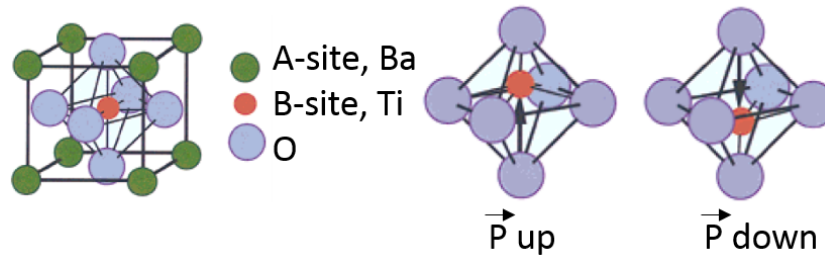


Figure 2: Perovskite ABO_3 unit cell of BaTiO_3 illustrating 180° polarization reversal for two of the six possible polarization states of the tetragonal phase produced by displacement of the central cation in the tetragonal phase.

Under application of an electric field atoms move to new positions along the direction of the applied field, which is schematically shown in Fig. 2. That leads to the change of polarization of the sample.

Good dielectric and electromechanical properties of ferroelectric materials condition their wide range of applications. Among these applications are high dielectric-constant capacitors, piezoelectric sonar and ultrasonic transducers, radio and communication filters, pyroelectric security surveillance devices, medical diagnostic transducers, buzzers, gas igniters, various sensors and switches, ultrasonic motors, electro-optic devices, thin-film capacitors, ferroelectric thin-film memories, etc.

Electrostriction is another electromechanical effect that exists in ferroelectric materials. Unlike piezoelectricity, where the deformation is linear with respect to the applied field, and it changes sign when the field is reversed, electrostriction is a quadratic effect with respect to polarization

$$\epsilon_{ij} = Q_{ijkl} P_k P_l \quad (3)$$

where P_i is the polarization, and Q_{ijkl} is the electrostrictive coefficient. This also means that electrostriction produces an expansion in most materials (if $Q > 0$) in the direction of the field regardless of its polarity. Electrostriction is a general property of all dielectric materials, whether they are crystals, amorphous, ceramics, polar, or centrosymmetric.

Until nowadays, the non-linear electrostrictive couplings were not yet considered and were usually neglected in both physical models and engineering calculations for electromechanical

systems. In contrast to the "normal" electrostrictive coupling which is linear in deformation and quadratic in polarization, here we are dealing with couplings that involve higher powers of these variables. It is presently understood that there are systems where these couplings can be decisive. For example, for the phase diagrams of ferroelectric thin films, the non-linear electrostrictive coefficients determine the phase of the film. Another important aspect of non-linear electrostriction was recognized during recent development of tunable Film Bulk Acoustic wave Resonators (FBARs): it was found that the non-linear electrostrictive interaction can essentially control the performance of such devices.

Another phenomenon, which is of a special interest, is the flexoelectric effect. This effect is controlled by the linear coupling between the deformation gradient and polarization (in contrast to the piezoelectric effect which is controlled by the linear coupling between deformation and polarization). The flexoelectric effect, being of high fundamental interest, was recently also recognized as the basis for a new type of mechanical sensors. At the same time, the recent experimental studies establish the important role of this coupling in behaviour of multi-domain and disordered ferroelectrics.

Goals and objectives of the thesis

The goal of the thesis is to develop new theoretical knowledge on the high-order electro-mechanical couplings in ferroelectrics. The work will be focused on the missing knowledge in the field, which can be summarized as follows.

The role of non-linear electrostrictive couplings in the phase formation in ferroelectric thin films was identified, however the information on the constants of non-linear electrostrictive interactions is very limited. Therefore we want to perform relevant first principles calculations to evaluate them and show their importance for real systems.

There is a growing interest of flexoelectricity from both theoretical and experimental points of view, however there are still many problems to be addressed. Namely, the dynamic bulk flexoelectric tensor was found to be important, but not yet measured or calculated. Here, we intend to show how to obtain the information on the bulk flexoelectric tensors exploiting a phonon spectrum. Using the model phonon spectrum of STO calculated with first principles methods, we want to evaluate the dynamic bulk flexoelectric tensor.

Two kinds of the theoretical activity are intended: (i) a work in terms of the continuous phenomenological theory (Landau theory, electrodynamics, phenomenological charge transport, etc.), (ii) first principles calculations using Density Functional Theory (DFT).

Outline of the thesis

The thesis is split into a few chapters. The introduction gives the general information about electromechanical effects and ferroelectric materials where these effects are of interest. The first chapter will show the state of the art including the latest achievements in the field. The second chapter will be devoted to DFT calculations of high-order electrostriction coefficients and to subsequent phenomenological development of the strain-temperature phase diagrams for ferroelectric thin films of a model ferroelectric BTO. In the third chapter we will study tunable Film Bulk Acoustic wave Resonators using Landau theory with the thermodynamic coefficients *ab initio* calculated. Then, we will consider electrostrictive effect for different crystallographic directions in perovskite bulk crystals and thin films. In the fifth chapter, using first principles calculations the flexoelectric effect will be studied. It will be demonstrated how to calculate the static and dynamic flexoelectric tensors with the help of the model phonon spectrum of SrTiO₃. The sixth chapter will be devoted to first principles calculations of antiphase boundaries in antiferroelectric PbZrO₃. At the end, we will summarize the obtained results and show possible impact in the field.

1 State of the art

Electromechanical properties of solids are widely used in many technical applications. Traditionally, speaking about electromechanical properties, one means the piezoelectric effect. Indeed nowadays this effect is widely used in devices based on bulk [12] or thin film materials [13]. Specifically, piezoelectrics, i.e. materials exhibiting the piezoelectric effect, are used, for example, in sensors, actuators, RF filters, and active damping devices. Materials, which exhibit piezoelectricity, are also good candidates for the energy harvesting use [14]. However, without diminishing the role of the piezoelectric effect, the recent developments in the field revealed that the so-called high order electromechanical couplings (and corresponding electromechanical effects) become of increasing importance [15].

1.1 Non-linear electrostrictive couplings and strain engineering

As was mentioned in the introduction, until recently, the non-linear electrostrictive couplings have been almost completely ignored when analysing the electromechanical properties of solids. The first relevant work was published by Yushin in 1996 [16]. The importance of these couplings was recognized later especially for the thin films. Recently, it became possible to control and even to engineer the phase of a ferroelectric film through creating different misfit strain between the film and the substrate by using different substrates, which nowadays constitutes a whole branch of materials science, so-called "strain engineering". It was demonstrated that the "ordinary" low-order electrostrictive coupling is extremely important for this control. The temperature-strain phase diagrams (see Fig. 1.1) have been developed for classical materials such as BaTiO_3 , PbTiO_3 , and SrTiO_3 [17, 18]. As a great success in this field, one should mention the paper by Haeni [19] where governed by this coupling ferroelectricity was stimulated for the paraelectric SrTiO_3 at room temperature. This observation was in a qualitative agreement with the theoretical prediction, moreover the experiment was actually stimulated by the theory. However, the further theoretical studies [20] established that the adequate derivation of the temperature-strain phase diagrams for ferroelectric thin films is impossible without taking into account the non-linear electrostrictive couplings. Up to date, no theoretical work has been done neither on the incorporation of these couplings into the

phenomenological theory nor on the first principle calculations of the corresponding coupling constants.

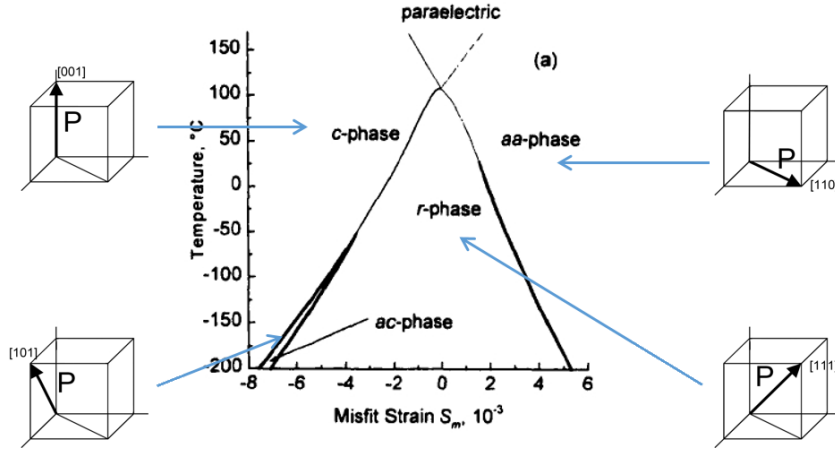


Figure 1.1: Temperature - misfit strain phase diagrams of a single-domain (001)-oriented BaTiO₃ taken from Ref. [1]. The phases are denoted as (i) the c-phase, polarization is out-of-plane ($P_1 = P_2 = 0, P_3 \neq 0$); (ii) the aa-phase, where polarization is in-plane ($P_1 \neq 0, P_2 \neq 0, P_3 = 0$); (iii) the ac-phase where $P_1 \neq 0, P_2 = 0, P_3 \neq 0$; (iv) r-phase, where all components of polarization are non-zero; and (v) paraelectric phase, polarization is 0.

Quite recently the importance of non-linear electrostrictive couplings was also realized in the context of the development of a new type of microwave tunable devices, tunable Film Bulk Acoustic wave Resonators (FBARs). In such devices, the piezoelectric effect is induced in a non-piezoelectric material by the application of a dc electric field [21]. Thus, in a thin non-piezoelectric film, the excitation of the piezoelectric resonance (like that used in quartz-based watches) was found possible. However, in tunable FBARs, in contrast to normal piezoelectrics like quartz, the parameters of the resonance can be tuned with the applied dc electric field. Modelling of such devices established that the tuning of its antiresonance frequency is mainly controlled by the non-linear electrostrictive couplings [22, 23]. Moreover, it was shown that it is the strength of this interaction that is decisive for the use of tunable FBARs in tunable RF filters.

The said above shows that the high-order electromechanical couplings are an important new issue for both fundamentals of ferroelectrics and applications. This is explained by a limited theoretical work done in the field since until recently the importance of the high-order electromechanical couplings was not recognized.

1.2 Flexoelectric effect

The name flexoelectric originates from the Latin word "flexus" meaning "bend" and is related to the fact that a strain gradient naturally arises in bent plates. The flexoelectric effect is an electromechanical effect in which the dielectric polarization exhibits a linear response to

a gradient of mechanical strain. In a piezoelectric material, an applied uniform strain can induce an electric polarization and vice-versa. Crystallographic considerations indicate that this technologically important property is fundamentally restricted to non-centrosymmetric crystal systems. For piezoelectrics, the polarization vector P_i is related to the second order strain tensor ϵ_{jk} through the third order piezoelectric tensor d_{ijk} :

$$P_i = d_{ijk}\epsilon_{jk}. \quad (1.1)$$

Tensor transformation properties require that under inversion-centre symmetry, all odd-order tensors (like d_{ijk} , third-order tensor) vanish. Thus, many common dielectrics, e.g. Silicon and NaCl are not piezoelectric whereas ZnO and GaAs are. Actually it is possible to extend the conventional piezoelectric constitutive law by including strain gradients:

$$P_i = d_{ijk}\epsilon_{jk} + f_{klj} \frac{\partial \epsilon_{kl}}{\partial x_j}. \quad (1.2)$$

Here $\frac{\partial \epsilon_{kl}}{\partial x_j}$ and f_{klj} are the strain gradient and the tensor of static flexoelectric coefficients, respectively. While the piezoelectric property is non-zero only for selected non-centrosymmetric materials, the strain gradient-polarization coupling (i.e. flexoelectric coefficients) is in principle non-zero for all dielectric materials including those that are centrosymmetric. This implies that under a non-uniform strain, all dielectric materials are capable of producing a polarization.

Though the existence of the flexoelectric effect in solids was predicted long time ago, only a little attention was paid to it, primarily because the effect was expected to be weak. However, recently, the situation has changed. First, systematic experimental studies on flexoelectricity in ferroelectric ceramics showed that the response can be several orders of magnitude stronger than was expected based on theoretical estimates [24]. Second, in line with the modern trend to the miniaturization, the length scales decrease, and therefore larger strain gradients and, correspondingly, larger flexoelectric effects are expected. The flexoelectric effect looks promising for practical applications and helps to explain a number of phenomena, especially at the nanoscale. However, available theoretical and experimental results are rather contradictory, attesting to a limited understanding of flexoelectricity.

The first phenomenological framework for the description of this effect was offered by Kogan [25] in 1964, who did it in the context of electron-phonon coupling in centrosymmetric crystals, where the flexoelectric coupling may play an important role. The analysis of the magnitude of the static bulk flexoelectric coefficients provided by Kogan was later generalized to ferroelectrics by the Tagantsev [26]. In ferroelectrics, the materials in which this effect looks to be interesting for practical applications, flexoelectricity was first addressed by Bursian and coworkers [27, 28]. They characterized flexoelectricity in the classical ferroelectric BaTiO₃ and demonstrated switching of spontaneous polarization driven by a strain gradient. These authors also developed a phenomenological theory of the flexoelectric effect in a finite plate of a ferroelectric. One of the results of this theory is that the flexoelectric effect should be

strongly enhanced in materials with high dielectric permittivity, e.g. ferroelectrics.

The evaluation of flexoelectric properties is a challenging task both experimentally and theoretically. Experimental measurements of the flexoelectric effect of high-dielectric-constant ceramics such as lead magnesium niobate, barium strontium titanate and lead zirconate titanate by Cross and co-workers [3, 29, 30] show that the magnitude of their flexoelectric coefficients are of the order of 10^{-6} C/m which is two orders of magnitude larger than theoretical estimates. At the same time, the values of the components of the static flexoelectric tensor for SrTiO₃ recently experimentally estimated by Zubko et al. [31] are of the order of 10^{-8} C/m, which reasonably agree with the estimates by Tagantsev [6].

Recent experimental studies on flexoelectricity-driven phenomena are also numerous. The results of these studies attest to the key feature of the flexoelectric effect, namely, that a strain gradient (via the flexoelectric coupling) may work as an electric field: it can induce poling, switching, and rotation of polarization; it can create a voltage offset of hysteresis loops and smear the dielectric anomaly at ferroelectric phase transitions. Gruverman et al. [2] observed polarization switching in the (111)-oriented (PZT)-based capacitors generated by substrate bending and provided direct experimental evidence of stress-induced switching (Fig. 1.2).

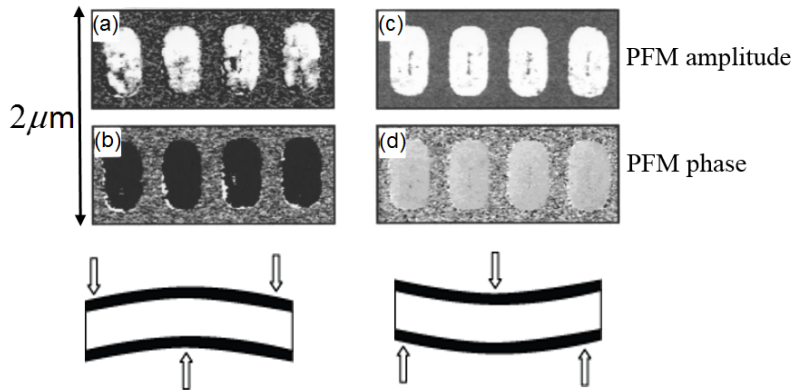


Figure 1.2: PFM (Piezoresponse Force Microscopy) images illustrating the impact of stress on polarization switching behaviour of the (111)-oriented PZT capacitors, taken from Ref. [2]. (a) and (b) - images of PFM amplitude and phase after tensile stress application, (c) and (d) - PFM amplitude and phase after compressive stress application.

At the same time, theoretical estimations show that effective electric field E^{eff} arising under application of bending due to flexoelectric effect is an order of $E^{\text{eff}} = \frac{f}{\chi} \frac{1}{R} \approx 0.1\text{V/cm}$, where χ is dielectric susceptibility and R characteristic bending radius, which is absolutely insufficient to perform polarisation switching. Later, Gruverman et al. [32] demonstrated that the stress gradient generated by the tip of an atomic force microscope can mechanically switch the polarization in the nanoscale volume of a ferroelectric film.

Recently, the idea to exploit flexoelectricity in a new type of composites to generate effective piezoelectricity has been discussed and theoretically analysed by Sharma et al. [33]. A sug-

gestion was made by Cross et al. [3, 29] about the possibility of creating composite material of non-piezoelectric materials which exhibit the piezoelectric response originating from the flexoelectric coupling. The idea behind such materials is to make working the strain gradients and to have effective piezoelectricity through the flexoelectric effect (Fig. 1.3).

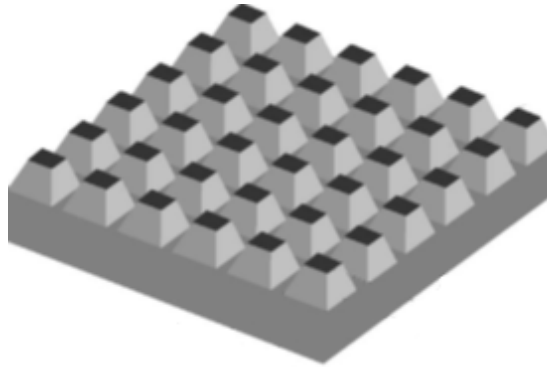


Figure 1.3: Diagrammatic sketch of a flexoelectric piezoelectric composite made of truncated pyramidal blocks of BST ceramics. Taken from Ref. [3].

Cross et al [3] have published studies on such composites reporting, for a $\text{Ba}_x\text{Sr}_{1-x}\text{TiO}_3$ (BST) based structure, an effective piezoelectric modulus of 40 pC/N (for example, for quartz piezoelectric modulus $d_{11} = 2.3$ pC/N). As was also shown by Majdoub et al. [34] the flexoelectric effect (as revealed by recent calculations on prototype nanostructures) under certain circumstances can compete with the piezoelectric response. Flexoelectric composites can have wide range of applications as, for example, in energy harvesting and as vibration and pressure sensors. Furthermore, they cannot be depoled offering an advantage in operation at the higher temperatures than ferroelectric piezoelectric ceramics.

Flexoelectric effect actually represents 4 related phenomena: static and dynamic bulk flexoelectric effects, surface flexoelectric effect and surface piezoelectricity [24].

The static bulk flexoelectric response is controlled by the redistribution of the bound charge of a crystal driven by a strain gradient, where ionic and electronic contributions can be distinguished. The theories of this phenomenon provide relationships between the flexoelectric tensor introduced phenomenologically and the microscopical parameters of the material (e.g. the dynamical matrix which describes the energy of interatomic interactions in the crystal). The ionic contribution to flexoelectricity was evaluated for several perovskite ferroelectrics and bi-atomic crystals by Sharma and coworkers [35] using the framework offered by Tagantsev [36]. Ab initio calculations of this contribution were performed by Hong et al [37] and Ponomareva et al [38] for SrTiO_3 , BaTiO_3 , and their solid solution. The first-principles calculations of the purely electronic contribution to flexoelectricity have been done by Hong and Vanderbilt for a number of crystals, including classical perovskites [39] and Stengel [40]. The concept behind these calculations, stemming from the classical work by Martin [41], was formulated by Resta [42]. The electronic contribution to flexoelectricity in carbon nanosystems was evalu-

Chapter 1. State of the art

ated by Dumitrica et al [43] and Kalinin and Meunier [44] using ab initio calculations. Ab initio and shell model results for static bulk flexoelectric effect are available for non-ferroelectric crystals (GaAs, GaP, ZnS, NaCl, and KCl) and ferroelectric (BaTiO₃, SrTiO₃) crystals [15]. For non-ferroelectric, the calculated value of the bulk flexoelectric coefficients were found to be in the range $10^{-12} - 10^{-11}$ C/m, which are essentially smaller than Kogan's estimate.

The importance of the surface effects in the flexoelectric behaviour of ferroelectrics was identified by Tagantsev and Yurkov [45]. It was also shown by Indenbom et al [46] and Eliseev et al [47] that taking flexoelectricity into account will lead to a modification of the electrical and mechanical boundary conditions.

Revising the work done in the field, one can conclude that the available theoretical knowledge on static bulk flexoelectric tensor is quite limited and the variety of terminology and methods used in different papers often obscure the links between different results. The dynamic bulk flexoelectric tensor was identified by Tagantsev [24, 48], but never measured or calculated, however its contribution is considered to be important. Surface flexoelectricity and surface piezoelectricity are little studied and their values are experimentally unknown.

2 Can we trust thin film diagrams?

In the introduction we already mentioned the importance of taking into account the non-linear electrostrictive couplings for problems involving ferroelectric thin films. In this chapter we will consider in depth the theory laying behind the matter and the impact of non-linear electrostrictive coefficients on the temperature - misfit strain phase diagrams.

2.1 Strain engineering

Strain engineering is a modern strategy to control and enhance materials properties. It represents a technique which deals with semiconductor and ferroic thin films strained on a substrate. Such strain can be tensile or compressive and occurs due to the difference between lattice parameters or due to the difference of the thermal expansion coefficients of the film and that of the underlying substrate. In strain-engineered ferroics, the strain appearing in the film shifts the transition temperatures and can change the properties of the material such as the dielectric and piezoelectric constants, remanent polarization, or even can induce room temperature ferroelectricity in a non-ferroelectric material [19]. Currently used methods for the description of thermodynamics of ferroic thin films (classical Landau theory [17], phase field modeling [49], and ab initio based Monte-Carlo (MC) simulations [50]) are based on an energy expansion in terms of internal degrees of freedom. Any treatment of this kind starts from such expansion for the bulk ferroic (e.g. the effective Hamiltonian for MC simulations [50] or a thermodynamic potential for Landau theory analysis [17]). Further mixed mechanical conditions corresponding to the films are applied. This way one establishes a kind of effective thermodynamic potential (or effective Hamiltonian) of the film. Minimisation of such potential or further MC simulations yield the ferroic state of a film as a function of the temperature and misfit strain. The standard way to present the results of such calculations is the so-called "temperature - misfit strain" phase diagrams [17], which give the ferroic state depending on temperature and parent misfit strain of the film. Such diagrams have been developed for many classical ferroelectric materials like BaTiO₃[1, 17, 49–51], PbTiO₃[1, 51], and SrTiO₃[18].

The goal of this work is to draw attention to the fact that the aforementioned methods of description of ferroelectric thin films in their current implementations may suffer from a serious *principle* drawback, which may lead to erroneous results. It is commonly understood that a large (sometimes enormous) difference between the properties of a strained film and its bulk counterpart is due to the coupling between the order parameter and strain. Customarily this coupling is modeled in the so-called electrostriction approximation corresponding to terms quadratic in the order parameter and linear in mechanical strain (stress) in the thermodynamic potential [17] or effective Hamiltonian [50] of the bulk material. Already 10 years ago, when using the electrostriction approximation for a special situation in PbTiO₃ films of (111)-orientation, a possible *principle* deficiency of this approximation was pointed out [20]. This chapter is devoted to a comprehensive analysis of this problem in terms of Landau theory however the conclusion should hold for MC simulations as well. We show that this "ordinary" electrostriction based description provides an adequate approach of thermodynamics of ferroelectric thin films if and only if it is controlled by the free energy expansion up to fourth power terms in polarization. However, if the sixth-power polarization terms (γ -terms) are needed in the expansion, which is a common situation for ferroelectric perovskites, higher-order electromechanical couplings should be taken into account. First, we elucidate the matter in terms of a simplified phenomenological model. Second, to demonstrate the phenomenon for thin films, we estimate some higher-order electrostrictive coefficients using experimental data and we calculate missing coefficients (in order to have a complete set) using ab initio methods. Then, we show that the higher-order electromechanical couplings readily lead to an order-of-magnitude renormalization of the γ -terms of free energy when passing from the bulk thermodynamic potential to the effective thermodynamic potential of the film. Finally, we illustrate our message with the results of the calculations for a BaTiO₃ thin film.

2.2 Scalar model

The problem with the "electrostriction based" description of strained ferroelectrics can be illustrated qualitatively by a simple scalar model. Let us describe a ferroelectric with a Gibbs thermodynamic potential energy expansion keeping only one component of polarization P and stress σ :

$$G = \underbrace{\frac{\alpha}{2}P^2 + \frac{\beta}{4}P^4 + \frac{\gamma}{6}P^6 - \frac{s}{2}\sigma^2 - QP^2\sigma}_{\text{"ordinary"}} - \underbrace{\frac{M}{2}P^2\sigma^2 - RP^4\sigma - \frac{N}{3}\sigma^3}_{\text{"high-order"}}, \quad (2.1)$$

where the "ordinary" part represents Gibbs energy commonly used to describe ferroelectric systems (Q - "ordinary" electrostrictive coefficient, s - linear compliance) and "high-order" terms (M , R - high-order electrostrictive coefficients and N - non-linear compliance) which are customarily neglected. This neglect can be readily justified for a bulk material but the situation for the clamped system is different. We can show this considering ferroelectricity in a clamped system, i.e. where the strain ϵ equals the misfit strain ϵ_0 . To obtain the effective

potential of the clamped system

$$\tilde{G} = G + \epsilon\sigma, \quad (2.2)$$

where T is temperature, we eliminate stress σ using a mechanical equation of state

$$\epsilon = \epsilon_0 = -\frac{\partial G}{\partial \sigma} = s\sigma + N\sigma^2 + QP^2 + RP^4 + MP^2\sigma, \quad (2.3)$$

and write the effective thermodynamic potential $\tilde{G}(P, T, \epsilon_0)$:

$$\tilde{G}(P, T, \epsilon_0) = \frac{\alpha^*}{2}P^2 + \frac{\beta^*}{4}P^4 + \frac{\gamma^*}{6}P^6 + \frac{\epsilon_0^2}{2s}, \quad (2.4)$$

where minima of \tilde{G} with respect to polarization correspond to the ground state of the clamped system. Electromechanical interactions in such systems lead to renormalizations of α , β and γ :

$$\alpha^* = \alpha - \epsilon_0 \frac{Q}{s} - \underbrace{\epsilon_0^2 \left(\frac{M}{2s^2} + \frac{QN}{s^3} \right)}_A, \quad (2.5)$$

$$\beta^* = \beta + 2 \frac{Q^2}{s} + \underbrace{\epsilon_0 \left(\frac{MQ}{s^2} - \frac{R}{s} - \frac{NQ^2}{s^3} \right)}_B, \quad (2.6)$$

$$\gamma^* = \gamma - \underbrace{3M \frac{Q^2}{s^2} + 6R \frac{Q}{s} + 2N \frac{Q^3}{s^3}}_C. \quad (2.7)$$

Now, let us have a closer look at Eqs. (2.5)-(2.7). The $\epsilon_0 \frac{Q}{s}$ term in (2.5) leads to the shift of the phase transition temperature. The $2 \frac{Q^2}{s}$ term in (2.6) renormalizes β , for example, for BaTiO₃ this "renormalization" switches the sign of β , i.e. it changes the order of the phase transition passing from a bulk material to a film [1]. These two "electrostrictive" corrections do not involve high-order electrostrictive couplings, they are well known and justified experimentally [19, 52]. At the same time, atomic order-of-magnitude estimates show that, in (2.5), $\frac{Q}{s}$ is about $(\frac{M}{2s^2} + \frac{QN}{s^3})$ whereas $2 \frac{Q^2}{s}$ is about $(\frac{MQ}{s^2} - \frac{R}{s} - \frac{NQ^2}{s^3})$ in (2.6). Thus, in view of smallness of ϵ_0 for any practical situation the A and B corrections are expected to be negligible, except the cases where the low-order corrections are unusually small. However, atomic order-of-magnitude estimates suggest that the C correction in (2.7) is of the same order of magnitude as γ similar to the strong renormalization of the β term in (2.6). These estimates imply that the high-order coefficients, which are customarily neglected in the majority of problems, should be included into thermodynamic energy expansions as far as the " γ -term" in (2.1) is important for the description of a problem.

2.3 Landau theory of thin films with high-order electrostrictive couplings

There are several ways to introduce high-order couplings to Landau theory. The first one is to use the Gibbs thermodynamic energy expansion for a centrosymmetric cubic crystal with respect to polarization P_i and stress σ_{ij} :

$$G = aP^2 + a_{ij}P_i^2P_j^2 + a_{ijk}P_i^2P_j^2P_k^2 - \frac{s_{ijkl}}{2}\sigma_{ij}\sigma_{kl} - \frac{N_{ijklmn}}{3}\sigma_{ij}\sigma_{kl}\sigma_{mn} - Q_{ijkl}P_iP_j\sigma_{kl} - \frac{M_{ijklmn}}{2}P_iP_j\sigma_{kl}\sigma_{mn} - R_{ijklmn}P_iP_jP_kP_l\sigma_{mn}, \quad (2.8)$$

where a , a_{ij} , and a_{ijk} are dielectric stiffness and higher-order dielectric stiffness coefficients at constant stress, s_{ijkl} and N_{ijklmn} are linear and nonlinear elastic compliances, Q_{ijkl} is ordinary electrostriction, and M_{ijklmn} and R_{ijklmn} are high-order electrostriction tensors. The minima of G with respect to polarization at zero stress correspond to the ground state of the mechanically free sample. The G expansion is often used dealing with experimental data. Alternatively, when working with ab initio calculations, instead of G expansion one naturally uses the Helmholtz thermodynamic function F written in terms of polarization P_i and strain ϵ_{ij} :

$$F = bP^2 + b_{ij}P_i^2P_j^2 + b_{ijk}P_i^2P_j^2P_k^2 + \frac{c_{ijkl}}{2}\epsilon_{ij}\epsilon_{kl} + \frac{n_{ijklmn}}{3}\epsilon_{ij}\epsilon_{kl}\epsilon_{mn} - q_{ijkl}P_iP_j\epsilon_{kl} - \frac{m_{ijklmn}}{2}P_iP_j\epsilon_{kl}\epsilon_{mn} - r_{ijklmn}P_iP_jP_kP_l\epsilon_{mn}, \quad (2.9)$$

where q_{ijkl} , m_{ijklmn} and r_{ijklmn} are components of linear and high-order electrostrictive tensors, and c_{ijkl} and n_{ijklmn} are linear and non-linear stiffness tensors. The minima of F at zero strain correspond to the ground state of a fully mechanically clamped sample.

The relationships between the N_{ijklmn} and n_{ijklmn} coefficients can be found by resolving the mechanical state equations for stress:

$$\sigma_{ij} = c_{ijkl}\epsilon_{kl} + n_{ijklmn}\epsilon_{kl}\epsilon_{mn} \quad (2.10)$$

and strain:

$$\epsilon_{ij} = s_{ijkl}\sigma_{kl} + N_{ijklmn}\sigma_{kl}\sigma_{mn}. \quad (2.11)$$

Eliminating, for example, stress σ_{ij} between (2.10) and (2.11) and keeping linear terms in (2.10) in view of the smallness of ϵ_{ij} one can obtain:

$$n_{ijklmn} = -c_{ijuv}c_{klwx}c_{mnyz}N_{uvwxyz}. \quad (2.12)$$

Hereafter, we use the Voigt matrix notation when possible. In addition to standard Voigt

2.4. Legendre transformation of high-order electrostrictive coefficients

notations for stress σ_i , strain ϵ_i , elastic (s_{ij} and c_{ij}) [53] and linear electrostriction (q_{ij} and Q_{ij}) tensors, defining Q_{ij} according to the Landolt-Bornstein reference book [7]

$$Q_{ijkl} = \begin{cases} Q_{mn} & \text{for } n = 1, 2, 3 \\ \frac{Q_{mn}}{2} & \text{for } n = 4, 5, 6 \end{cases}, \quad (2.13)$$

we use the Voigt matrix notation for nonlinear elasticity (n_{ijk} and N_{ijk}) and high-order electrostriction (m_{ijk} , r_{ijk} , M_{ijk} , and R_{ijk}) tensors as follows:

$$N_{ijklmn} = \begin{cases} N_{abc}, & a, b, c = 1, 2, 3 \\ \frac{N_{abc}}{2}, & \text{one suffix } 4, 5, 6 \text{ and other } 1, 2, 3 \\ \frac{N_{abc}}{4}, & \text{one suffix } 1, 2, 3 \text{ and other } 4, 5, 6 \\ \frac{N_{abc}}{8}, & \text{for } a, b, c = 4, 5, 6 \end{cases}, \quad (2.14)$$

$$\begin{cases} M_{ijklmn} = M_{abc}, & a, b, c = 1, 2, 3 \\ M_{ijklmn} = \frac{M_{abc}}{2}, & a = 1, 2, 3; b, c = (\text{one suffix } 4, 5, 6 \text{ and another } 1, 2, 3) \\ M_{ijklmn} = \frac{M_{abc}}{4}, & a = 1, 2, 3; b, c = 4, 5, 6 \\ M_{414} = 8M_{231123}, M_{424} = 8M_{232223}, M_{456} = 8M_{231312} \end{cases}, \quad (2.15)$$

$$\begin{cases} R_{ijklmn} = R_{abc}, & a, b, c = 1, 2, 3 \\ R_{ijklmn} = \frac{R_{abc}}{2}, & a, b = 1, 2, 3; c = 4, 5, 6 \\ R_{144} = 4R_{112323}, R_{155} = 4R_{111313} \end{cases}. \quad (2.16)$$

The Voigt matrix notation for the coefficients of the F expansion are $n_{ijklmn} = n_{abc}$, $a, b, c = 1..6$; $m_{ijklmn} = m_{abc}$, $a = 1, 2, 3; b, c = 1..6$ and $m_{414} = 2m_{231123}, m_{424} = 2m_{232223}, m_{456} = 2m_{231312}$; and $r_{ijklmn} = r_{abc}$, $a, b = 1, 2, 3; c = 1..6$ and $r_{144} = 2r_{112323}, r_{155} = 2r_{111313}$.

2.4 Legendre transformation of high-order electrostrictive coefficients

Knowing the coefficients of Helmholtz thermodynamic function F written in terms of polarization P_i and strain ϵ_i (2.9) it is possible to find the corresponding coefficients of Gibbs energy expansion G with respect to polarization P_i and stress σ_i (2.8). One performs Legendre transformation

$$G = F - \epsilon_i \sigma_i \quad (2.17)$$

Chapter 2. Can we trust thin film diagrams?

where $\epsilon_i \sigma_i$ represents the work required to maintain a constant stress. Then, the solutions of the mechanical equation of state

$$\sigma_i = -\frac{\partial F}{\partial \epsilon_i}, i = 1..6 \quad (2.18)$$

with respect to ϵ_i were expanded in series, and only low order terms of the expansion were kept, after that, ϵ_i were substituted into (2.17). This way, one eliminates strains ϵ_i between (2.17) and (2.18) and obtains G as function of P_i and σ_{ij} with new high-order electrostrictive coefficients express in terms of c_{ij} , m_{ijk} , and r_{ijk} . The transformations of the corresponding high-order electrostrictive coefficients are listed below (2.19 - 2.33).

$$M_{111} = \frac{(c_{11} + c_{12})^2 m_{111}}{(c_{11} - c_{12})^2 (c_{11} + 2c_{12})^2} - \frac{4c_{12} (c_{11} + c_{12}) m_{112}}{(c_{11} - c_{12})^2 (c_{11} + 2c_{12})^2} + \frac{2c_{12}^2 m_{122}}{(c_{11} - c_{12})^2 (c_{11} + 2c_{12})^2} + \frac{2c_{12}^2 m_{123}}{(c_{11} - c_{12})^2 (c_{11} + 2c_{12})^2}, \quad (2.19)$$

$$M_{112} = -\frac{c_{12} (c_{11} + c_{12}) m_{111}}{(c_{11} - c_{12})^2 (c_{11} + 2c_{12})^2} + \frac{(c_{11}^2 + c_{11} c_{12} + 2c_{12}^2) m_{112}}{(c_{11} - c_{12})^2 (c_{11} + 2c_{12})^2} - \frac{c_{11} c_{12} m_{122}}{(c_{11} - c_{12})^2 (c_{11} + 2c_{12})^2} - \frac{c_{11} c_{12} m_{123}}{(c_{11} - c_{12})^2 (c_{11} + 2c_{12})^2}, \quad (2.20)$$

$$M_{122} = \frac{c_{12}^2 m_{111}}{(c_{11} - c_{12})^2 (c_{11} + 2c_{12})^2} - \frac{2c_{11} c_{12} m_{112}}{(c_{11} - c_{12})^2 (c_{11} + 2c_{12})^2} + \frac{(c_{11}^2 + 2c_{11} c_{12} + 2c_{12}^2) m_{122}}{(c_{11} - c_{12})^2 (c_{11} + 2c_{12})^2} - \frac{2c_{12} (c_{11} + c_{12}) m_{123}}{(c_{11} - c_{12})^2 (c_{11} + 2c_{12})^2}, \quad (2.21)$$

$$M_{123} = \frac{c_{12}^2 m_{111}}{(c_{11} - c_{12})^2 (c_{11} + 2c_{12})^2} - \frac{2c_{11} c_{12} m_{112}}{(c_{11} - c_{12})^2 (c_{11} + 2c_{12})^2} - \frac{2c_{12} (c_{11} + c_{12}) m_{122}}{(c_{11} - c_{12})^2 (c_{11} + 2c_{12})^2} + \frac{(c_{11}^2 + 2c_{11} c_{12} + 2c_{12}^2) m_{123}}{(c_{11} - c_{12})^2 (c_{11} + 2c_{12})^2}, \quad (2.22)$$

$$M_{144} = \frac{m_{144}}{c_{44}^2}, \quad (2.23)$$

$$M_{155} = \frac{m_{155}}{c_{44}^2}, \quad (2.24)$$

$$M_{414} = \frac{(c_{11} + c_{12}) m_{414}}{(c_{11} - c_{12}) (c_{11} + 2c_{12}) c_{44}} - \frac{2c_{12} m_{424}}{(c_{11}^2 + c_{11} c_{12} - 2c_{12}^2) c_{44}}, \quad (2.25)$$

2.4. Legendre transformation of high-order electrostrictive coefficients

$$M_{424} = -\frac{c_{12}m_{414}}{(c_{11}^2 + c_{11}c_{12} - 2c_{12}^2)c_{44}} + \frac{c_{11}m_{424}}{(c_{11}^2 + c_{11}c_{12} - 2c_{12}^2)c_{44}}, \quad (2.26)$$

$$M_{456} = \frac{m_{456}}{c_{44}^2}, \quad (2.27)$$

$$R_{111} = \frac{(c_{11} + c_{12})m_{111}(c_{11}q_{11} + c_{12}(q_{11} - 2q_{12}))}{(c_{11} - c_{12})^2(c_{11} + 2c_{12})^2} + \frac{2c_{12}m_{122}(c_{12}q_{11} - c_{11}q_{12})}{(c_{11} - c_{12})^2(c_{11} + 2c_{12})^2} + \frac{2c_{12}m_{123}(c_{12}q_{11} - c_{11}q_{12})}{(c_{11} - c_{12})^2(c_{11} + 2c_{12})^2} + \frac{2m_{112}(c_{11}^2q_{12} + c_{11}c_{12}(-2q_{11} + q_{12}) + 2c_{12}^2(-q_{11} + q_{12}))}{(c_{11} - c_{12})^2(c_{11} + 2c_{12})^2} + \frac{(c_{11} + c_{12})r_{111}}{(c_{11} - c_{12})(c_{11} + 2c_{12})} - \frac{2c_{12}r_{112}}{c_{11}^2 + c_{11}c_{12} - 2c_{12}^2}, \quad (2.28)$$

$$R_{121} = \frac{m_{122}(c_{11}^2q_{11} + 2c_{12}^2q_{11} + c_{11}c_{12}(q_{11} - 4q_{12}))}{2(c_{11} - c_{12})^2(c_{11} + 2c_{12})^2} + \frac{c_{11}m_{111}(-c_{12}q_{11} + c_{11}q_{12})}{2(c_{11} - c_{12})^2(c_{11} + 2c_{12})^2} + \frac{m_{123}(-3c_{11}c_{12}q_{11} - 2c_{12}^2(q_{11} - 2q_{12}) + c_{11}^2q_{12})}{2(c_{11} - c_{12})^2(c_{11} + 2c_{12})^2} + \frac{m_{112}(2c_{12}^2q_{11} + c_{11}^2(q_{11} + 2q_{12}) - c_{11}c_{12}(q_{11} + 4q_{12}))}{2(c_{11} - c_{12})^2(c_{11} + 2c_{12})^2} - \frac{c_{12}m_{414}q_{44}}{2(c_{11}^2 + c_{11}c_{12} - 2c_{12}^2)c_{44}} + \frac{c_{11}m_{424}q_{44}}{2c_{11}^2c_{44} + 2c_{11}c_{12}c_{44} - 4c_{12}^2c_{44}} + \frac{c_{11}r_{121}}{c_{11}^2 + c_{11}c_{12} - 2c_{12}^2} - \frac{c_{12}r_{123}}{c_{11}^2 + c_{11}c_{12} - 2c_{12}^2}, \quad (2.29)$$

$$R_{112} = \frac{m_{112}(c_{11}^2q_{11} + 2c_{12}^2q_{11} + c_{11}c_{12}(q_{11} - 4q_{12}))}{(c_{11} - c_{12})^2(c_{11} + 2c_{12})^2} - \frac{c_{12}m_{111}(c_{11}q_{11} + c_{12}(q_{11} - 2q_{12}))}{(c_{11} - c_{12})^2(c_{11} + 2c_{12})^2} + \frac{c_{11}m_{122}(-c_{12}q_{11} + c_{11}q_{12})}{(c_{11} - c_{12})^2(c_{11} + 2c_{12})^2} + \frac{c_{11}m_{123}(-c_{12}q_{11} + c_{11}q_{12})}{(c_{11} - c_{12})^2(c_{11} + 2c_{12})^2} - \frac{c_{12}r_{111}}{c_{11}^2 + c_{11}c_{12} - 2c_{12}^2} + \frac{c_{11}r_{112}}{c_{11}^2 + c_{11}c_{12} - 2c_{12}^2}, \quad (2.30)$$

$$R_{123} = \frac{m_{123}(c_{11}^2q_{11} + c_{11}c_{12}(2q_{11} - 3q_{12}) + 2c_{12}^2(q_{11} - q_{12}))}{(c_{11} - c_{12})^2(c_{11} + 2c_{12})^2} + \frac{c_{12}m_{111}(c_{12}q_{11} - c_{11}q_{12})}{(c_{11} - c_{12})^2(c_{11} + 2c_{12})^2} + \frac{m_{122}(c_{11}^2q_{12} + c_{11}c_{12}(-2q_{11} + q_{12}) + 2c_{12}^2(-q_{11} + q_{12}))}{(c_{11} - c_{12})^2(c_{11} + 2c_{12})^2} + \frac{m_{112}(c_{11}^2q_{12} + 2c_{12}^2q_{12} - c_{11}c_{12}(2q_{11} + q_{12}))}{(c_{11} - c_{12})^2(c_{11} + 2c_{12})^2} + \frac{(c_{11} + c_{12})m_{414}q_{44}}{2(c_{11} - c_{12})(c_{11} + 2c_{12})c_{44}} - \frac{c_{12}m_{424}q_{44}}{(c_{11}^2 + c_{11}c_{12} - 2c_{12}^2)c_{44}} - \frac{2c_{12}r_{121}}{c_{11}^2 + c_{11}c_{12} - 2c_{12}^2} + \frac{(c_{11} + c_{12})r_{123}}{(c_{11} - c_{12})(c_{11} + 2c_{12})}, \quad (2.31)$$

$$R_{144} = \frac{m_{414}(c_{11}q_{11} + c_{12}(q_{11} - 2q_{12}))}{2(c_{11}^2 + c_{11}c_{12} - 2c_{12}^2)c_{44}} + \frac{-c_{12}m_{424}q_{11} + c_{11}m_{424}q_{12}}{(c_{11} - c_{12})(c_{11} + 2c_{12})c_{44}} + \frac{m_{144}q_{44}}{2c_{44}^2} + \frac{m_{456}q_{44}}{c_{44}^2} + \frac{r_{144}}{c_{44}}, \quad (2.32)$$

$$R_{155} = \frac{m_{414}(c_{11}q_{12} - c_{12}q_{11})}{(c_{11} - c_{12})(c_{11} + 2c_{12})c_{44}} + \frac{m_{424}(-2c_{12}q_{12} + c_{11}(q_{11} + q_{12}))}{(c_{11} - c_{12})(c_{11} + 2c_{12})c_{44}} + \frac{m_{155}q_{44}}{c_{44}^2} + \frac{r_{155}}{c_{44}}. \quad (2.33)$$

2.5 Thin film phase diagrams

To illustrate quantitatively the phenomenon described above in Sec. 2.2, we exploit an effective energy potential of a strained thin film of a single-domain (001)-oriented BTO on a square substrate. In principle, the considered below theory of thin films works not only for BTO, but for all ferroelectric materials characterized with $m\bar{3}m \rightarrow 4mm$ phase transition. To obtain the effective potential from the G expansion:

$$\tilde{G}(P_i, T, \epsilon_0) = G + \epsilon_1 \sigma_1 + \epsilon_2 \sigma_2 + \epsilon_6 \sigma_6, \quad (2.34)$$

the minima of which correspond to the ground state of the film partially clamped on the substrate [1], we apply mixed mechanical conditions

$$\begin{aligned} \frac{\partial G}{\partial \sigma_1} = \epsilon_0, \quad \frac{\partial G}{\partial \sigma_2} = \epsilon_0, \quad \frac{\partial G}{\partial \sigma_6} = 0 \\ \sigma_3 = 0, \sigma_4 = 0, \sigma_5 = 0 \end{aligned} \quad (2.35)$$

and eliminate stresses σ_1 , σ_2 and σ_6 . Hereafter a Cartesian coordinate system with the x_3 axis perpendicular to the film-substrate interface is considered, $\epsilon_0 = \frac{a_{\parallel} - a_0}{a_0}$ - biaxial parent misfit strain, where a_0 is the lattice parameter of the ferroelectric material in the cubic phase extrapolated to temperature T and a_{\parallel} is the in-plane lattice parameter of the film. Minimizing $\tilde{G}(P_i, T, \epsilon_0)$ with respect to polarization P_i for each (T, ϵ_0) point one can find the polarization states of the thin film, i.e. one can build the phase diagram.

2.6 Bulk - thin film renormalization of a_{ijk} coefficients

As it was mentioned discussing the scalar model, the high-order electrostrictive as well as nonlinear compliance coefficients lead to the changes in coefficients $a_{ijk}^{\text{bulk}} \rightarrow a_{ijk}^{\text{film}}$ of P^6 -terms while passing from a bulk crystal to the thin film ($G \rightarrow \tilde{G}$). The high-order couplings described by the M_{ijk} , R_{ijk} , and N_{ijk} tensors renormalize the a_{ijk} coefficients of the P^6 -terms of \tilde{G} . The renormalization reads:

$$\begin{aligned} a_{111}^{\text{film}} = a_{111}^{\text{bulk}} - \frac{M_{111}(Q_{11}s_{11} - Q_{12}s_{12})^2}{2(s_{11} - s_{12})^2(s_{11} + s_{12})^2} - \frac{M_{122}(Q_{12}^2s_{11}^2 - 2Q_{11}Q_{12}s_{11}s_{12} + Q_{11}^2s_{12}^2)}{2(s_{11} - s_{12})^2(s_{11} + s_{12})^2} \\ - \frac{R_{112}(-Q_{12}s_{11}^3 + Q_{11}s_{11}^2s_{12} + Q_{12}s_{11}s_{12}^2 - Q_{11}s_{12}^3)}{(s_{11} - s_{12})^2(s_{11} + s_{12})^2} - \frac{R_{111}(-Q_{11}s_{11}^3 + Q_{12}s_{11}^2s_{12} + Q_{11}s_{11}s_{12}^2 - Q_{12}s_{12}^3)}{(s_{11} - s_{12})^2(s_{11} + s_{12})^2} \\ + \frac{M_{112}(-Q_{11}^2s_{11}s_{12} - Q_{12}^2s_{11}s_{12} + Q_{11}Q_{12}(s_{11}^2 + s_{12}^2))}{(s_{11} - s_{12})^2(s_{11} + s_{12})^2} + \\ \frac{(Q_{11} + Q_{12})}{3(s_{11} - s_{12})^2(s_{11} + s_{12})^3} (Q_{11}^2(s_{11}^2N_{111} + s_{11}(N_{111} - 3N_{112})s_{12} + N_{111}s_{12}^2) + \\ Q_{12}^2(s_{11}^2N_{111} + s_{11}(N_{111} - 3N_{112})s_{12} + N_{111}s_{12}^2) - \\ Q_{11}Q_{12}(s_{11}^2(N_{111} - 3N_{112}) + 4s_{11}N_{111}s_{12} + (N_{111} - 3N_{112})s_{12}^2)), \end{aligned} \quad (2.36)$$

2.6. Bulk - thin film renormalization of high-order coefficients

$$a_{333}^{\text{film}} = a_{111}^{\text{bulk}} - \frac{M_{122}Q_{12}^2}{(s_{11} + s_{12})^2} - \frac{M_{123}Q_{12}^2}{(s_{11} + s_{12})^2} + \frac{2Q_{12}R_{112}}{s_{11} + s_{12}} + \frac{2Q_{12}^3(N_{111} + 3N_{112})}{3(s_{11} + s_{12})^3}, \quad (2.37)$$

$$\begin{aligned} a_{112}^{\text{film}} = a_{112}^{\text{bulk}} & - \frac{M_{122}(Q_{11}^2s_{11}(s_{11} - 2s_{12}) + Q_{12}^2s_{12}(-2s_{11} + s_{12}) + 2Q_{11}Q_{12}(s_{11}^2 - s_{11}s_{12} + s_{12}^2))}{2(s_{11} - s_{12})^2(s_{11} + s_{12})^2} - \\ & \frac{M_{112}(Q_{11}Q_{12}(s_{11}^2 - 4s_{11}s_{12} + s_{12}^2) + Q_{11}^2(s_{11} - s_{11}s_{12} + s_{12}^2) + Q_{12}^2(s_{11} - s_{11}s_{12} + s_{12}^2))}{(s_{11} - s_{12})^2(s_{11} + s_{12})^2} - \\ & \frac{M_{155}Q_{44}^2(s_{11}^2 - s_{12}^2)^2}{2(s_{11} - s_{12})^2(s_{11} + s_{12})^2s_{44}^2} - \frac{M_{424}(Q_{11} + Q_{12})Q_{44}}{(s_{11} + s_{12})s_{44}} + \frac{Q_{44}R_{155}(s_{11}^2 - s_{12}^2)^2}{(s_{11} - s_{12})^2(s_{11} + s_{12})^2s_{44}^2} - \\ & \frac{M_{111}(2Q_{11}Q_{12}s_{11}s_{44}^2(s_{11} - s_{12}) + Q_{12}^2s_{11}^2s_{44}^2 - 2Q_{11}^2s_{11}s_{12}s_{44}^2 - 2Q_{11}Q_{12}s_{11}s_{12}s_{44}^2 - 2Q_{12}^2s_{11}s_{12}s_{44}^2 + Q_{11}^2s_{12}^2s_{44}^2)}{2(s_{11} - s_{12})^2(s_{11} + s_{12})^2s_{44}^2} - \\ & \frac{R_{111}(-Q_{12}s_{11}^3s_{44}^2 + Q_{11}s_{11}^2s_{12}s_{44}^2 + Q_{12}s_{11}s_{12}^2s_{44}^2 - Q_{11}s_{12}^3s_{44}^2)}{(s_{11} - s_{12})^2(s_{11} + s_{12})^2s_{44}^2} - \\ & (R_{121}(-2Q_{11}s_{11}^3s_{44}^2 - 2Q_{12}s_{11}^3s_{44}^2 + 2Q_{11}s_{11}^2s_{12}s_{44}^2 + 2Q_{12}s_{11}^2s_{12}s_{44}^2 + 2Q_{11}s_{11}s_{12}^2s_{44}^2 + 2Q_{12}s_{11}s_{12}^2s_{44}^2 - \\ & \quad 2Q_{11}s_{12}^3s_{44}^2 - 2Q_{12}s_{12}^3s_{44}^2))/(s_{11} - s_{12})^2(s_{11} + s_{12})^2s_{44}^2 - \\ & \frac{R_{112}(-Q_{11}s_{11}^3s_{44}^2 + Q_{12}s_{11}^2s_{12}s_{44}^2 + Q_{11}s_{11}s_{12}^2s_{44}^2 - Q_{12}s_{12}^3s_{44}^2)}{(s_{11} - s_{12})^2(s_{11} + s_{12})^2s_{44}^2} + \\ & \frac{(Q_{11} + Q_{12})}{(s_{11} - s_{12})^2(s_{11} + s_{12})^3s_{44}^2} \left(Q_{44}^2(s_{11}^2 - s_{12}^2)^2N_{155} + (Q_{11}^2(s_{11}^2N_{112} - s_{11}(N_{111} + N_{112})s_{12} + N_{112}s_{12}^2) + \right. \\ & \left. Q_{12}^2(s_{11}^2N_{112} - s_{11}(N_{111} + N_{112})s_{12} + N_{112}s_{12}^2) + Q_{11}Q_{12}(s_{11}^2(N_{111} + N_{112}) - 4s_{11}N_{112}s_{12} + (N_{111} + N_{112})s_{12}^2))s_{44}^2 \right), \end{aligned} \quad (2.38)$$

$$\begin{aligned} a_{113}^{\text{film}} = a_{113}^{\text{bulk}} & - \frac{M_{111}Q_{12}(Q_{11}s_{11} - Q_{12}s_{12})}{(s_{11} - s_{12})(s_{11} + s_{12})^2} - \frac{M_{123}(Q_{11}Q_{12}s_{11}^2 - Q_{11}^2s_{11}s_{12} - Q_{12}^2s_{11}s_{12} + Q_{11}Q_{12}s_{12}^2)}{(s_{11} - s_{12})^2(s_{11} + s_{12})^2} - \\ & \frac{M_{112}(Q_{11}Q_{12}s_{11}^2 + Q_{12}^2s_{11}^2 - 2Q_{11}Q_{12}s_{11}s_{12} - 2Q_{12}^2s_{11}s_{12} + Q_{11}Q_{12}s_{12}^2 + Q_{12}^2s_{12}^2)}{(s_{11} - s_{12})^2(s_{11} + s_{12})^2} - \\ & \frac{R_{123}(-2Q_{12}s_{11}^3 + 2Q_{11}s_{11}^2s_{12} + 2Q_{12}s_{11}s_{12}^2 - 2Q_{11}s_{12}^3)}{(s_{11} - s_{12})^2(s_{11} + s_{12})^2} - \\ & \frac{R_{121}(-2Q_{11}s_{11}^3 + 2Q_{12}s_{11}^2s_{12} + 2Q_{11}s_{11}s_{12}^2 - 2Q_{12}s_{12}^3)}{(s_{11} - s_{12})^2(s_{11} + s_{12})^2} - \\ & \frac{R_{111}(-Q_{12}s_{11}^3 + Q_{12}s_{11}^2s_{12} + Q_{12}s_{11}s_{12}^2 - Q_{12}s_{12}^3)}{(s_{11} - s_{12})^2(s_{11} + s_{12})^2} - \frac{R_{112}(-Q_{12}s_{11}^3 + Q_{12}s_{11}^2s_{12} + Q_{12}s_{11}s_{12}^2 - Q_{12}s_{12}^3)}{(s_{11} - s_{12})^2(s_{11} + s_{12})^2} - \\ & \frac{M_{122}(2Q_{11}Q_{12}s_{12}(-3s_{11} + s_{12}) + Q_{11}^2(s_{11}^2 + s_{12}^2) + Q_{12}^2(3s_{11}^2 - 2s_{11}s_{12} + s_{12}^2))}{2(s_{11} - s_{12})^2(s_{11} + s_{12})^2} + \\ & \frac{Q_{12}}{(s_{11} - s_{12})^2(s_{11} + s_{12})^3} (4Q_{11}Q_{12}(s_{11}^2N_{112} - s_{11}(N_{111} + N_{112})s_{12} + N_{112}s_{12}^2) + Q_{11}^2(s_{11}^2(N_{111} + N_{112}) - \\ & \quad 4s_{11}N_{112}s_{12} + (N_{111} + N_{112})s_{12}^2) + Q_{12}^2(s_{11}^2(N_{111} + N_{112}) - 4s_{11}N_{112}s_{12} + (N_{111} + N_{112})s_{12}^2)), \end{aligned} \quad (2.39)$$

$$\begin{aligned} a_{133}^{\text{film}} = a_{112}^{\text{bulk}} & - \frac{M_{111}Q_{12}^2}{2(s_{11} + s_{12})^2} - \frac{M_{112}Q_{12}^2}{(s_{11} + s_{12})^2} - \frac{M_{123}Q_{12}(Q_{11} + Q_{12})}{(s_{11} + s_{12})^2} - \frac{M_{122}Q_{12}(2Q_{11} + 3Q_{12})}{2(s_{11} + s_{12})^2} + \\ & \frac{R_{112}(Q_{11}s_{11} + Q_{12}s_{11} + Q_{11}s_{12} + Q_{12}s_{12})}{(s_{11} + s_{12})^2} + \frac{R_{121}(2Q_{12}s_{11} + 2Q_{12}s_{12})}{(s_{11} + s_{12})^2} + \frac{R_{123}(2Q_{12}s_{11} + 2Q_{12}s_{12})}{(s_{11} + s_{12})^2} + \\ & \frac{Q_{12}^2(Q_{11} + Q_{12})(N_{111} + 3N_{112})}{(s_{11} + s_{12})^3}, \end{aligned} \quad (2.40)$$

$$\begin{aligned}
a_{123}^{\text{film}} = a_{123}^{\text{bulk}} &- \frac{2M_{112}Q_{12}(Q_{11}+Q_{12})}{(s_{11}+s_{12})^2} + \frac{2M_{111}Q_{12}(-s_{11}+s_{12})(Q_{12}s_{11}-Q_{11}s_{12})}{(s_{11}-s_{12})^2(s_{11}+s_{12})^2} - \\
&\frac{M_{123}(-4Q_{11}Q_{12}s_{11}s_{12}+Q_{11}^2(s_{11}^2+s_{12}^2)+Q_{12}^2(s_{11}^2+s_{12}^2))}{(s_{11}-s_{12})^2(s_{11}+s_{12})^2} + \\
&\frac{2M_{122}(Q_{11}^2s_{11}s_{12}+Q_{12}^2(2s_{11}-s_{12})s_{12}-Q_{11}Q_{12}(2s_{11}^2-s_{11}s_{12}+s_{12}^2))}{(s_{11}-s_{12})^2(s_{11}+s_{12})^2} - \frac{M_{144}Q_{44}^2(s_{11}^2-s_{12}^2)^2}{2(s_{11}-s_{12})^2(s_{11}+s_{12})^2s_{44}^2} - \\
&\frac{2M_{424}Q_{12}Q_{44}}{(s_{11}+s_{12})s_{44}} + \frac{2Q_{44}R_{144}(s_{11}^2-s_{12}^2)^2}{(s_{11}-s_{12})^2(s_{11}+s_{12})^2s_{44}} - \\
&\frac{R_{123}(4Q_{11}s_{11}(s_{11}+s_{12})(-s_{11}+s_{12})s_{44}^2+4Q_{12}(-s_{11}-s_{12})s_{12}(-s_{11}+s_{12})s_{44}^2)}{(s_{11}-s_{12})^2(s_{11}+s_{12})^2s_{44}^2} - \\
&(R_{121}(8Q_{12}s_{11}(s_{11}+s_{12})(-s_{11}+s_{12})s_{44}^2+4Q_{11}(-s_{11}-s_{12})s_{12}(-s_{11}+s_{12})s_{44}^2+ \\
&4Q_{12}(-s_{11}-s_{12})s_{12}(-s_{11}+s_{12})s_{44}^2))/((s_{11}-s_{12})^2(s_{11}+s_{12})^2s_{44}^2) + \\
&\frac{2Q_{12}N_{111}(2Q_{11}Q_{12}s_{11}^2s_{44}^2-2Q_{11}^2s_{11}s_{12}s_{44}^2-2Q_{12}^2s_{11}s_{12}s_{44}^2+2Q_{11}Q_{12}s_{12}^2s_{44}^2)}{(s_{11}-s_{12})^2(s_{11}+s_{12})^3s_{44}^2} + \\
&\frac{2Q_{12}Q_{44}^2(s_{11}^2-s_{12}^2)^2N_{155}}{(s_{11}-s_{12})^2(s_{11}+s_{12})^3s_{44}^2} + \\
&(2Q_{12}N_{112}(2Q_{11}^2s_{11}^2s_{44}^2+2Q_{11}Q_{12}s_{11}^2s_{44}^2+2Q_{12}^2s_{11}^2s_{44}^2-2Q_{11}^2s_{11}s_{12}s_{44}^2- \\
&8Q_{11}Q_{12}s_{11}s_{12}s_{44}^2-2Q_{12}^2s_{11}s_{12}s_{44}^2+2Q_{11}^2s_{12}^2s_{44}^2+2Q_{11}Q_{12}s_{12}^2s_{44}^2+2Q_{12}^2s_{12}^2s_{44}^2))/ \\
&((s_{11}-s_{12})^2(s_{11}+s_{12})^3s_{44}^2)
\end{aligned} \tag{2.41}$$

Note that in (2.35) solutions were expanded in series and only low order terms of the expansion were kept, then σ_1 , σ_2 and σ_6 were substituted into (2.34), therefore expressions (2.36 - 2.41) result from the expansion in series in (2.35).

2.7 Ab initio calculations

To see what impact high-order interactions exert on the thin film effective potential \tilde{G} (2.34), one has to know the values of the high-order electrostrictive and non-linear compliance coefficients. Since the experimental information on the high-order coefficients is scarce we turned towards ab initio methods, namely, we used the Vienna Ab-initio Simulation Package (VASP) [54] performing zero Kelvin Density Functional Theory (DFT) full relaxation calculations. All calculations were performed within the Generalized Gradient Approximation PW91 (GGA-PW91) [55] as implemented in VASP using the projector augmented-wave method for the electron-ion interactions [56]. We have used a 8x8x8 Monkhorst-Pack grid for k-point sampling [57], and a plane-wave energy cut-off of 600eV. For full relaxation calculations, the threshold of the Hellman-Feynman force was 1meV/Å. We would like to underline that mechanical compliance and electrostriction in (2.8) are expected to be weakly temperature dependent. This justifies the use of zero Kelvin DFT results in finite temperature calculations. All other analytical and numerical calculations to solve Landau theory equations including plotting thin film misfit-strain temperature phase diagrams, etc. were performed with Wolfram Mathematica software.

Technically, because of working with DFT, it is more convenient to use the F expansion (2.9) to calculate the high-order coefficients. Stiffness c_{ij} and n_{ijk} and electrostrictive q_{ij} , m_{ijk} ,

and r_{ijk} coefficients can be found in the following way. Using VASP we can find stress σ_i on strain ϵ_j and polarization P_i on strain ϵ_j dependences for different geometries (for different i and j). Then, using the mechanical state equation

$$\sigma_{ij} = \frac{\partial G}{\partial \epsilon_{ij}} = c_{ijkl}\epsilon_{kl} + n_{ijklmn}\epsilon_{kl}\epsilon_{mn} - q_{kl ij}P_kP_l - m_{klmni j}P_kP_l\epsilon_{mn} - r_{klmni j}P_kP_lP_mP_n, \quad (2.42)$$

we determine the coefficients by fitting. Polarization was calculated by the atomic displacements $\xi_{p,j}$ and Born charges for the cubic phase $Z_{p,ij}$:

$$P_i = \frac{e}{v} Z_{p,ij} \xi_{p,j}, \quad (2.43)$$

where p enumerates the atoms in the unit cell, e - the charge of electron, v - volume of the cubic unit cell. The Born charges $Z_{p,ij}$ for BTO were obtained with VASP.

$$\begin{aligned} Q_{\text{Ba}} &= \begin{pmatrix} 2.34 & 0 & 0 \\ 0 & 2.34 & 0 \\ 0 & 0 & 2.34 \end{pmatrix} \\ Q_{\text{Ti}} &= \begin{pmatrix} 7.90 & 0 & 0 \\ 0 & 7.90 & 0 \\ 0 & 0 & 7.90 \end{pmatrix} \\ Q_{\text{O1}} &= \begin{pmatrix} -2.17 & 0 & 0 \\ 0 & -2.17 & 0 \\ 0 & 0 & -6.29 \end{pmatrix} \\ Q_{\text{O2}} &= \begin{pmatrix} -2.17 & 0 & 0 \\ 0 & -6.29 & 0 \\ 0 & 0 & -2.17 \end{pmatrix} \\ Q_{\text{O3}} &= \begin{pmatrix} -6.29 & 0 & 0 \\ 0 & -2.17 & 0 \\ 0 & 0 & -2.17 \end{pmatrix} \end{aligned} \quad (2.44)$$

It is possible to find c_{ij} and n_{ijk} tensors separately from others (q_{ij} , m_{ijk} , and r_{ijk}) if one uses the mechanical state equation (2.42) at zero polarization and models the deformation applied to the paraelectric cubic phase keeping the mmm symmetry of the structure. For example, the mechanical state equation (2.42) at zero polarization and only ϵ_1 nonzero component gives:

$$\sigma_1 = c_{11}\epsilon_1 + n_{111}\epsilon_1^2. \quad (2.45)$$

The $\sigma_1(\epsilon_1)$ dependence obtained with VASP shown in Fig. 2.1 are inserted into Eq. (2.45) and the corresponding c_{11} and n_{111} coefficients are obtained by fitting.

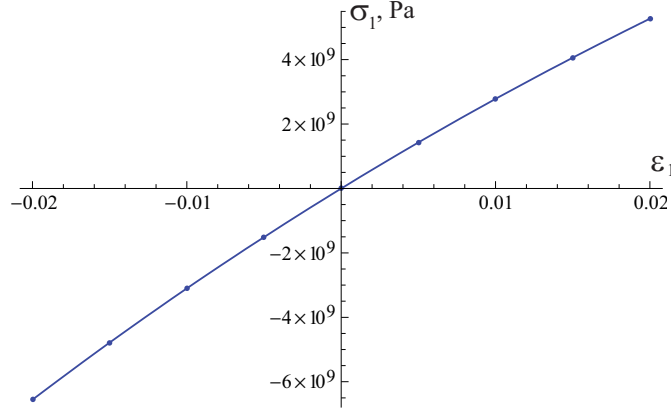


Figure 2.1: Modeled stress σ_1 on strain ϵ_1 dependence for BaTiO₃. Obtained with VASP keeping the mmm symmetry of the structure.

Then, the other q_{ij} , m_{ijk} , and r_{ijk} coefficients can be found from analysis of all of Eq. (2.42). Let us demonstrate how to find the q_{11} , m_{111} and r_{111} tensors components. One uses Eq. (2.42) where only polarization P_1 and strain ϵ_1 are nonzero:

$$\sigma_1 = c_{11}\epsilon_1 + n_{111}\epsilon_1^2 - q_{11}P_1^2 - m_{111}P_1^2\epsilon_1 - r_{111}P_1^4, \quad (2.46)$$

Performing VASP full relaxation calculations keeping the $4mm$ tetragonal symmetry of the structure, we find the $P_1(\epsilon_1)$ and $\sigma_1(\epsilon_1)$ dependences using polynomial fit. Then, we put them into Eq. (2.46). Once we have polynomial functions of ϵ_1 on the both sides of Eq. (2.46) we obtain q_{11} , m_{111} and r_{111} by fitting. By repeating this procedure for different symmetries of the structure and for different components of σ_i and ϵ_j it is possible to calculate all the components of the high-order electrostrictive tensors.

The above described scheme requires a good accuracy of $\sigma_i(\epsilon_j)$ and $P_i(\epsilon_j)$ dependences. Unfortunately, because of the technical limitations of software we can not have reliable precision of the curvature of $\sigma_i(\epsilon_j)$ and $P_i(\epsilon_j)$ and therefore reliable precision of r_{ijk} coefficients. We clarify the matter with the example where only $\sigma_1(\epsilon_1)$ and $P_1(\epsilon_1)$ are nonzero. One represents $\sigma_1(\epsilon_1)$ and $P_1^2(\epsilon_1)$ dependences obtained with VASP as

$$\begin{aligned} \sigma_1(\epsilon_1) &= \sigma_1(0) + \sigma_1'(0)\epsilon_1 + \sigma_1''(0)\epsilon_1^2, \\ P_1^2(\epsilon_1) &= \rho_0 + \rho_1\epsilon_1 + \rho_2\epsilon_1^2 \end{aligned} \quad (2.47)$$

and inserts them into Eq. (2.46). Equating coefficients of powers of ϵ_1 one has 3 independent equations:

$$\sigma_1(0) = -q_{11}\rho_0 - r_{111}\rho_0^2, \quad (2.48)$$

$$\sigma_1'(0) = c_{11} - q_{11}\rho_1 - 2m_{111}\rho_0 - 2r_{111}\rho_0\rho_1, \quad (2.49)$$

$$\sigma_1''(0) = n_{111} - q_{11}\rho_2 - 2m_{111}\rho_1 - r_{111}(\rho_1^2 + 2\rho_0\rho_2) \quad (2.50)$$

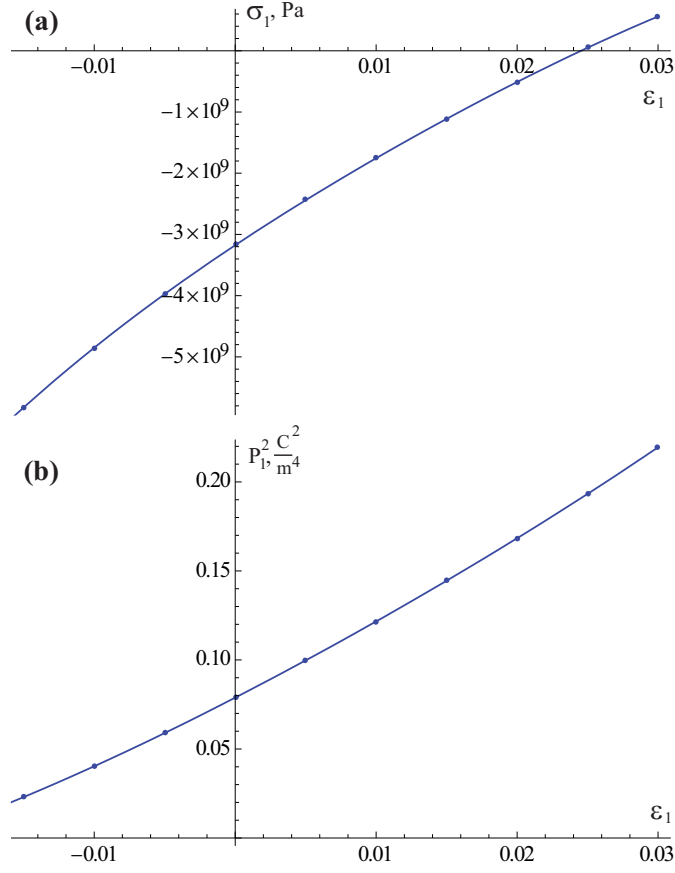


Figure 2.2: Modeled stress σ_1 on strain ϵ_1 (a) and square of polarization P_1^2 on strain ϵ_1 (b) dependences for BaTiO₃. Obtained with VASP full relaxation calculations keeping the $4mm$ tetragonal symmetry of the structure.

to find simultaneously 3 unknown values of q_{11} , m_{111} , and r_{111} . This way one has to consider the second derivatives of $\sigma_1(\epsilon_1)$ and $P_1(\epsilon_1)$ dependences (Eq. (2.50)) which cannot be reliably found with VASP. This is supported by the fact that the r_{ijk} values found with VASP are in conflict with those obtained with experimental data. Thus, we do not attempt to calculate the r_{ijk} coefficients, and this way we use only the two lower-order independent equations. We realize that the exclusion of r_{ijk} can cause the change of m_{ijk} in (2.49), but the numerical calculations show that this leads to a small correction of m_{ijk} .

The coefficients are calculated with errors as it can be seen from Table 2.2. The origin of the error of the coefficients is due to the computational limit of VASP causing the calculation error of atomic displacements and therefore polarization (which was calculated by atomic displacements) and stress σ . Additionally, the calculation scheme described above is iterative, one needs to use previously found coefficients to calculate new ones. For example, to find a coefficient m_{112} which corresponds to the term

$$F = \dots - \frac{m_{112}}{2} P_1^2 \epsilon_1 \epsilon_2 + \dots \quad (2.51)$$

one uses the mechanical equation of state keeping only P_1 , ϵ_1 and ϵ_2 components:

$$\frac{\partial F}{\partial \epsilon_1} = \sigma_1 = c_{11}\epsilon_1 + c_{12}\epsilon_2 + c_{111}\epsilon_1^2 + 2c_{112}\epsilon_1\epsilon_2 - q_{11}P_1^2 - m_{111}P_1^2\epsilon_1 - m_{112}P_1^2\epsilon_2. \quad (2.52)$$

From (2.52) by setting $\epsilon_1 = \epsilon_2 = \epsilon$ we can write:

$$\sigma_1(\epsilon) = (c_{11} + c_{12})\epsilon + (c_{111} + 2c_{112})\epsilon^2 - q_{11}P_1^2 - (m_{111} + m_{112})P_1^2\epsilon, \quad (2.53)$$

Then, keeping $\epsilon_1 = \epsilon_2 = \epsilon$ we find the $\sigma_1(\epsilon)$ and $P_1(\epsilon)$ dependences with first principles methods. Knowing $\sigma_1(\epsilon)$ and $P_1(\epsilon)$, the m_{112} coefficient can be found from (2.53), since the other (except m_{112}) coefficients in (2.53) are known from the previous steps. The $\sigma_1(\epsilon)$ and $P_1(\epsilon)$ dependences obtained with VASP have some errors as well as the previously found c_{11} , c_{12} , c_{111} , c_{112} , q_{11} , and m_{111} coefficients. So, when the m_{112} coefficient is calculated it contains an accumulating error of all previously found coefficients and clearly has lower precision than for example m_{111} .

2.8 Experimental estimates of R_{ijk} coefficients

Due to the technical limitations of VASP we are unable to reliably determine the r_{ijk} coefficients. Luckily we can estimate some of the R_{ijk} coefficients using experimental information on piezoelectric coefficients and spontaneous polarization and strain. From (2.8) one can proceed to the linearized constitutive equations for the piezoelectric coefficient d_{ij} , defined as

$$d_{ij} = \left(\frac{\partial \epsilon_j}{\partial E_i} \right)_{\sigma_i=0}, \quad (2.54)$$

and spontaneous strain ϵ_S . For BaTiO₃ in the tetragonal phase we have:

$$d_{33} = \chi_{33} \frac{\partial}{\partial P_3} \left(\frac{\partial G}{\partial \sigma_3} \right) = 2Q_{11}P_S\chi_{33} + 4R_{111}P_S^3\chi_{33} \quad (2.55)$$

$$\epsilon_{S3} = -\frac{\partial G}{\partial \sigma_3} = Q_{11}P_S^2 + R_{111}P_S^4 \quad (2.56)$$

$$d_{31} = \chi_{33} \frac{\partial}{\partial P_3} \left(\frac{\partial G}{\partial \sigma_1} \right) = 2Q_{12}P_S\chi_{33} + 4R_{112}P_S^3\chi_{33} \quad (2.57)$$

$$\epsilon_{S1} = -\frac{\partial G}{\partial \sigma_1} = Q_{12}P_S^2 + R_{112}P_S^4 \quad (2.58)$$

$$d_{15} = \chi_{11} \frac{\partial}{\partial P_1} \left(\frac{\partial G}{\partial \sigma_5} \right) = 2P_SQ_{44}\chi_{11} + 4R_{155}P_S^3\chi_{11}, \quad (2.59)$$

where $P_S = 0.26 \frac{\text{C}}{\text{m}^2}$ [58] is the spontaneous polarization, $\chi_{33} = 168\epsilon_0$ and $\chi_{11} = 2920\epsilon_0$ [9] are the dielectric susceptibilities. Eqs. (2.55)-(2.59) can be appended with the equation for the

spontaneous stain in the orthorhombic phase:

$$\epsilon_{S5} = -\frac{\partial G}{\partial \sigma_5} = Q_{44} \frac{P_S^2}{2} + R_{155} \frac{P_S^4}{4}, \quad (2.60)$$

where for P_S we take the same value of $0.26 \frac{\text{C}}{\text{m}^2}$ since the absolute value of P_S does not appreciably change during the phase transition from the tetragonal to the orthorhombic phase [58], there is only a rotation of polarization vector. Resolving Eqs. (2.55)-(2.60) and using experimental data on d_{ij} and ϵ_{Si} from Table 2.1 one can estimate the Q_{ij} and R_{ijk} values which are also shown in Table 2.1. Thus, three out of six components of the R_{ijk} tensor can be found within this method. While we have a relatively good precision of the Q_{ij} coefficients within few percents, the error bars of the R_{ijk} coefficients can reach some 30% of their value (except R_{155} , where the error can be up to 100% in view of the smallness of the latter).

$d_{ij}, [10^{-12} \frac{\text{C}}{\text{N}}]$	ϵ_{Si}	$Q_{ij}, [\frac{\text{m}^4}{\text{C}^2}]$	$R_{ijk}, [\frac{\text{m}^8}{\text{C}^4}]$
$d_{33} = 85.6$	$\epsilon_{S3} = 0.0077$	$Q_{11} = 0.118$	$R_{111} = -0.08$
$d_{31} = -34.5$	$\epsilon_{S1} = -0.0027$	$Q_{12} = -0.036$	$R_{112} = -0.07$
$d_{15} = 240$	$\epsilon_{S5} = 0.00105$	$Q_{44} = 0.032$	$R_{155} = -0.02$

Table 2.1: Some experimental material parameters of BaTiO₃. d_{ij} - piezoelectric coefficients, the values are taken from Ref. [9]. ϵ_{Si} is the spontaneous strain, $\epsilon_{S3} = \frac{c-a_0}{a_0}$ and $\epsilon_{S1} = \frac{a-a_0}{a_0}$, where $c = 4.034 \text{ \AA}$ and $a = 3.992 \text{ \AA}$ are the lattice parameters of the tetragonal cell, $a_0 = 4.003 \text{ \AA}$ is the lattice constant of cubic BaTiO₃ extrapolated to room temperature [10], ϵ_{S5} is recalculated from the distortion angle $\beta = 89^\circ 51.6'$ [10] of orthorhombic cell. Q_{ij} and R_{ijk} are linear and non-linear electrostriction calculated from experimental data.

2.9 Results and discussion

The coefficients of ordinary and high-order electrostriction as well as linear and non-linear elastic compliances obtained with the first principles calculations for the F expansion were recalculated for G . The analytic expressions of the recalculations can be found in section 2.4 and Eq. (2.12). The values of recalculated coefficients are given in Table 2.2. In the table we compare the obtained c_{ij} stiffness coefficients with experiment, the corresponding s_{ij} values needed for the thin film diagram plotting, one can find with the following expressions:

$$\begin{aligned} s_{11} &= \frac{c_{11} + c_{12}}{c_{11}^2 + c_{12}c_{11} - 2c_{12}^2}, \\ s_{12} &= -\frac{c_{12}}{c_{11}^2 + c_{12}c_{11} - 2c_{12}^2}, \\ s_{44} &= \frac{1}{c_{44}}. \end{aligned} \quad (2.61)$$

We should note that current DFT methods give relatively moderate precision for high-order coefficients as it is clear from the error bars in Table 2.2 due to technical limitations of the

Chapter 2. Can we trust thin film diagrams?

software and due to the neglect of the r_{ijk} coefficients in the used scheme as it was described above.

$c_{ij}, (\times 10^{11} \text{Pa})$		$c_{ij}^{\text{exp}}, (\times 10^{11} \text{Pa})$		$M_{ijk}, \left(10^{-12} \frac{\text{m}^4}{\text{C}^2 \text{Pa}}\right)$		$N_{ijk}, \left(10^{-23} \frac{1}{\text{Pa}^2}\right)$	
c_{11}	2.94 ± 0.01	c_{11}	2.75	M_{111}	-2.6 ± 0.2	N_{111}	8 ± 1
c_{12}	1.08 ± 0.01	c_{12}	1.79	M_{112}	1.3 ± 0.5	N_{112}	< 2
c_{44}	1.18 ± 0.01	c_{44}	1.13	M_{122}	3.5 ± 0.5	N_{123}	< 2
				M_{123}	-1.0 ± 0.5	N_{144}	< 2
$Q_{ij}, \left(\frac{\text{m}^4}{\text{C}^2}\right)$		$Q_{ij}^{\text{exp}}, \left(\frac{\text{m}^4}{\text{C}^2}\right)$		M_{144}	< 1	N_{155}	< 2
Q_{11}	0.162 ± 0.005	Q_{11}	0.11	M_{155}	1.5 ± 1	N_{456}	< 4
Q_{12}	-0.034 ± 0.005	Q_{12}	-0.043	M_{414}	< 1		
Q_{44}	0.021 ± 0.005	Q_{44}	0.029	M_{424}	< 1		
				M_{456}	< 1		

Table 2.2: Some materials parameters of BaTiO₃ obtained from ab initio calculations. s_{ij} and N_{ijk} are linear and nonlinear elastic compliance, Q_{ij} and M_{ijk} are linear and high-order electrostrictive tensors respectively. Experimental values of c_{ij} (from [7]) and Q_{ij} (from [1]) are also given for comparison.

The renormalized a_{ijk}^{film} coefficients are obtained using relationships (2.36)-(2.41) and data from the Table 2.2. Table 2.3 demonstrates the size of the $a_{ijk}^{\text{bulk}} \rightarrow a_{ijk}^{\text{film}}$ renormalization effect for BaTiO₃ where the components of the original (a_{ijk}^{bulk}) and renormalized (a_{ijk}^{film}) tensors as well as the renormalizing corrections (Δa_{ijk}) are given.

	a_{ijk}^{bulk}	$\Delta a_{ijk}^{\text{by } M_{ijk} \& R_{ijk}}$	$\Delta a_{ijk}^{\text{by } N_{ijk}}$	a_{ijk}^{film}
a_{111}	7.9	0.5 ± 0.5	1.4 ± 0.2	9.8 ± 0.5
a_{333}		0.8 ± 0.5	< 0.2	8.7 ± 0.5
a_{112}	4.5	-10.6 ± 0.5	1.5 ± 0.2	-4.6 ± 0.5
a_{113}		-5.0 ± 0.5	-1.3 ± 0.2	-1.8 ± 0.5
a_{133}		0.5 ± 0.5	0.5 ± 0.2	5.5 ± 0.5
a_{123}	4.9	7.1 ± 0.5	1.4 ± 0.2	13.4 ± 0.5

Table 2.3: Renormalization of the coefficients of the P^6 -terms when passing from the thermodynamic potential of a bulk material G to the effective potential of a film \tilde{G} . All values are given in $10^9 \frac{\text{m}^9}{\text{C}^4 \text{F}}$ at 300K. a_{ijk}^{bulk} are coefficients of the expansion G for bulk and mechanically free BaTiO₃. Δa_{ijk} are corrections to corresponding a_{ijk}^{bulk} coefficients representing an addition to a_{ijk}^{bulk} (for example, $a_{333}^{\text{film}} = a_{111}^{\text{bulk}} + \Delta a_{333}$). a_{ijk}^{film} are coefficients of the \tilde{G} energy of the (001)-oriented clamped film.

An inspection of this table shows that the renormalization is strong, e.g. $a_{123}^{\text{bulk}} = 4.9 \times 10^9 \frac{\text{m}^9}{\text{C}^4 \text{F}}$ while $a_{123}^{\text{film}} = 13.9 \times 10^9 \frac{\text{m}^9}{\text{C}^4 \text{F}}$ which means more than a 100% change, confirming the conclusion drawn above from the order-of-magnitude estimates.

Further we demonstrate the influence of high-order terms on the temperature - misfit strain phase diagram for a single-domain (001)-oriented BaTiO₃ thin film. To plot the diagram, one

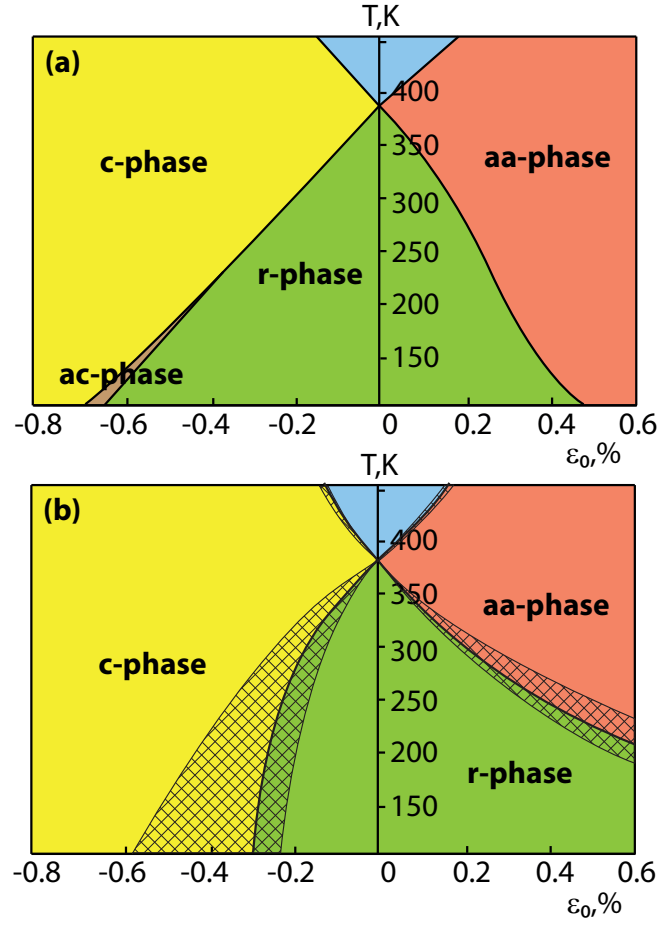


Figure 2.3: Temperature - misfit strain phase diagrams of a single-domain (001)-oriented BaTiO_3 . ϵ_0 - biaxial parent misfit strain, T - temperature. The phases are denoted as (i) the c-phase (yellow), polarization is out-of-plane ($P_1 = P_2 = 0, P_3 \neq 0$); (ii) the aa-phase (red), where polarization is in-plane ($P_1 \neq 0, P_2 \neq 0, P_3 = 0$); (iii) the ac-phase (brown) where $P_1 \neq 0, P_2 = 0, P_3 \neq 0$; (iv) r-phase (red), where all components of polarization are non-zero; and (v) paraelectric phase (blue), polarization is 0. (a) Original Pertsev's diagrams built with coefficients from Ref. [1]. (b) Developed with coefficients set from Ref. [1] appended with high-order M_{ijklmn} , R_{ijklmn} and N_{ijklmn} coefficients. The hatched regions demonstrate the shift of the transition lines within the error bars of the coefficients.

minimizes the above obtained thin film effective potential $\tilde{G}(P_i, T, \epsilon_0)$ (2.34) with respect to polarization P_i for each (T, ϵ_0) point. A comparison between Figs. 2.3(a) and 2.3(b) shows how the original phase diagram built with the coefficients from Ref. [1] changes when supplemented with the high-order electrostrictive and nonlinear compliance coefficients (Table 2.2) evaluated from first principles calculations and experimental data. From Figs. 2.3(a) and 2.3(b) one can see that taking into account the high-order coefficients strongly changes the diagram. The effect might have been much stronger, but positive P^4 -terms of \tilde{G} leading to the second-order phase transition in the film [1] diminish the role of the strongly renormalized a_{ijk} coefficients. The hatched regions in Fig. 2.3(b) demonstrate the shift of the transition

lines within the error bars of the coefficients. It is seen that the diagram is extremely sensitive to the variation of the high-order coefficients.

Another striking feature of the data from Table 2.3 is the negative sign of some of a_{ijk}^{film} , making the renormalized theory formally unstable. However, we found that, physically, the situation can be treated as stable. The point is that the potential \tilde{G} of the thin film still has local minima due to the positive sign of renormalized coefficients for P^4 -terms of the thermodynamic potential of the film [1], therefore the system is locally stable. As for the global stability, it can be restored by adding P^8 -terms in the G expansion [59]. We do not incorporate these terms in our consideration, however we believe that this will not essentially affect the positions of the local minima in view of very high power of the terms.

We would like to note that the above results have implications on finite temperature MC simulations. To perform MC simulations for perovskites one customarily uses an effective Hamiltonian incorporating ordinary electrostriction [50, 60]. In view of our findings, we suggest that for the treatment of ferroelectric thin films the effective Hamiltonian has to also include high-order electromechanical interactions and nonlinear elasticity.

2.10 Conclusions

To summarize, in this chapter it was shown that an adequate Landau theory treatment of thermodynamics of typical ferroelectric thin films requires taking into account high-order electromechanical couplings and non-linear elasticity. The high-order electromechanical couplings were for the first time calculated using first principles methods. Our analysis suggests that all Landau theory based simulation of ferroelectric thin films should take into account not only customarily incorporated "ordinary electrostriction type" coupling, but also the high-order electromechanical interactions. In view of this finding, we believe that an experimental evaluation of high-order electromechanical couplings in ferroelectrics seems to be a task of primary importance.

3 FBARs tuning from first principles

Another example, demonstrating the importance of taking into account the high-order electrostrictive coefficients, is tunable thin Film Bulk Acoustic wave Resonators (FBARs). In this chapter, first, we introduce tunable FBARs and review their applications. Then, we consider a theory of FBARs tuning and using ab initio methods we determine the coefficients needed for FBARs tuning description. Further, using ab initio results the tuning of $\text{Ba}_x\text{Sr}_{1-x}\text{TiO}_3$ (BST) based tunable FBARs was studied. Finally, we present the results and discussion of the obtained results.

3.1 Introduction to Film Bulk Acoustic wave Resonators

Highly selective Radio Frequency (RF) bandpass filters are absolutely essential for multichannel microwave communication systems and specifically for mobile phones which nowadays constitute the largest market for RF resonators. RF bandpass filters are needed to avoid interference between different wireless communication systems and to protect receive and transmit passes from the interference of disturbing signals. Traditionally the band selecting filters are based on Surface Acoustic Wave (SAW) technology. The SAW filters provide good selectivity in the frequency range below 2 GHz. However, their overall performance degrades closer to the upper limit of mobile phone frequency bands (about 2 GHz).

Surface acoustic wave based sensors are also widely used, for example, in biosensing [61] where such sensors provide high sensitivity for the detection of biomolecules in liquids. However these devices do not scale well with RF applications at higher frequencies since their sub-micrometer sizes decrease the power handling capabilities.

Small size, high Q-factor values, and applicability to high frequencies are the driving forces for the development of the FBAR technology for GHz-range applications. FBAR devices use thin piezoelectric (typically AlN [62–65] or ZnO [66, 67]) films to transform an electrical signal into an acoustical wave which can resonate at a certain frequency in the acoustically isolated body of the resonator. The acoustic waves in FBARs propagate perpendicular to the surfaces

of the film (thickness waves) which are mainly used in microwave filters [68]. Presently FBARs are commercially available and the filters based on fixed frequency FBARs are regarded as one of the most promising technologies to address the performance/cost requirements of microwave communications systems [69]. However these piezoelectric-effect-based FBARs are non-tunable, their resonance frequency is fixed by geometry and size of the resonator and piezoelectric material used.

At the same time modern trends of IC architecture simplification and miniaturisation, improvement of transceiver/receiver performance, reducing power consumption in mobile devices, and reduction of weight, size and cost [70] give rise for the development of tunable FBARs. Tunable FBARs based on $\text{Ba}_x\text{Sr}_{1-x}\text{TiO}_3$ ferroelectric films in the paraelectric phase were proposed and patented in 2004 by Gevorgian [21, 71]. Tunable FBARs (at about 5 GHz) with tuning range up to 4% [72] and Q-factors of more than 350 [73] were reported. Tunable FBARs exploiting BST ferroelectric films in the paraelectric phase possess no ferroelectric hysteresis which is extremely important for the circuit applications of these devices.

One distinguishes two tuning modes of tunable FBARs based on ferroelectric thin films: thickness extension (TE) and lateral field excitation (LFE) modes [23]. For the TE mode, the direction of the applied DC bias E_{DC} (as well as induced polarization P_{DC}) is parallel to the travelling direction of the acoustic wave (perpendicular to the film surface). For the LFE mode, the applied DC bias is in the plane of the film and perpendicular to the travelling direction of the acoustic wave. The TE mode is a standard and practically used realisation of modern tunable FBARs, so that hereafter in this chapter, we are going to deal with the TE mode only.

For practical application as tunable microwave filters, the simultaneous tuning of the resonance and antiresonance frequencies is highly desired [70]. At the same time, for BST compositions the antiresonance tuning is normally much smaller than that of the resonance which makes the realisation of tunable filters using BST based tunable FBARs difficult. This problem is of high interest nowadays and provokes research in the field.

A simple theory of tunable FBARs based on the DC-bias-induced piezoelectric effect was developed recently by Noeth et al. [23, 74] and by Vendik et al. [22] where it was shown that, for antiresonance frequency tuning, it is important to take into account the high-order electrostrictive coefficient m_{111} . In these papers as m_{111} values were unknown for BST, they were taken from order-of-magnitude estimations. This work answers some questions which remain to be addressed. What is the sign of m_{111} coefficients for BST and the sign of the corresponding shift of the antiresonance frequency of tunable FBARs? Is it possible to have comparable shifts of resonance and antiresonance frequencies that is essential to produce a tunable filter?

In this chapter the high-order electrostrictive coefficient as well as stiffness and linear electrostriction were calculated using ab initio methods. To improve the reliability of the obtained results we used two different software packages: Vienna Ab-initio Simulation Package (VASP) and Quantum ESPRESSO (QE). Then using ab initio results and theory developed in Ref.

[23], the tuning of BST based tunable FBARs was studied. Finally we present the results and discussion of the obtained results.

3.2 Description of FBARs tuning

A theory of tunable FBARs based on the DC bias induced piezoelectric effect was developed recently by Noeth et al [23, 74]. Here we recall essential aspects. The treatment is based on a Landau free energy expansion for the cubic phase in terms of the ferroelectric part of polarization P and strain u .

$$F = \alpha_i P_i^2 + \beta_{ij} P_i^2 P_j^2 + \frac{1}{2} c_{ij}^0 u_i u_j - q_{ij} P_i^2 u_j - \frac{1}{2} m_{ijk} P_i^2 u_j u_k, \quad (3.1)$$

where c^0 - stiffness of free bulk sample, q and m - linear and nonlinear electrostriction respectively. In this case dielectric displacement D_i is defined as

$$D_i = \epsilon_b E_i + P_i, \quad (3.2)$$

where ϵ_b is the background permittivity and E_i is the electric field. We include in our treatment a nonlinear electrostrictive coefficient m which was previously considered as a higher-order correction and customarily neglected [75], but which actually plays an important role in the antiresonance frequency tuning of tunable FBARs [22, 23, 74].

Let us consider a tunable FBAR operating in the TE mode based on a [001]-oriented BST thin ferroelectric film in the paraelectric phase. DC field induced tuning of acoustic resonance of paraelectric phase BST films are demonstrated experimentally for $x \leq 0.5$ [76], therefore we limit our consideration to these BST compositions. A schematic drawing of a resonator using the TE mode is shown in Fig. 3.1. representing a parallel-plate capacitor of thickness t , where

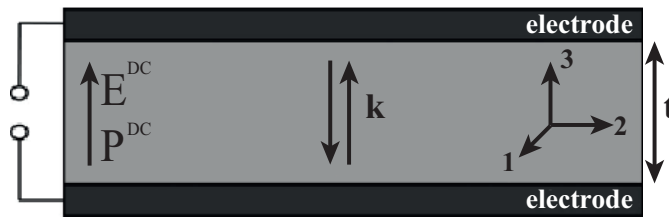


Figure 3.1: A schematic drawing of the TE mode resonator. The DC bias E^{DC} and polarization P^{DC} is parallel to the direction of the traveling acoustic wave with the wave vector k .

the acoustic wave with the wave vector k resonates in the thickness direction along the X_3 axis parallel to the applied field. Applied between the electrodes the electric field consists of large DC E_3^{DC} and small AC E_3^{AC} components:

$$E_3^{\text{tot}} = E_3^{DC} + E_3^{AC}, \quad (3.3)$$

Chapter 3. FBARs tuning from first principles

The electric field induces polarization in the film which can also be split into DC and AC parts:

$$P_3^{\text{tot}} = P_3^{\text{DC}} + P_3^{\text{AC}}. \quad (3.4)$$

Values of induced polarization P_3^{DC} can be found by solving a cubic equation [70]:

$$E_3^{\text{DC}} = \alpha_3^* P_3^{\text{DC}} + \beta_{33}^* (P_3^{\text{DC}})^3, \quad (3.5)$$

where α^* and β^* correspond to the coefficients of a clamped film. Explicit expressions of α^* and β^* for the [001] thin films clamped on the substrate can be found elsewhere [1].

From (3.1) one can proceed to the linearised constitutive equations [23] written for a tunable FBAR (Fig. 3.1) using the TE mode:

$$\begin{aligned} D_3 &= \epsilon_{33} E_3^{\text{AC}} + e_{33} u_3 \\ \sigma_3 &= c_{33}^E u_3 - e_{33} E_3^{\text{AC}} \end{aligned} \quad (3.6)$$

where D - electric displacement, σ stress, e - electric field induced effective piezoelectric coefficient, c^E - stiffness coefficient at constant field. The dielectric constant ϵ_{33} consists of a background part ϵ^b and a field dependent part χ_{33} :

$$\epsilon_{33} = \epsilon^b + \chi_{33}, \quad \chi_{33} = \frac{1}{\alpha_3^* + \beta_{33}^* (P_3^{\text{DC}})^2} \quad (3.7)$$

The DC bias applied to centrosymmetric BST crystal leads to internal atom displacements and induced piezoelectricity with an effective piezoelectric constant e :

$$e_{33} = 2\chi_{33} q_{33} P_3^{\text{DC}}. \quad (3.8)$$

Tunability of acoustic resonance of tunable FBARs is also achieved due to the DC field dependent stiffness c^E :

$$c_{33}^E = c_{33}^0 + (m_{333} + 4q_{33}^2 \chi_{33}) (P_3^{\text{DC}})^2, \quad (3.9)$$

where c^0 is stiffness in the absence electric field.

This way, the AC field via the induced piezoelectric effect, (3.8), causes an acoustic wave travelling in the film. From (3.6), the impedance Z can be derived by taking into account the mechanical wave equation, mechanical boundary conditions, and the Poisson equation [77]:

$$Z(\omega) = \frac{1}{i\omega C_0} \left(1 - k_t^2 \frac{\tan(kt/2)}{kt/2} \right), \quad (3.10)$$

where ω is the AC field angular frequency, C_0 is the clamped capacitance, and k is the wave

vector of the longitudinal wave. The wave vector k and the electromechanical coupling factor k_t are defined as [77]:

$$k = \frac{\omega}{\sqrt{c_{33}^D/\rho}} \quad (3.11)$$

$$k_t^2 = \frac{e_{33}^2}{c_{33}^D \epsilon_{33}} \quad (3.12)$$

where ρ is the density of the material and the elastic constant c^D at fixed dielectric displacement is

$$c_{33}^D = c_{33}^E + \frac{e_{33}^2}{\epsilon_{33}}. \quad (3.13)$$

Using Eqs. (3.7), (3.9), and (3.13) and neglecting the difference between $\epsilon_{33} = \chi_{33} + \epsilon_b$ and χ_{33} for large χ_{33} (normally for ferroelectric materials $\chi_{33} \gg \epsilon_b$), one can express c_{33}^D as

$$c_{33}^D = c_{33}^0 - m_{333}(P_3^{DC})^2 - \frac{e_{33}^2 \epsilon^b}{\epsilon_{33}^2}. \quad (3.14)$$

One can see in (3.14) that the c_{33}^D tuning is carried out by two terms. The first one, $m_{333}(P_3^{DC})^2$, is determined by non-linear electrostriction m_{333} and the second one, $\frac{e_{33}^2 \epsilon^b}{\epsilon_{33}^2}$, we will call it electrostrictive, is driven by the induced piezoelectric coefficient, e_{33} .

In the TE mode the relations for the resonance f_R and the antiresonance frequency f_{AR} [in Hz] are given by [77]:

$$f_R = \frac{1}{2t} \sqrt{\frac{c_{33}^D}{\rho} \left(1 - \frac{8k_t^2}{\pi^2}\right)}, \quad (3.15)$$

$$f_{AR} = \frac{1}{2t} \sqrt{\frac{c_{33}^D}{\rho}} \quad (3.16)$$

In Ref. [23] it was shown that the resonance frequency tuning (3.15) is stronger than the antiresonance one. It happens because of the field dependance of electromechanical coupling factor k_t is much stronger than that of the elastic constant c_{33}^D according to order-of-magnitude estimations, and for the resonance tuning 3.15 the change of c_{33}^D can be neglected. However, for the antiresonance frequency tuning, (3.16), c_{33}^D fully determines the antiresonance behaviour (3.16). To determine the shift of c_{33}^D under applied field and in turn to determine the shift of f_{AR} one has to know the m_{333} coefficient which is not yet available experimentally.

The theory discussed above deals with tunable FBARs based on the BST films in the cubic paraelectric phase and therefore the expansion of free energy (3.1) is written for a cubic

material. Due to the $m\bar{3}m$ symmetry of tensors in (3.1), one can write that $m_{111} = m_{222} = m_{333}$. Further we will always use the m_{111} notation.

3.3 Ab initio calculations

To find the high-order electrostrictive coefficients m_{111} for BaTiO₃ and SrTiO₃ we turned towards ab initio methods, namely, we used 2 programs, PWSCF (Plane-Wave Self-Consistent Field) being part of QE package [78] and VASP [54] performing zero Kelvin Density Functional Theory (DFT) full relaxation calculations.

All VASP calculations were performed within the generalized-gradient approximation (GGA) with the Perdew-Burke-Ernzerhof (PBE) exchange-correlation functional [79] as implemented in VASP using the projector augmented-wave method for the electron-ion interactions [56]. We have used a 8x8x8 Monkhorst-Pack grid for k-point sampling [57], and a plane-wave energy cut-off of 600eV to yield convergence. For full relaxation calculations, the threshold of the Hellman-Feynman force was 1meV/Å.

QE calculations were also made within the GGA PBE exchange-correlation functional with ultrasoft pseudopotential by Vanderbilt [80]. We have used an automatically generated uniform 8x8x8 grid of k-points, the kinetic energy cutoff for wavefunctions was 60Ry (816eV). The convergence threshold on forces for ionic minimization was chosen to be equal to 5×10^{-5} a.u. (1.3 meV/Å).

The starting point for our calculations was a relaxed cubic phase with lattice parameters $a_0 = 4.0268\text{Å}$ (QE) and $a_0 = 4.0351\text{Å}$ (VASP) for BaTiO₃, and $a_0 = 3.9383\text{Å}$ (QE) and $a_0 = 3.9479\text{Å}$ (VASP) for SrTiO₃.

Here we would like to underline that mechanical and electro-mechanical constants, like mechanical stiffness and electrostriction defined as coefficients of free energy expansion (3.1), are expected to be weakly temperature dependent. This justifies the use of zero Kelvin DFT results in finite temperature tunable FBARs simulations.

Let us demonstrate the way we found the stiffness c_{11} and electrostrictive q_{11} , m_{111} coefficients. From VASP and QE we directly have atomic displacements and stress σ_i applied to the structure for a certain deformation value u_i . Then, polarization was calculated using (2.43).

The Born charges calculated with QE are

$$\begin{aligned}
 Q_{\text{Ba}} &= \begin{pmatrix} 2.74 & 0 & 0 \\ 0 & 2.74 & 0 \\ 0 & 0 & 2.74 \end{pmatrix} \\
 Q_{\text{Ti}} &= \begin{pmatrix} 7.44 & 0 & 0 \\ 0 & 7.44 & 0 \\ 0 & 0 & 7.44 \end{pmatrix} \\
 Q_{\text{O1}} &= \begin{pmatrix} -2.14 & 0 & 0 \\ 0 & -2.14 & 0 \\ 0 & 0 & -5.91 \end{pmatrix} \\
 Q_{\text{O2}} &= \begin{pmatrix} -2.14 & 0 & 0 \\ 0 & -5.91 & 0 \\ 0 & 0 & -2.14 \end{pmatrix} \\
 Q_{\text{O3}} &= \begin{pmatrix} -5.91 & 0 & 0 \\ 0 & -2.14 & 0 \\ 0 & 0 & -2.14 \end{pmatrix}
 \end{aligned} \tag{3.17}$$

for BTO and

$$\begin{aligned}
 Q_{\text{Sr}} &= \begin{pmatrix} 2.55 & 0 & 0 \\ 0 & 2.55 & 0 \\ 0 & 0 & 2.55 \end{pmatrix} \\
 Q_{\text{Ti}} &= \begin{pmatrix} 7.37 & 0 & 0 \\ 0 & 7.37 & 0 \\ 0 & 0 & 7.37 \end{pmatrix} \\
 Q_{\text{O1}} &= \begin{pmatrix} -2.03 & 0 & 0 \\ 0 & -2.03 & 0 \\ 0 & 0 & -5.87 \end{pmatrix} \\
 Q_{\text{O2}} &= \begin{pmatrix} -2.03 & 0 & 0 \\ 0 & -5.87 & 0 \\ 0 & 0 & -2.03 \end{pmatrix} \\
 Q_{\text{O3}} &= \begin{pmatrix} -5.87 & 0 & 0 \\ 0 & -2.03 & 0 \\ 0 & 0 & -2.03 \end{pmatrix}
 \end{aligned} \tag{3.18}$$

for STO.

Using the energy expansion (3.1) and setting $P_i = 0$ (paraelectric phase), one can write a

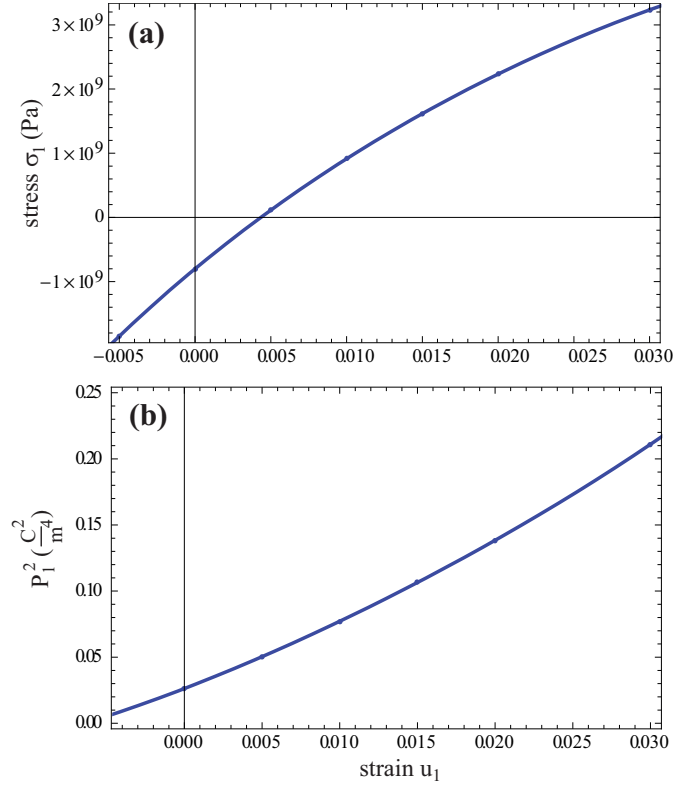


Figure 3.2: Modeled stress σ_1 on strain u_1 (a) and square of polarization P_1^2 on strain u_1 (b) dependences in the vicinity of zero strain for SrTiO₃. Obtained with VASP full relaxation calculations keeping the $4mm$ tetragonal symmetry of the structure.

mechanical equation of state for Ox_1 direction:

$$\frac{\partial F}{\partial u_1} = \sigma_1 = c_{11} u_1, \quad (3.19)$$

where applied deformation was calculated as $u_1 = \frac{c-a_0}{a_0}$. Then, with DFT methods, keeping the mmm symmetry of the structure, we model the $\sigma_1(u_1)$ dependence. Fitting $\sigma_1(u_1)$ with polynomial function, we can find c_{11} coefficient.

Next, for other q_{11} and m_{111} coefficients, using ab initio full relaxation calculations and keeping the $4mm$ tetragonal symmetry of the structure, we find $P_1(u_1)$ and $\sigma_1(u_1)$ dependences (Fig. 3.2). The obtained dependences are expanded in series in the vicinity of $u_1 = 0$:

$$\sigma_1(u_1) = \sigma_1(0) + \sigma_1'(0) u_1 + \sigma_1''(0) u_1^2, \quad (3.20)$$

$$P_1^2(u_1) = \rho_0 + \rho_1 u_1 + \rho_2 u_1^2 \quad (3.21)$$

and substituted into the mechanical equation written for the case where only the P_1 compo-

ment of polarization and the u_1 component of strain are nonzero:

$$\frac{\partial F}{\partial u_1} = \sigma_1 = c_{11}u_1 - q_{11}P_1^2 - m_{111}P_1^2u_1. \quad (3.22)$$

Equating coefficients of powers of u_1 one has two low-order independent equations:

$$\sigma_1(0) = -q_{11}\rho_0 \quad (3.23)$$

$$\sigma_1'(0) = c_{11} - q_{11}\rho_1 - m_{111}\rho_0 \quad (3.24)$$

to find the q_{11} and m_{111} values.

We do not incorporate the nonlinear stiffness coefficient n_{111} into (3.22) since the $n_{111}u_1^2$ term would be a higher-order correction. We clarify the matter as follows. Let us consider Eq. (3.22) supplemented with nonlinear stiffness:

$$\sigma_1 = c_{11}u_1 + n_{111}u_1^2 - q_{11}P_1^2 - m_{111}P_1^2u_1. \quad (3.25)$$

Equating coefficients of powers of u_1 as before, additionally to (3.23) and (3.24) one has the third equation:

$$\sigma_1''(0) = n_{111} - q_{11}\rho_2 - m_{111}\rho_1. \quad (3.26)$$

Thus, n_{111} does not enter the two lower-order equations ((3.23) and (3.24)) and can be excluded from the consideration.

3.4 Results and discussion

The coefficients of ordinary and high-order electrostriction as well as elastic stiffness obtained with the first principles calculations are given in Table 3.1. Two sets of constants calculated with VASP and QE as well as experimental data are given for comparison. Analysis of Table 3.1 shows that one has a good agreement between our calculated stiffness coefficients and experiment. At the same time, it is difficult to compare the obtained q_{11} electrostriction values with experimental results in view of the two-times spread of the latter. Meanwhile, our q_{11} values are 10-20% close to the values taken from Landolt and Bornstein, which gives us reason to believe that the predicted m_{111} values are a reasonable approximation. The main reason for the inaccuracy of the obtained coefficients in Table 3.1 is the errors appearing due to the software technical limitations of the determination of the relaxed atomic positions and therefore the determination of polarization and stress.

Based on electro-mechanical coefficients obtained with VASP calculations and taking into account the small difference of obtained values for the end members of BST solid solution

	VASP	QE	Experiment
SrTiO ₃ ($x = 0$)			
$c_{11}, 10^{11} \frac{\text{N}}{\text{m}^2}$	3.28 ± 0.02	3.17 ± 0.02	$3.18^a, 3.16^b$
$q_{11}, 10^{10} \frac{\text{m}}{\text{F}}$	3.0 ± 0.1	2.9 ± 0.1	$1.20^a, 2.53^b$
$m_{111}, 10^{11} \frac{\text{m}}{\text{F}}$	-2.2 ± 0.4	-3.0 ± 0.4	-
BaTiO ₃ ($x = 1$)			
$c_{11}, 10^{11} \frac{\text{N}}{\text{m}^2}$	2.91 ± 0.02	2.82 ± 0.02	$2.83^a, 2.55^b$
$q_{11}, 10^{10} \frac{\text{m}}{\text{F}}$	4.0 ± 0.1	3.6 ± 0.1	$1.43^a, 2.81^b$
$m_{111}, 10^{11} \frac{\text{m}}{\text{F}}$	-2.8 ± 0.4	-2.8 ± 0.4	-

Table 3.1: Data obtained with the first principles calculations. c_{11} - stiffness, q_{11} and m_{111} - linear and nonlinear electrostriction coefficients. (a) Experimental data were taken or recalculated from Ref. [11]. (b) Data were taken or recalculated from Landolt and Bornstein [7].

(Table 3.1) we used a linear interpolation for the dependences $c_{11}(x)$, $q_{11}(x)$, $m_{111}(x)$:

$$c_{11}(x) = 3.28 \times 10^{11} - 3.7 \times 10^{10} x \frac{\text{N}}{\text{m}^2} \quad (3.27)$$

$$q_{11}(x) = 3.04 \times 10^{10} + 9.3 \times 10^9 x \frac{\text{m}}{\text{F}} \quad (3.28)$$

$$m_{111}(x) = -2.2 \times 10^{11} - 6 \times 10^{10} x \frac{\text{m}}{\text{F}} \quad (3.29)$$

The common way to characterise the tunability of a material is to use the relative tunability n_r defined as

$$n_r = \frac{\epsilon(0) - \epsilon(E^{DC})}{\epsilon(0)}, \quad (3.30)$$

where $\epsilon(0)$ and $\epsilon(E^{DC})$ correspond to the permittivity at zero field and under DC bias, respectively.

Using (3.14)-(3.16) and (3.27)-(3.29) one can plot the tuning of resonance, $\frac{f_r - f_0}{f_0}$, and antiresonance, $\frac{f_{ar} - f_0}{f_0}$, frequencies depending on n_r , where f_0 is the resonance frequency extrapolated to zero DC field:

$$f_0 = \frac{1}{2t} \sqrt{\frac{c_{33}^0}{\rho}}. \quad (3.31)$$

These dependences for the tunable FBAR using the [001]-oriented thin film of some BST compositions are shown in Fig. 3.3. The resonance tuning is larger for BST compositions with

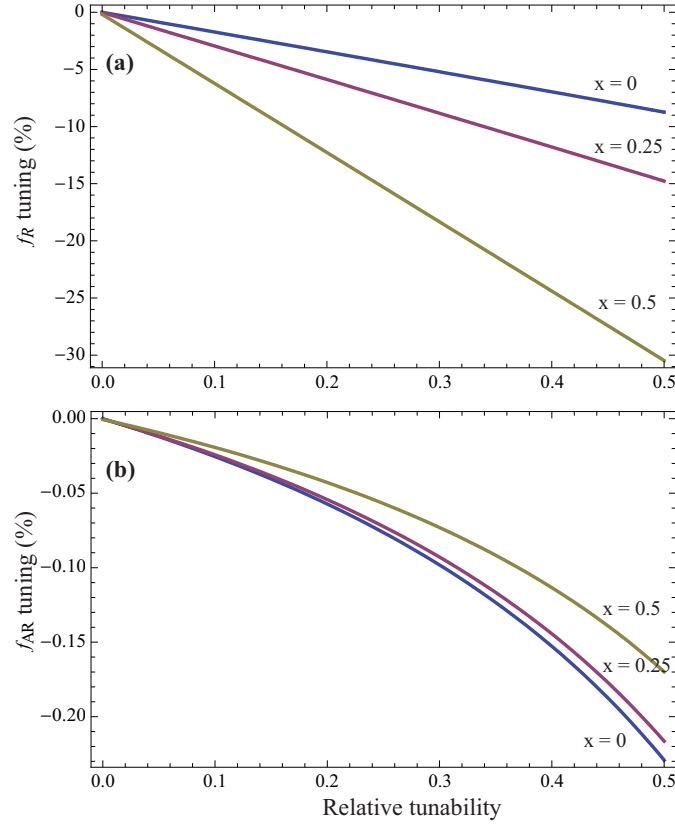


Figure 3.3: Modeled dependences of resonance (a) and antiresonance (b) frequency tuning on relative tunability n_r for the tunable FBAR using the [001]-oriented thin film of different BST compositions. Parameters used in calculations like stiffness, linear and non-linear electrostriction are taken from Table 3.1. Other used parameters are taken from Ref. [4]: $\alpha = \frac{1}{\epsilon_0} \frac{T - T_0(x)}{C_{CW}(x)}$, $T = 300\text{K}$, $T_0(x) = (42 + 439.37x - 96x^2)\text{K}$, $C_{CW}(x) = (0.86 + 1.1x^2)10^5\text{K}$, $\beta = 8(1 - x)10^9 \frac{\text{m}^5}{\text{C}^2\text{F}}$, and $\epsilon_b = 7\epsilon_0$.

higher x because of increasing values of $q_{11}(x)$ (3.28) which via k_t (3.12) govern the tuning. The shift of the antiresonance frequency is much smaller than that of the resonance. The reason for such a difference in behaviour of resonance and antiresonance can be explained as follows. A tunable FBAR resonator can be represented as an equivalent parallel LC circuit and its antiresonance corresponds to infinite impedance Z of such a circuit. The $Z = \infty$ means $D_3 = 0$ on the plates of the tunable FBAR which in turn leads to a presence of the depolarising field inside. The depolarising field reduces the amplitude of the polarization wave and therefore suppresses the electromechanical coupling between polarization and strain. So, the contribution of linear electrostriction is reduced and the tuning starts to be sensitive to higher-order effects. This way, for antiresonance tuning, the non-linear electrostriction m_{111} becomes important for consideration. On the contrary, the resonance corresponds to $Z = 0$ of the equivalent serial LC circuit which means $\langle E_3 \rangle = 0$. Therefore, the average depolarizing field inside the resonator is zero and there is almost no reduction of polarization-strain coupling, and therefore the contribution of m_{111} as a higher-order effect is negligible.

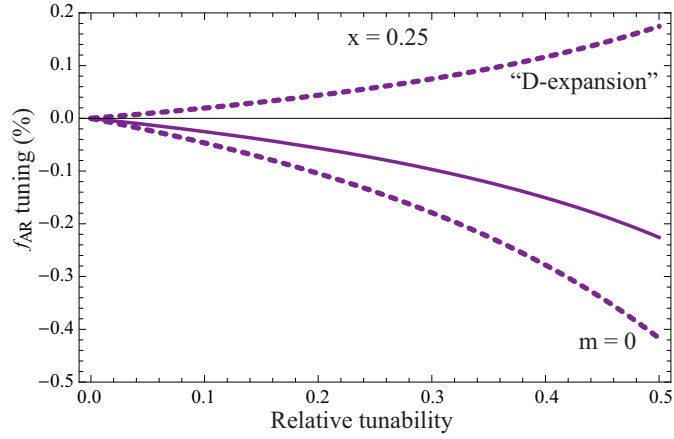


Figure 3.4: Modeled dependences of the antiresonance frequency tuning on relative tunability n_r for the tunable FBAR using the [001]-oriented thin film of BST with $x = 0.25$. Dashed lines show the antiresonance behaviour without taking into account m_{111} and the behaviour resulting from "D-expansion" of Landau free energy.

The shift of the antiresonance frequency is specified by two competing terms $m_{333}(P_3^{DC})^2$ and $\frac{e_{33}^2 e_{33}^b}{\epsilon_{33}^2}$ (see (3.14)) which are actually equally responsible for the antiresonance tuning. We would like to underline that it is important to use thermodynamic energy expansion in terms of polarization ("P-expansion") and not in terms of dielectric displacement ("D-expansion"). In Ref. [22] where the electromechanical properties of tunable FBARs were treated based on the "D-expansion" of free energy, the $\frac{e_{33}^2 e_{33}^b}{\epsilon_{33}^2}$ term does not appear leading to erroneous results. In Fig. 3.4, the antiresonance tuning without taking into account m_{111} and the tuning resulting from "D-expansion" are shown with dashed lines for a BST composition with $x = 0.25$. The previously unknown m_{111} coefficient was found to be negative and therefore responsible for the positive shift of f_{AR} , at the same time the electrostrictive contribution in (3.14) gives negative shift. This way there is a compensation of two contributions in (3.14) which leads to weaker tuning than what was expected from order-of-magnitude estimations.

Additionally, it is instructive to plot resonance and antiresonance frequency tuning depending on applied DC bias (Figure 3.5). We cannot directly compare our results obtained for the (001)-oriented single-domain BST thin film with experiment in view of limited experimental data, available mostly for polydomain films [70]. At the same time, it is still useful to have a look on the available experimental results. In Ref. [81] a membrane-type tunable FBAR based on a $\text{Ba}_{0.3}\text{Sr}_{0.7}\text{TiO}_3$ 650 nm thick thin film was fabricated by means of microfabrication. The polydomain film with a (001)/(111) preferred orientation was deposited on a 100 nm thick bottom Pt electrode which in turn was placed on a 100 nm thick SiO_2 layer. The maximum archived tuning was about -2.4% and -0.6% for the resonance and antiresonance frequencies respectively at a DC electric field of 615 kV/cm which corresponds to $n_r = 0.5$. Our results for $x = 0.25$ and DC bias of 615 kV/cm show the resonance tuning of -20% and antiresonance of -0.7% (Figure 3.5). Our calculations show the similar antiresonance tuning value, but

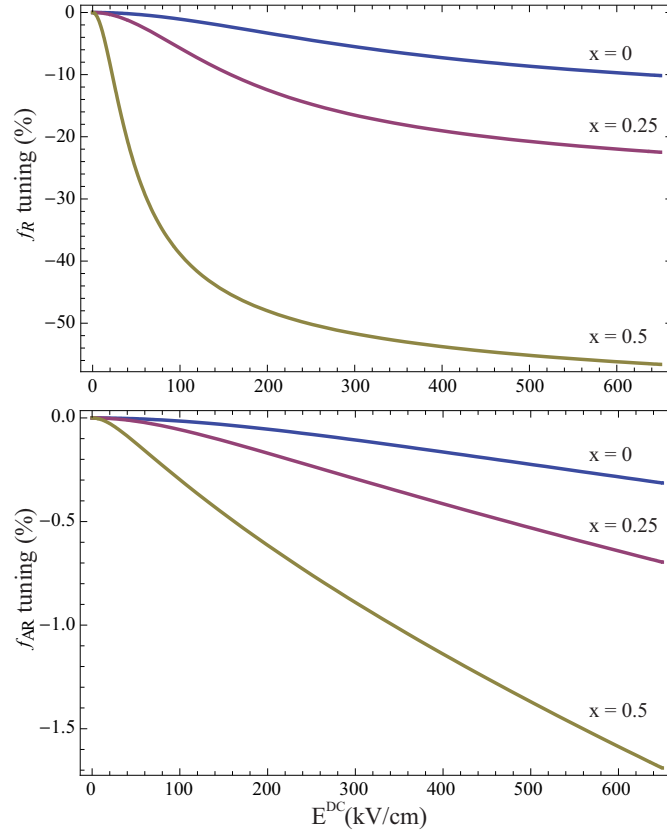


Figure 3.5: Modeled dependences of the resonance (a) and antiresonance (b) frequency tuning on applied DC bias for the tunable FBAR using the [001]-oriented thin film of different BST compositions. Parameters used in calculations like stiffness, linear and non-linear electrostriction are taken from Table 3.1. Other used parameters are taken from Ref. [4]: $\alpha = \frac{1}{\epsilon_0} \frac{T - T_0(x)}{C_{CW}(x)}$, $T = 300\text{K}$, $T_0(x) = (42 + 439.37x - 96x^2)\text{K}$, $C_{CW}(x) = (0.86 + 1.1x^2)10^5\text{K}$, $\beta = 8(1 - x)10^9 \frac{\text{m}^5}{\text{C}^2\text{F}}$, and $\epsilon_b = 7\epsilon_0$.

the resonance tuning values are much larger than experimental results. The reason of such difference of the resonance tuning values is that our calculations were performed for the (001)-oriented single domain film, whereas the experiment were done with (001)/(111)-oriented polydomain film deposited on the SiO_2 layer and loaded with Pt electrodes. First, the effective values of q_{11} electrostriction for the (111)-oriented film are few times lower than the true value of q_{11} [23], that eventually leads to the smaller electromechanical coupling factor k_t and correspondingly to the lower resonance tuning. Second, the frequency tuning of pure BST material is expected to be reduced by the presence of electrodes and substrates.

3.5 Conclusions

A high-order m_{111} electrostrictive coefficient being important for antiresonance frequency tuning of tunable FBARs was for the first time calculated using ab initio methods for BaTiO_3

and SrTiO₃. Since the m_{111} values were found negative and close to each other for the both materials, we determined m_{111} for BST compositions using a linear interpolation. Based on the results obtained with first principles calculations we simulated the resonance and antiresonance tuning of the BST based tunable FBAR. Our calculations confirm that when studying tunable FBARs tuning one should use the P-expansion of the Landau free energy which allows taking into account the electrostrictive contribution to the shift of the antiresonance frequency. It was established that there is a compensation of linear and non-linear electrostrictive contributions to the antiresonance tuning which leads to the fact that the tuning was found to be smaller than expected from previously made estimations.

4 Positive effective Q_{12} electrostrictive coefficients in perovskites

Nowadays materials science is focused on creation and engineering of new materials and composites with unusual properties. Among them are composites and forms with negative Poisson's ratio [82–84], which expand laterally in tension and contract laterally in compression, metamaterials with negative compressibility [85] exhibiting transitions, during which a material undergoes contraction when tensioned (or expansion when pressured). Using of these unusual mechanical properties in applications pushes the limits of design of modern devices such as actuators, force amplifiers, micromechanical controls, and protective devices.

Even more important and widely used nowadays are electromechanical properties. To exhibit a deformation under the application of an electric field, is a common property of solids. Historically, this phenomena was called electrostriction and it implied both a linear converse piezoelectric effect and a quadric effect with respect to polarization, i.e. electrostriction. The electrostrictive effect, being quadratic, is typically weaker than the piezoelectric one. At the same time, in materials of interest for applications, primarily ferroelectrics, the piezoelectric effect has its disadvantages, for example it shows hysteresis which is undesirable for actuator applications [12], while electrostriction in centrosymmetric materials is free of this drawback. Electrostriction plays an essential role in physics and applications of solids. First of all, electrostriction is of importance for the ferroelectric thin film strain engineering [86] as we saw in the chapter 2. The strain engineering dealing with thin films strained on the substrates pursues the fabrication more environmentally preferable materials. In the clamped thin films electrostriction leads to major effects as a shift of Curie temperature, an increase of remanent polarization, and a change of the order of the phase transition. In relaxor ferroelectrics, in view of their high dielectric constant, the electrostrictive effect can be used for hysteresis-free actuator applications [12]. In chapter 3 we learned that electrostriction is important for tunable FBARs. Ordinary FBARs based on piezoelectric thin films resonate at certain frequency of the applied AC electric field depending on the acoustic velocity of the material and geometry of the FBAR [62, 66]. In tunable FBARs based on ferroelectric films, piezoelectricity is induced by applying DC bias in such a way that the resonance frequency can be tuned. It is electrostriction that is responsible for this tuning as well as for the modification

of other properties as elastic constants and dielectric permittivity [23, 71]. Tunable FBARs can be used for many applications like in sensors, voltage-controlled tunable resonators and filters [87, 88].

It is generally believed that in perovskite ferroelectrics the electrostrictive effect leads to expansion of the sample along the applied electric field and its contraction in the perpendicular direction. In terms of the so-called stress-polarization electrostrictive coefficients Q_{ij} it means that Q_{11} is positive and Q_{12} is negative [1, 5, 6]. However, this is not a general rule for ferroelectrics. For example, some of the ferroelectric polymers from the polyvinylidene fluoride (PVDF) family can exhibit the opposite behaviour [89, 90]. Here a reasonable question arises: is the "extension along the field and contraction perpendicular to it" rule general for perovskites or is it rather a feature of the crystallographic orientation of the sample? This chapter addresses this question showing that the "extension along the field and contraction perpendicular to it" rule can be readily violated if the sample is cut obliquely to the cubic crystallographic directions, notably electrostrictive expansion in all direction can be possible.

4.1 Effective Q_{12} electrostrictive coefficients in crystals

To answer this question, let us consider a bar of perovskite material in the cubic paraelectric phase cut obliquely in a direction which differs by angle θ from the [001] crystallographic axis (see Fig. 4.1). The oblique cut direction changes in the (110)-plane and passes from [001] to [111] and then to [110]-directions. To explore the electrostrictive strain behaviour, one applies an electrical field \vec{E} which in turn induces polarization \vec{P} parallel to the field ($\vec{P} = \chi\vec{E}$ for cubic material) in the oblique cut direction. The polarization \vec{P} in the sample

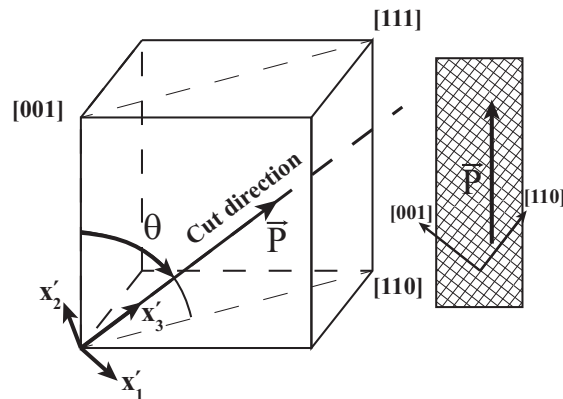


Figure 4.1: Direction of polarization described by angle θ and the rotated reference frame (x'_1, x'_2, x'_3) associated with it. The polarization direction changes in plane going from [001] to [111] and then to the [110] direction.

4.1. Effective electrostrictive coefficients in perovskite crystals

$$\vec{P} = \begin{pmatrix} \frac{\sqrt{2}}{2} \sin \theta \\ \frac{\sqrt{2}}{2} \sin \theta \\ \cos \theta \end{pmatrix} \quad (4.1)$$

in turn induces electrostrictive strain ϵ_{kl} :

$$\epsilon_{kl} = Q_{ijkl} P_i P_j \quad (4.2)$$

where Q_{ijkl} is the electrostrictive tensor. We now change to the Voigt matrix notation [53]

$$\begin{aligned} \epsilon_{ij} &= \epsilon_n \text{ for } n = 1, 2, 3 \\ \epsilon_{ij} &= \frac{\epsilon_n}{2} \text{ for } n = 4, 5, 6, \end{aligned}$$

defining electrostrictive tensor Q_{mn} according to the Landolt-Bornstein reference book [7]:

$$\begin{aligned} Q_{ijkl} &= Q_{mn} \text{ for } n = 1, 2, 3 \\ Q_{ijkl} &= \frac{Q_{mn}}{2} \text{ for } n = 4, 5, 6. \end{aligned}$$

In Voigt notation the electrostrictive strain ϵ appeared in the sample reads as

$$\epsilon = \begin{pmatrix} \epsilon_1 \\ \epsilon_1 \\ \epsilon_3 \\ \epsilon_4 \\ \epsilon_4 \\ \epsilon_6 \end{pmatrix}, \quad (4.3)$$

where

$$\begin{aligned} \epsilon_1 &= P^2 \left(\frac{1}{2} (Q_{11} + Q_{12}) \sin^2 \theta + Q_{12} \cos^2 \theta \right) \\ \epsilon_3 &= P^2 (Q_{11} \cos^2 \theta + Q_{12} \sin^2 \theta) \\ \epsilon_4 &= \sqrt{2} P^2 Q_{44} \cos \theta \sin \theta \\ \epsilon_6 &= P^2 Q_{44} \sin^2 \theta \end{aligned}$$

Chapter 4. Positive effective electrostrictive coefficients in perovskites

In the Cartesian reference frame (x'_1, x'_2, x'_3) with the x'_3 axis parallel to the direction of the oblique cut (see Fig. 4.1), the strain tensor has the form:

$$\epsilon' = \begin{pmatrix} P^2 Q_{12}^{\theta(1)} \\ P^2 Q_{12}^{\theta(2)} \\ P^2 Q_{11}^{\theta} \\ P^2 Q_{44}^{\theta} \\ 0 \\ 0 \end{pmatrix}, \quad (4.4)$$

where

$$\begin{aligned} Q_{11}^{\theta} &= \frac{1}{32} ((6Q_{11} - 6Q_{12} - 3Q_{44}) \cos(4\theta) + (8Q_{11} - 4(2Q_{12} + Q_{44})) \cos(2\theta) + \\ &\quad 18Q_{11} + 14Q_{12} + 7Q_{44}) \\ Q_{12}^{\theta(1)} &= \frac{1}{8} (- (2Q_{11} - 2Q_{12} - Q_{44}) \cos(2\theta) + 2Q_{11} + 6Q_{12} - Q_{44}) \\ Q_{12}^{\theta(2)} &= \frac{1}{32} (- (6Q_{11} - 3(2Q_{12} + Q_{44})) \cos(4\theta) + 6Q_{11} + 26Q_{12} - 3Q_{44}) \\ Q_{44}^{\theta} &= -\frac{1}{32} (2Q_{11} - 2Q_{12} - Q_{44}) (2 \sin(2\theta) + 3 \sin(4\theta)) \end{aligned} \quad (4.5)$$

are the effective electrostrictive components. $\epsilon'_3 = P^2 Q_{11}^{\theta}$ is parallel to the cut direction, $\epsilon'_1 = P^2 Q_{12}^{\theta(1)}$ and $\epsilon'_2 = P^2 Q_{12}^{\theta(2)}$ are perpendicular to it. For $\theta = 0$, for typical cubic perovskites BaTiO₃, SrTiO₃, and PbTiO₃ $Q_{11}^{\theta} = Q_{11} > 0$ while $Q_{12}^{\theta(1)} = Q_{12}^{\theta(2)} = Q_{12} < 0$ (see Table 4.1) and the "extension along the field and contraction perpendicular to it" rule holds. In answering the question of whether this rule is violated for the oblique orientation of the sample, we are interested in whether the signs of Q_{11}^{θ} , $Q_{12}^{\theta(1)}$, and $Q_{12}^{\theta(2)}$ depend on the value of angle θ .

		BaTiO ₃ [5]	SrTiO ₃ [6]	PbTiO ₃ [1]
Q_{11} ,	$\frac{\text{m}^4}{\text{C}^2}$	0.10	0.046	0.089
Q_{12} ,	$\frac{\text{m}^4}{\text{C}^2}$	-0.034	-0.013	-0.026
Q_{44} ,	$\frac{\text{m}^4}{\text{C}^2}$	0.029	0.020	0.068

Table 4.1: Electrostrictive coefficients which were used for calculations, for BaTiO₃ coefficients were taken from [5], for SrTiO₃ from [6], and PbTiO₃ from [1]. The Q_{44} values are written taking into account the factor of 2 as defined in Landolt-Bornstein [7].

We start with an issue relevant to the problem. The field-induced relative change of the sample volume is given by the trace of the deformation tensor, which is independent of the direction of the cut:

$$\text{Tr}(\epsilon_{ij}) = P^2 (Q_{11}^{\theta} + Q_{12}^{\theta(1)} + Q_{12}^{\theta(2)}) = P^2 (Q_{11} + 2Q_{12}) = \text{const.} \quad (4.6)$$

Thus, in principle, if one cuts the sample obliquely with respect to the cubic crystallographic

4.2. Effective electrostrictive coefficients in perovskite thin films

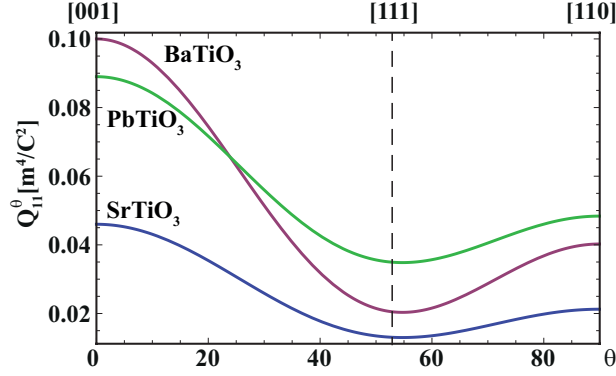


Figure 4.2: Effective Q_{11}^{θ} coefficient as a function of the cut direction θ for three perovskites materials BaTiO₃ (pink), SrTiO₃ (blue) and PbTiO₃ (green). The data for electrostrictive constants are taken from Table 4.1.

directions Q_{12}^{θ} can become positive at the expense of a reduction in Q_{11}^{θ} while keeping the sum $Q_{11}^{\theta} + Q_{12}^{\theta(1)} + Q_{12}^{\theta(2)}$ constant and breaking the classical "extension along the field and contraction perpendicular to it" behaviour. Indeed, for three perovskites materials BaTiO₃, SrTiO₃, and PbTiO₃, such a reduction in Q_{11}^{θ} is possible as clear from Fig. 4.2.

It is seen in Fig. 4.2 that while Q_{11}^{θ} always stays positive, at the same time, it decreases for all the considered perovskite materials. Such a decrease corresponds to appreciable variations in Q_{12}^{θ} for all these materials, as seen from Fig. 4.3, where the dependences of the $\frac{Q_{12}^{\theta}}{Q_{11}^{\theta}}$ ratio on the cut direction θ are plotted. For the cubic ferroelectrics considered, a positive Q_{12}^{θ} can be found for certain directions. Cuts close to the [111]-direction are of special interest. Here one finds expansion of the sample in all directions. In addition, Q_{11}^{θ} has a minimum for the [111]-direction which in turn gives a maximum for $Q_{12}^{\theta(1)} + Q_{12}^{\theta(2)}$. For cuts close to the [110]-direction, instead of the classical "extension along the field and contraction perpendicular to it" behaviour one finds a very different behaviour where, under the field, the sample expands in two dimensions and contracts in one (along the [001]-axis).

4.2 Effective Q_{12} electrostrictive coefficients in thin films

As we saw in the chapter 2 electrostriction plays an essential role in the thermodynamics of thin films. At the same time we learned here that the effective electrostrictive coefficients are different for different crystallographic directions, therefore for the thin films of different orientations (deposited in different orientations) we should expect different behaviour [20, 91]. Indeed, Fig. 4.4 shows the experimental dependance of out-of-plane permittivity on temperature of two constrained BST 30/70 thin films of (111) and (100) orientations respectively. The peaks of permittivity correspond to paraelectric-ferroelectric phase transition in the films. It is interesting to observe that for -0.7% strained (100)-oriented film the T_C is 130 K higher than the transition temperature of unstrained bulk material, but -0.8% strained (111)-oriented film

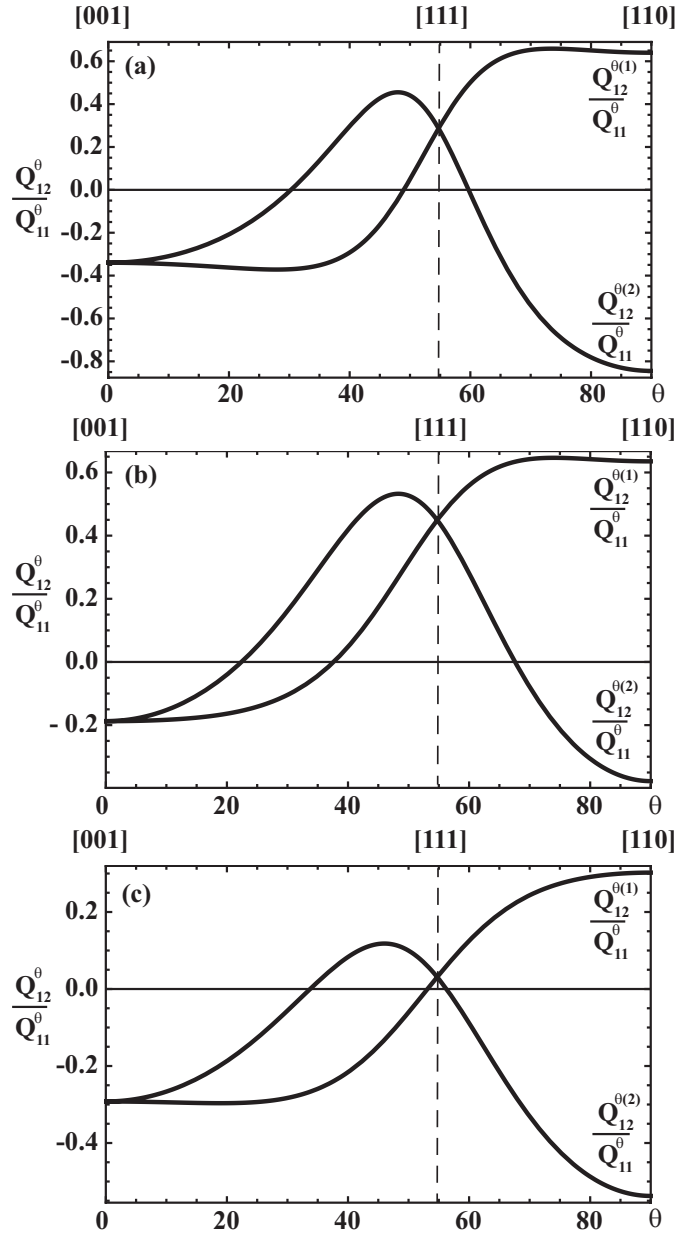


Figure 4.3: Dependence of $\frac{Q_{12}^{\theta}}{Q_{11}^{\theta}}$ ratio on the cut direction θ . Q_{11}^{θ} - longitudinal effective electrostrictive coefficient, $Q_{12}^{\theta(1)}, Q_{12}^{\theta(2)}$ - two transversal effective electrostrictive coefficients (see (4.4)). (a) plotted for BaTiO₃ with coefficients from [5]. (b) for SrTiO₃ from [6]. (c) for PbTiO₃ from [1].

the ferroelectric phase transition occurs at the temperature which is 50 K less than bulk.

To understand this phenomenon one can exploit Landau thermodynamic theory of thin films [1] similarly to what we did in chapter 2 for the (001)-oriented film (eqs. (2.34)-(2.35)). For

4.2. Effective electrostrictive coefficients in perovskite thin films

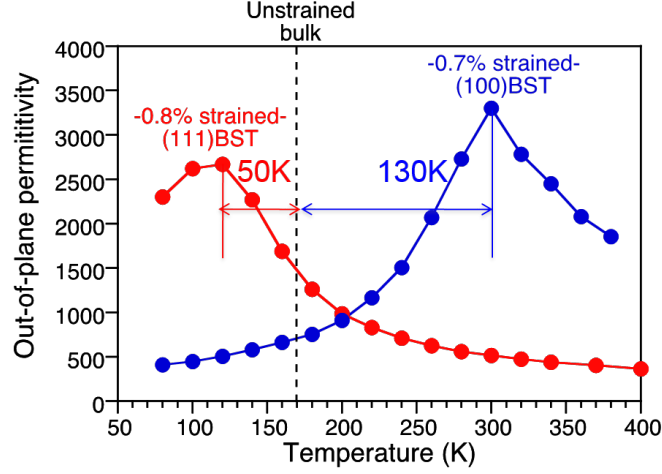


Figure 4.4: Experimental dependence of out-of-plane permittivity on temperature of two BST 30/70 thin films of (111) and (100) orientations. Provided by Yamada Tomoaki, Tokyo Institute of Technology, Japan

(001)-oriented thin film the potential can be written as

$$\tilde{G} = a_1(P_1^2 + P_2^2) + a_3P_3^2 + \dots, \quad (4.7)$$

where the a_1 and a_3 coefficients are [1]:

$$a_1 = a - \frac{Q_{11} + Q_{12}}{s_{11} + s_{12}} \epsilon_0 \quad (4.8)$$

$$a_3 = a - \frac{2Q_{12}}{s_{11} + s_{12}} \epsilon_0 \quad (4.9)$$

with

$$a = \frac{T - T_C}{2\epsilon_0 C_{CW}},$$

where T_C and C_{CW} are the Curie-Weiss temperature and constant of the bulk crystal. In (4.7) we dropped the higher-order polarization terms since we develop qualitative illustration working for relatively small strains and close to the T_C of bulk material. The conditions $a_1 = 0$ and $a_3 = 0$ give two transition lines on the film phase diagram (Fig. 2.3a). Therefore, equations (4.8) and (4.9) show that misfit strain ϵ_0 shifts the T_C . Moreover, this shift of transition temperature also depend on electrostrictive coefficients (see (4.8) and (4.9)). Since, as we saw before, the effective electrostrictive coefficients change for different crystallographic directions one should expect different behaviour for different film orientations. For example, for (111)-

oriented film one can obtain for a_1 and a_3 [20]:

$$\begin{aligned} a_1 &= a - \frac{(4Q_{11} + 8Q_{12} + Q_{44})}{4s_{11} + 8s_{12} + s_{44}} \epsilon_0 \\ a_3 &= a - \frac{(4Q_{11} + 8Q_{12} - 2Q_{44})}{4s_{11} + 8s_{12} + s_{44}} \epsilon_0. \end{aligned} \quad (4.10)$$

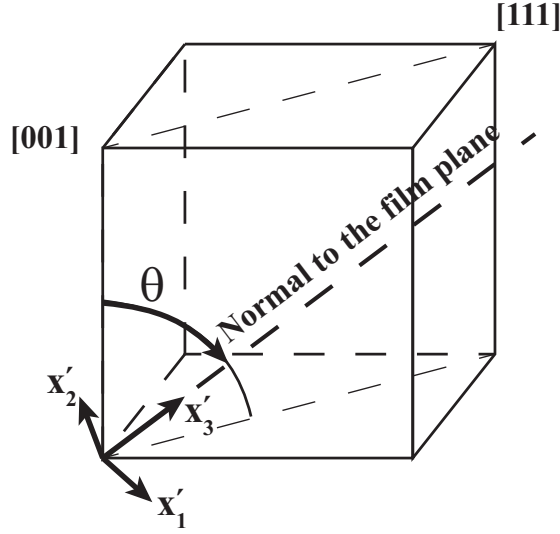


Figure 4.5: Orientation of the film described by the normal to the film plane which differs from [001] crystallographic axis by angle θ . The rotated reference frame (x'_1, x'_2, x'_3) is associated with the film with Ox'_3 axis parallel to the normal.

Let us study a more general case where the film is oriented with angle θ to [001] crystallographic direction (see Fig. 4.5). Using the energy expansion of a centrosymmetric cubic bulk material G (eq. (2.8)), we write the effective thermodynamic potential \tilde{G} of the thin film:

$$\tilde{G} = G + \epsilon'_1 \sigma'_1 + \epsilon'_2 \sigma'_2 + \epsilon'_6 \sigma'_6, \quad (4.11)$$

where ϵ'_i and σ'_i are written for the rotated reference frame, assuming that Ox'_3 axis is perpendicular to the surface of the film. Then, we impose the boundary conditions written for rotated reference frame:

$$\begin{aligned} \epsilon'_1 &= \epsilon_0, \epsilon'_2 = \epsilon_0, \epsilon'_6 = 0 \\ \sigma'_3 &= 0, \sigma'_4 = 0, \sigma'_5 = 0. \end{aligned} \quad (4.12)$$

4.2. Effective electrostrictive coefficients in perovskite thin films

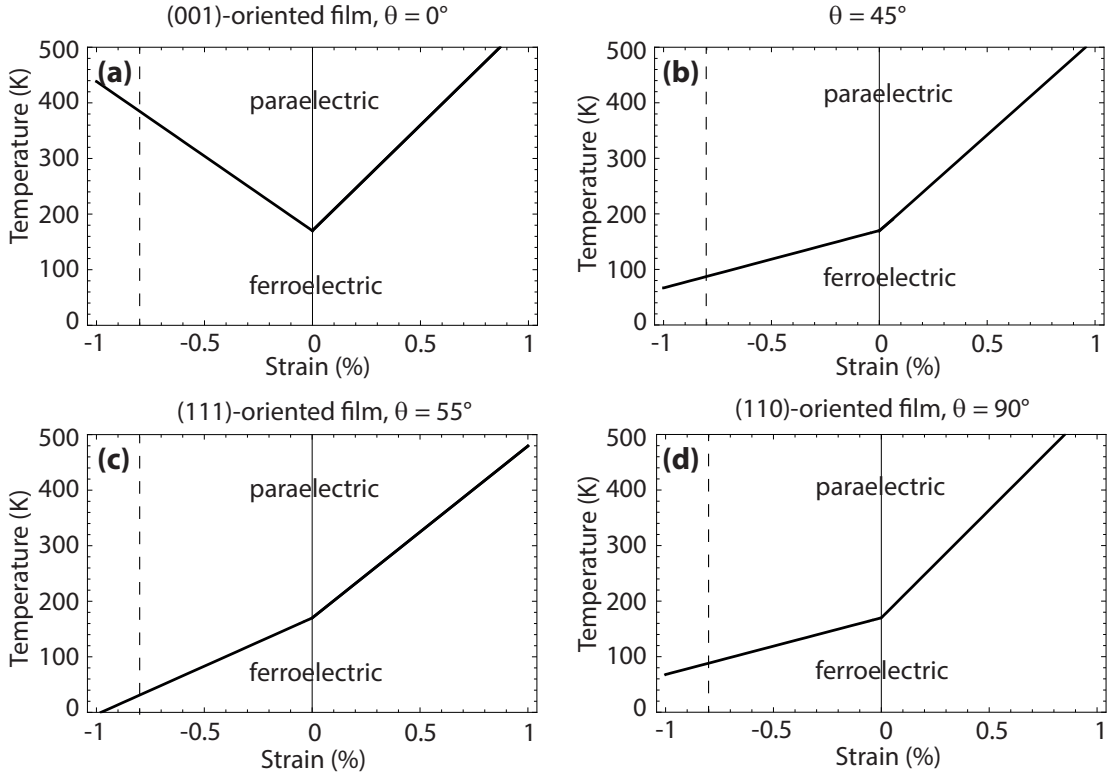


Figure 4.6: Schematically shown thin film temperature - misfit strain phase diagrams for different film orientations of BST 30/70 film. θ - orientation (deposition) angle of the thin film with respect to [001] crystallographic axis. Parameters (T_C , Q_{ij} , s_{ij} , etc.) of bulk BaTiO₃ and SrTiO₃ materials were as taken from [5–7] and interpolated for BST 30/70.

The relationships between stress σ_i of crystallographic reference frame and σ'_i are

$$\begin{aligned}
 \sigma'_1 &= \frac{1}{2}(\sigma_1 + \sigma_2 - 2\sigma_6) \\
 \sigma'_2 &= \frac{1}{2}\left(2\sigma_3 \sin^2(\theta) - \sqrt{2}(\sigma_4 + \sigma_5) \sin(2\theta) + (\sigma_1 + \sigma_2 + 2\sigma_6) \cos^2(\theta)\right) \\
 \sigma'_3 &= \frac{1}{2}(\sigma_1 + \sigma_2 + 2\sigma_6) \sin^2(\theta) + \sigma_3 \cos^2(\theta) + \sqrt{2}(\sigma_4 + \sigma_5) \sin(\theta) \cos(\theta) \\
 \sigma'_4 &= \frac{1}{4}\left((\sigma_1 + \sigma_2 - 2\sigma_3 + 2\sigma_6) \sin(2\theta) + 2\sqrt{2}(\sigma_4 + \sigma_5) \cos(2\theta)\right) \\
 \sigma'_5 &= \frac{1}{2}\left((\sigma_1 - \sigma_2) \sin(\theta) - \sqrt{2}(\sigma_4 - \sigma_5) \cos(\theta)\right) \\
 \sigma'_6 &= \frac{1}{2}\left(\sqrt{2}(\sigma_4 - \sigma_5) \sin(\theta) + (\sigma_1 - \sigma_2) \cos(\theta)\right).
 \end{aligned} \tag{4.13}$$

The relationships (4.13) hold for the components of strain, and they can be obtained by replacing σ by ϵ in (4.13). The resulting thin film potential can be written as

$$\tilde{G} = a_1^* P_1^2 + a_2^* P_2^2 + a_3^* P_3^2, \tag{4.14}$$

where the a_1^* , a_2^* , and a_3^* coefficients are effective dielectric stiffness of the thin film which depend on the orientation of the film (on the angle θ), strain ϵ_0 , and temperature.

Figure 4.6 shows the paraelectric-ferroelectric transition lines of thin film phase diagrams for different film orientations (oriented with angle θ with respect to [001] crystallographic axis) of BST 30/70 film. One can observe that for compressive strains the transition line substantially changes its behaviour, while for tensile strains it nearly does not alter.

Let us consider a thin film under the 0.8% compressive strain (dashed line on the diagrams in Fig. 4.6) corresponding to experimental results shown in Fig. 4.4. The 0.8% compressive strain gives a 180 K (experiment 130 K, Fig. 4.4) increase of transition temperature comparing to the bulk material for (001)-oriented film, while for (111)-orientation we have 120 K (experiment 50 K) negative shift of T_C . Figure 4.7 shows the phase transition temperature depending on the film orientation under the compressive strain of 0.8%, i.e. along the dashed line. One can see that, first, the increase of θ cause the decrease of the phase transition temperature, and T_C has its minimum for (111)-oriented film. It is interesting to notice that for θ around 40 degrees the phase transition temperature of the film becomes equal to that of the bulk material. Figure 4.7 clarifies the experimentally observed behaviour of permittivity on temperature of two BST 30/70 thin films of (111) and (100) orientations showing the positive shift of T_C for (001) film and negative shift for (111)-oriented film with respect to T_C of the bulk material. However, predicted theoretical behaviour gives good qualitative illustration to the effect, but not quantitative agreement: for (001) film predicted shift is 180 K (experiment 130 K), for (111) film 120 K instead of experimental 50 K.

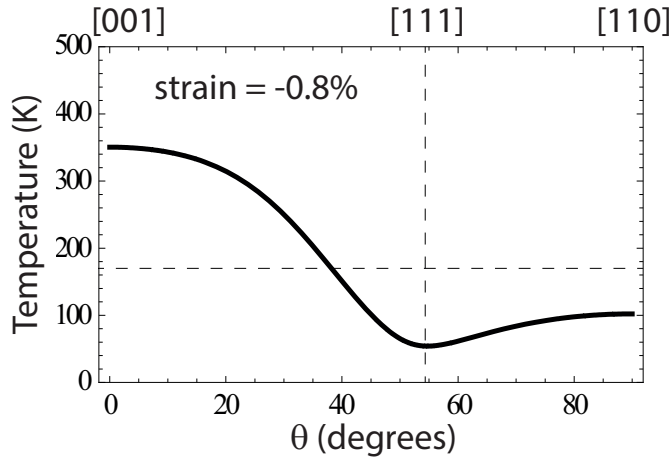


Figure 4.7: Ferroelectric phase transition temperature depending on the film orientation under the compressive strain of 0.8% for BST 30/70 thin film. θ - orientation (deposition) angle of the thin film with respect to [001] crystallographic axis. Parameters (T_C , Q_{ij} , s_{ij} , etc.) of bulk BaTiO₃ and SrTiO₃ materials were as taken from [5–7] and interpolated for BST 30/70.

4.3 Conclusions

In the first part of this chapter it was shown that classical cubic perovskite ferroelectrics exhibit deviations from the "extension along the field and contraction perpendicular to it" behaviour if the sample is cut obliquely to the cubic crystallographic directions. Specifically, a remarkable behaviour is predicted for bars of BaTiO₃, SrTiO₃, and PbTiO₃ cut along the [111] crystallographic cubic direction. In this case, in the paraelectric phase in an electric field parallel to bar, an expansion along all its three dimensions takes place. In terms of the components of the electrostriction tensor, Q_{ij}^θ , in the reference frame of the bar this implies that Q_{11}^θ and Q_{12}^θ are positive in contrast to $Q_{11} > 0$ and $Q_{12} < 0$ in the crystallographic reference frame. The situation with the [110] cut is also unusual, the electrostriction effect in the field directed along the bar will result in a contraction in one transversal direction and an expansion in the another. This implies $Q_{12}^\theta < 0$ and $Q_{13}^\theta > 0$. The crystal chemistry behind such behaviour is not clear for the moment. This phenomenon may be of interest for actuators based on the electrostrictive effect, transducers, and detectors.

In the second part we considered the effect of the change of phase transition temperature of the thin films grown in different crystallographic orientation on the example of BST 30/70. Here, we identify the manifestation of the angular dependance of electrostriction in the phase diagrams of thin films, i.e. we found the shift of T_C depending on the film orientation. It was found that, oppositely to the commonly believed behaviour, a compressive strain does not always increase T_C . Depending on the film orientation the phase transition temperature can be less than that in the bulk material. Ferroelectric properties of materials can be markedly changed through strain engineering. Using of the thin films grown in different orientations gives more flexibility for engineering and provides a broader range of operating temperatures. This can be exploited to modify the ferroelectric properties of any ferroic system, including multiferroics [92], whose ferroic order parameter has a strong coupling to strain.

At the end, we would like to say that, to have a better quantitative theory of differently oriented thin films, one has to consider higher order electromechanical couplings as it was discussed in the chapter 2.

5 Flexoelectric effect

The flexoelectric effect looks promising for practical applications and helps to explain a number of phenomena, especially at the nanoscale. However, the available theoretical and experimental results are rather contradictory, attesting to a limited understanding of flexoelectricity. The bulk flexoelectric effect can be split into static effect (which appears, for example, in a bent plate) and dynamic effect (which can be observed in a sound wave). We demonstrate the possibility of extraction of static and dynamic bulk flexocoupling tensors from phonon dispersion. The developed method can be used with real experimental phonon spectrum to find flexoelectric coefficients. Here, we work with the simulated phonon spectrum of STO, which was calculated using first principles methods.

In this chapter, we first will introduce the bulk flexoelectric effect in crystals. Then, we will demonstrate that the static and dynamic flexoelectric tensors can be found analyzing the phonon dispersion branches with the example of the simulated spectrum of STO cubic crystal. The results extracted from phonon dispersion can be confirmed with an alternative method involving lattice dynamics, i.e. dynamical matrices or Interatomic Force Constants (IFCs), which will be considered further in the corresponding section. The dynamic bulk flexocoupling coefficient was, for the first time, obtained for STO material. We will sum up the results in conclusions.

5.1 Description of the bulk flexoelectric effect in crystals

Following Yudin and Tagantsev [24], we consider a phenomenological approach which provides an adequate description of the bulk flexoelectric effect. However, in contrast to the piezoelectric response, the treatment of the flexoelectric effect in the static (e.g. in a bent plate) and dynamic (in a sound wave) situations generally requires separate treatments [36]. Let us start with the static case.

5.1.1 Static flexoelectric effect

In a simple case one can introduce the flexoelectric effect via the constitutive equation for the electric polarization P_i

$$P_i = \chi_{ij} E_j + e_{ijk} u_{jk} + \mu_{klj} \frac{\partial u_{kl}}{\partial x_j}, \quad (5.1)$$

where E_i , u_{jk} , and $\frac{\partial u_{kl}}{\partial x_j}$ are the macroscopic electric field, the strain tensor, and its spatial gradient, respectively. The first two rhs terms of equation (5.1) describe the dielectric and piezoelectric responses with the tensor of the clamped dielectric susceptibility χ_{ij} and the piezoelectric tensor e_{ijk} , respectively. The last rhs term of equation (5.1) describes the linear polarization response to a strain gradient - flexoelectric effect. The strain tensor is defined as the symmetric part of the tensor $\frac{\partial U_i}{\partial x_j}$, where U_i is the displacement of point of the medium in the direction i :

$$u_{jk} = \frac{1}{2} \left(\frac{\partial U_j}{\partial x_k} + \frac{\partial U_k}{\partial x_j} \right). \quad (5.2)$$

The antisymmetric part of the tensor $\frac{\partial U_i}{\partial x_j}$

$$\Omega_{jk} = \frac{1}{2} \left(\frac{\partial U_j}{\partial x_k} - \frac{\partial U_k}{\partial x_j} \right), \quad (5.3)$$

corresponding to rotations of the sample as a whole. Homogeneous rotations evidently do not contribute to the polarization response. At the same time, the gradients of Ω_{jk} can contribute to the polarization response, however they can always be presented as a sum of the components of tensor $\frac{\partial u_{kl}}{\partial x_j}$, as it was shown by Indenbom et al [46]. The fourth rank tensor μ_{klj} controlling the flexoelectric effect in equation (1) is the flexoelectric tensor, it is symmetric with respect to the permutation of the first two suffixes. The flexoelectric tensor is allowed in materials of any symmetry (including amorphous), in a sharp contrast to the piezoelectric tensor, e_{ijk} , which is a third rank tensor and, therefore, allowed only in non-centrosymmetric materials. This makes the principal difference between piezoelectricity and flexoelectricity, as the latter is a general phenomenon having no symmetry limitations. Since the piezoelectric and flexoelectric tensors describe the properties of a material in the absence of a macroscopical electric field, these can also be defined as

$$e_{ijk} = \left(\frac{\partial P_i}{\partial u_{jk}} \right)_{E=0}, \quad (5.4)$$

$$\mu_{klj} = \left(\frac{\partial P_i}{\partial \left(\frac{\partial u_{kl}}{\partial x_j} \right)} \right)_{E=0}. \quad (5.5)$$

5.1. Description of the bulk flexoelectric effect in crystals

A more advanced description of piezoelectric and flexoelectric effects is based on minimizing of thermodynamic potential [24]. Such a minimization yields the bulk constitutive electromechanical equations:

$$E_i = \chi_{ij}^{-1} P_j - f_{klij} \frac{\partial u_{kl}}{\partial x_j} - g_{ijkl} \frac{\partial^2 P_k}{\partial x_j \partial x_l}, \quad (5.6)$$

$$\sigma_{ij} = c_{ijkl} u_{kl} + f_{ijkl} \frac{\partial P_k}{\partial x_l}, \quad (5.7)$$

where σ_{ij} and c_{ijkl} are stress and elastic stiffness respectively. f_{ijkl} is called flexocoupling tensor. It is seen that, in the case where the strain gradient and the polarization are homogeneous, equation (5.6) reproduces the flexoelectric effect introduced by (5.1) with

$$\mu_{ijkl} = \chi_{kx} f_{ijxl} \quad (5.8)$$

Equation (5.8) links the flexoelectric and flexocoupling tensors, suggesting that the flexoelectric response should be enhanced in materials with high dielectric constants such as ferroelectrics. It is also clear from this equation that via the flexoelectric coupling the strain gradient works as an electric field. Equation (5.7) enables us to recognize the thermodynamically conjugated effect to the static bulk flexoelectric response — converse flexoelectric effect, which consists of the contribution to the mechanical stress, proportional to the gradient of polarization.

5.1.2 Dynamic flexoelectric effect

Now we will discuss the so-called dynamic flexoelectric effect. While the static bulk flexoelectric effect can be viewed as an extension of the piezoelectric effect, the phenomenon treated below has no analogue in piezoelectricity. In the elastic wave in solids, the static effect can be viewed as a contribution to polarization proportional to the strain gradient (which is always present in the mechanical wave). In the time domain, there is another contribution which corresponds to the polarization response to accelerated motion of the medium, or P_i is proportional to \ddot{U}_j , and since in the acoustic wave $\ddot{U}_j \propto \frac{\partial u_{kl}}{\partial x_j}$, this contribution to the flexoelectric effect is called the dynamic flexoelectric effect.

On the phenomenological side, the dynamic flexoelectric effect can be taken into account by adding a mixed term to the density of kinetic energy

$$T_k = \frac{\rho}{2} \dot{U}_i^2 + \frac{\gamma_{ij}}{2} \dot{P}_i \dot{P}_j + M_{ij} \dot{U}_i \dot{P}_j \quad (5.9)$$

where ρ is the density and γ_{ij} is a phenomenological tensor controlling the dynamics of

polarization, M_{ij} is a dynamic flexoelectric tensor. Minimizing the action

$$\int \int (T - \Phi + u_i \sigma_i) dV dt, \quad (5.10)$$

$$\Phi = \frac{\chi_{ij}^{-1}}{2} P_j P_j + \frac{c_{ijkl}}{2} u_{ij} u_{kl} + \frac{g_{ijkl}}{2} \frac{\partial P_i}{\partial x_j} \frac{\partial P_k}{\partial x_l} - \frac{f_{ijkl}}{2} \left(P_k \frac{\partial u_{ij}}{\partial x_l} - u_{ij} \frac{\partial P_k}{\partial x_l} \right) - P_i E_i, \quad (5.11)$$

with respect to P_i and U_j [24] one obtains

$$E_i = \chi_{ij}^{-1} P_j - f_{klij} \frac{\partial u_{kl}}{\partial x_j} + M_{ij} \ddot{U}_j - g_{ijkl} \frac{\partial^2 P_k}{\partial x_j \partial x_l} + \gamma_{ij} \ddot{P}_j, \quad (5.12)$$

$$\rho \ddot{U}_i = c_{ijkl} \frac{\partial u_{kl}}{\partial x_j} + f_{ijkl} \frac{\partial^2 P_k}{\partial x_l \partial x_l} - M_{ji} \ddot{P}_j. \quad (5.13)$$

The last two rhs terms of equation (5.12) control the spatial and frequency dispersion of the polarization response. However, when we consider macroscopic manifestations of the flexoelectric response (e.g. in a dynamically bent sample or in ultrasonic acoustic wave), where $1/q$ (q - phonon wave vector) is much larger than the typical microscopic scales, and sound wave frequency is much smaller than the typical optical phonon frequencies, these terms can be neglected. Thus, setting electric field to 0 in (5.12) and taking into account that $\ddot{U}_j \propto \frac{\partial u_{kl}}{\partial x_j}$ we see that the $M_{ij} \ddot{U}_j$ term corresponding to the dynamic flexoelectric effect indeed provides a contribution to polarization along with f_{ijkl} .

It is instructive to eliminate \ddot{U}_i between equations (5.12) and (5.13) to find a relationship controlling the total flexoelectric response in the dynamic case omitting the terms containing the higher order second derivatives of polarization $\frac{\partial^2 P_k}{\partial x_j \partial x_l}$ and \ddot{P}_i :

$$E_i = \chi_{ij}^{-1} P_j - \left(f_{klij} - \frac{1}{\rho} M_{ix} c_{xjkl} \right) \frac{\partial u_{kl}}{\partial x_j}. \quad (5.14)$$

From this equation we can see that in view of the dynamic flexoelectric effect, the role of the flexocoupling tensor, f_{klij} , is now played by the total flexocoupling tensor:

$$f_{klij}^{\text{tot}} = f_{klij} - \frac{1}{\rho} M_{ix} c_{xjkl} = f_{klij} + f_{klij}^{\text{dyn}}. \quad (5.15)$$

Thus, including the dynamic case, the flexoelectric response is controlled by the total flexoelectric tensor

$$\mu_{ijkl}^{\text{tot}} = \mu_{ijkl} + \mu_{ijkl}^{\text{dyn}}, \quad (5.16)$$

5.2. Determination of flexoelectric tensors using phonon dispersion

where the dynamic contribution is correspondingly defined as

$$\mu_{klij}^{\text{dyn}} = -\frac{1}{\rho} \chi_{ix} M_{xy} c_{yjkl}. \quad (5.17)$$

Both the phenomenological and microscopic theories suggest that, like the static contribution, the dynamic contribution should be enhanced in high-K materials, see Eq. (5.17). The dynamic contribution to the flexoelectric effect makes it qualitatively different from the piezoelectric effect.

Order-of-magnitude estimates [24] show that the components of tensors f_{ijkl} and f_{ijkl}^{dyn} are expected to be comparable. One should mention that, despite the fact that the components of the tensors f_{ijkl} and f_{ijkl}^{dyn} are expected to be comparable, the dynamic flexoelectric effect does not always provide a contribution comparable to that of the static effect. In an acoustic wave, the dynamic effect works at full strength, however, in quasi-static experiments of plate bending, i.e. where the smallest dimension of the sample is less than the acoustic wavelength corresponding to the frequency of the external perturbation, the dynamic effect is negligible [24].

In the following sections, we will first demonstrate a possibility of determination of static and dynamic bulk flexocoupling tensors using phonon spectrum. We will calculate them using a model spectrum for STO material which was obtained with first principles calculations. Then, we will use an alternative approach to calculate flexocoupling tensors which involves microscopic lattice dynamics, i.e. Interatomic Force Constants (IFC). At the end, we will conclude, comparing the results obtained with two methods and showing advantages and drawbacks of both approaches.

5.2 Determination of flexoelectric tensors using phonon dispersion

5.2.1 Introduction

One of the direct manifestations of flexoelectric coupling is related to phonon spectra in solids. In terms of phonons, the flexoelectric interaction can be interpreted as a repulsion between transverse acoustic (TA) and soft-mode transverse optic (TO) branches. This effect was documented in perovskite ferroelectrics by Axe et al, who studied the dispersion of the phonons in KTaO_3 (KTO) [8] and PbTiO_3 [93] by means of neutron scattering. The temperature dependence of the dispersion curves obtained for KTO is shown in figure 5.1. As it is seen from the figure, with decreasing temperature the soft optical branch moves downward closer to the acoustic one and causes a bending of the latter. The temperature-driven acoustic phonon branch bending has also been observed in STO by Hehlen et al [94] by means of Brillouin scattering (the method which allows to trace acoustic branches in the vicinity of the Γ -point).

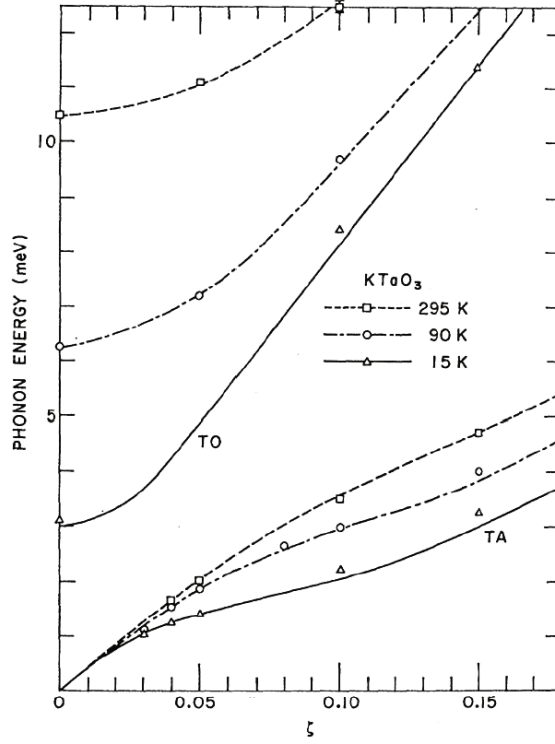


Figure 5.1: Temperature dependence of dispersion curves for transverse acoustic (TA) and soft-mode optic (TO) phonons with wavevector $q = \frac{\pi}{a}(\xi, 0, 0)$ in KTaO_3 , where a is the lattice constant. Taken from ref. [8].

It is possible to describe the repulsion of phonon branches in terms of the continuum Landau theory [24]. Within the validity of the continuum model we consider the long-wavelength part of the spectrum. We start with equations (5.12) and (5.13), where we rewrite the strain in terms of acoustic displacement

$$u_{kl} = \frac{1}{2} \left(\frac{\partial U_k}{\partial x_l} + \frac{\partial U_l}{\partial x_k} \right). \quad (5.18)$$

To describe the phonons, we search for solutions for polarization and displacement in the form

$$P = \tilde{P} e^{i\omega t - i\vec{q}\vec{x}}, \quad (5.19)$$

$$U = \tilde{U} e^{i\omega t - i\vec{q}\vec{x}}. \quad (5.20)$$

Since we are interested in the transverse modes, in which electric field does not arise, we omit the term related to electric field and obtain the following set of linear homogeneous equations

5.2. Determination of flexoelectric tensors using phonon dispersion

for amplitudes of polarization and displacement:

$$\omega^2 \gamma_{ij} \tilde{P}_j = \chi_{ij}^{-1} P_j + g_{ijkl} q_j q_l \tilde{P}_k + f_{kl ij} q_j q_l \tilde{U}_k - M_{ij} \tilde{U}_j \omega^2, \quad (5.21)$$

$$\rho \omega^2 \tilde{U}_i = c_{ijkl} q_j q_l \tilde{U}_k + f_{ijkl} q_j q_l \tilde{P}_k - M_{ji} \tilde{P}_j \omega^2. \quad (5.22)$$

Eigenfrequencies of the system, corresponding to acoustic and optic branches, may be found from the condition of zero determinant of the set of equations (5.21) and (5.22). Let us illustrate the acoustic branch bending for the case of the cubic crystalline lattice symmetry and the q -vector directed along a four-fold axis, which corresponds to the conditions of the experiment by Axe et al (figure 5.1). In this case, the transverse modes are two-fold degenerate and not coupled with the longitudinal mode. The dispersion of the transverse modes may be readily derived from equations (5.21) and (5.22) by applying the zero determinant condition to get:

$$(\omega^2 - \omega_A^2)(\omega^2 - \omega_O^2) = \frac{(\omega^2 M - q^2 f_{44})^2}{\rho \gamma}, \quad (5.23)$$

where ω_A and ω_O are the TA and TO phonon frequencies in the absence of flexoelectric coupling:

$$\omega_A^2 = \frac{c_{44} q^2}{\rho}, \quad (5.24)$$

$$\omega_O^2 = \frac{\alpha + g_{44} q^2}{\gamma}. \quad (5.25)$$

In view of the cubic symmetry of the material under consideration second order tensors become scalars, so we use the expressions $M_{ij} \rightarrow M$, $\gamma_{ij} \rightarrow \gamma$, $\chi_{ij}^{-1} \rightarrow \alpha$.

The trend of the phonon branch repulsion can be identified by treating the case of weak interaction between the branches. In this case the relative shift of the acoustic branch may be calculated from equation (5.23) by setting $\omega = \omega_A$ everywhere except for the first parenthesis in the lhs to get:

$$\omega^2 = \omega_A^2 - \frac{q^4 (f_{44}^{\text{tot}})^2}{\gamma \rho (\omega_O^2 - \omega_A^2)}, \quad (5.26)$$

where

$$f_{100}^{\text{tot}} = f_{44}^{\text{tot}} = f_{44} - \frac{c_{44}}{\rho} M. \quad (5.27)$$

The repulsive character of the interaction between the branches (or lowering of the acoustic branch) is seen from the sign in expression (5.26). As for its magnitude, it is controlled by the

total flexocoupling coefficient, (5.27), which has both dynamic and static contributions. We should take into account this fact when we will extracting information about the flexocoupling tensors from ab initio phonon dispersion curves. Formula (5.26) works best in the vicinity of the Γ -point, where the mode coupling conditioned by higher powers of the wavevector and self dispersion of the branches are weak. The difference of frequency squares in the denominator in the rhs of equation (5.26) indicates the amplification of the effect when the optical branch approaches the acoustic one (e.g. with decreasing temperature). The trend of the branch repulsion described above holds when interaction between them is strong. In the case of strong coupling, the contributions of static and dynamic flexoelectric effects to the acoustic branch bending become frequency-weighted, as controlled by expression (5.23). As noticed by Axe et al [8], if the strength of flexoelectric effect exceeds some threshold (once the acoustic branch touches the x-axis in figure 5.1), there will be a phase transition into an incommensurate phase.

5.2.2 Ab initio calculations of phonon dispersion curves

To obtain phonon dispersion curves and IFCs, we exploit the QE ab initio package. Phonon calculations with QE represent a two-step process. First, one has to find the groundstate atomic and electronic configuration using PWscf. The PWscf calculations were also made within the GGA PBE exchange-correlation functional with ultrasoft pseudopotential by Vanderbilt [80]. We have used an automatically generated uniform $10 \times 10 \times 10$ grid of k-points, the kinetic energy cutoff for wavefunctions was 60Ry (816eV). Second, one calculates phonons using Density Functional Perturbation Theory as implemented in the PHonon code. For phonon calculations use used $10 \times 10 \times 10$ automatic Monkhorst-Pack grid of q-points. The energy threshold for self-consistency was chosen to be equal to 10^{-16} Ry (1.4×10^{-15} eV) with the help of the convergence tests. Within PHonon, first, ph.x code calculates normal modes and dynamical matrices at given mesh of q-points. At this step dynamical matrices does not contain the nonanalytic term occurring in polar materials, i.e. there is no LO-TO splitting, moreover no Acoustic Sum Rule (ASR) is applied. Then, code q2r.x (q-point to real space) reads the dynamical matrices produced in the preceding step and Fourier-transform them, writing a file of IFC in real space, up to a distance that depends on the size of the grid of q-vectors. At the end, matdyn.x program is used to produce phonon modes, frequencies, and dynamical matrices at any q-point using the IFC as input. At this step ASR is applied and microscopic field contribution (LO-TO splitting) can be introduced. This procedure of a double Fourier transformations offers a scheme which gives a good accuracy of the frequencies for all q-points being much cheaper computationally.

A real STO material has a structural transition at 105 K, which occurs due to the oxygen octahedra rotation, changing the symmetry from cubic to tetragonal. These tetragonal distortions are found to be essential in preventing the ferroelectric transition. If one suppressed this structural instability (for instance, keeping the cubic symmetry of the material) STO would have a ferroelectric phase transition near 30 K [95]. A manifestation of this behaviour is supported

5.2. Determination of flexoelectric tensors using phonon dispersion

by DFT calculations with GGA exchange-correlation functionals of cubic STO where one can observe negative squares of phonon frequencies for the soft-mode phonons for relaxed cubic structure. To avoid this situation, of course, it is possible to include the oxygen octahedra rotation and work with tetragonal STO, which is the stable configuration at 0 K, but in this case phonon picture is much more complicated, and therefore it is much more computationally expensive. The stability of cubic STO can also be brought by applying a hydrostatic pressure to the system. Here we would like to remark that we are primarily interested in high order inharmonic couplings (flexoelectric couplings) which change very little with pressure or temperature, unlike, for example, the dielectric response. The possible change of flexoelectric coefficients is defined by the deformation of the system, which is about 1% for our case. This way, we believe that the obtained here estimates are valid for realistic finite temperature and pressure.

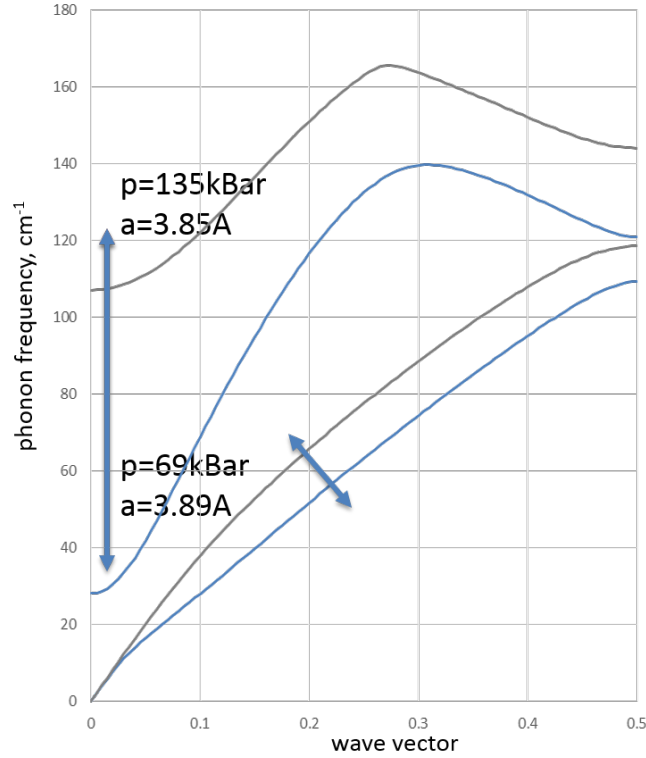


Figure 5.2: Calculated phonon dispersion of transverse acoustic (TA) and soft-mode transverse optic (TO) branches with wavevector $q = \frac{\pi}{a}(\xi, 0, 0)$ for cubic SrTiO_3 stabilized by pressure. The blue lines correspond to the lower pressure ($p = 69$ kBar, $a = 3.89$ Å) when the flexoelectric interaction between the TO and TA branches is strong and one can observe lowering of the TA. The grey lines correspond to the high pressure ($p = 135$ kBar, $a = 3.85$ Å) when the interaction is weak.

Figure 5.2 shows phonon dispersion of the TA and TO branches for [1,0,0] direction for the cubic STO stabilized by pressure. Tuning the pressure one can bring the TO and TA branches closer to each other amplifying the flexoelectric coupling. The blue lines correspond to the

lower pressure ($p = 69$ kBar, $a = 3.89$ Å) when the flexoelectric interaction between the TO and TA phonon is strong and one can observe lowering of the TA branch. The grey lines correspond to the high pressure ($p = 135$ kBar, $a = 3.85$ Å) when the TO and TA branches stand far from each other and therefore the interaction is weak. This picture of the TA branch lowering with pressure is similar to that with temperature observed by Axe for KTO, see Fig. 5.1.

Since the flexoelectric effect is proportional to the dielectric constant it is essential to know its value for the studied system. The dielectric constant can be found from the frequency of the TO mode at Γ -point, namely [96]

$$\omega_O^2(0) = \frac{\lambda}{\epsilon}. \quad (5.28)$$

For the low pressure ($\omega_O(0) = 28\text{cm}^{-1}$) with $\sqrt{\lambda} = 4.7 \times 10^{13}$ Hz [96] we have relative dielectric constant $\epsilon_r = 3138$, whereas for high pressure ($\omega_O(0) = 107\text{cm}^{-1}$) ϵ_r equals 215. This way we have the ab initio STO cubic structure approaching the phase transition not with temperature but with pressure.

5.2.3 Results

To observe the flexoelectric coupling, it is instructive to plot the dispersion curves for the square of the phonon frequency vs that of the wave vector, Fig. 5.3. The grey and blue curves of the TA phonon correspond to high and low pressure. The dashed lines show the linear behaviour in the absence of interaction between branches corresponding to the expressions (5.24) and (5.25). For the high pressure case, the flexoelectric coupling is weak in view of the large distance between the TA and TO branches. We assume that in this case the bending of the acoustical branch is conditioned by the self dispersion of the curves or other higher order effects, which are not related to flexoelectric coupling under study.

Fitting the TA branch of $[1,0,0]$ direction of wavevector to (5.26) in the vicinity of Γ -point one can find f_{44}^{tot} within the sign ambiguity. Expression (5.26) gives only total value of flexoelectric coefficient, to find f_{44} and M , one has to consider full expression (5.23). Substituting ω in rhs of (5.23) with expression (5.26) one can obtain:

$$(\omega^2 - \omega_A^2)(\omega^2 - \omega_O^2) = \frac{\left(q^2 f_{44}^{\text{tot}} + q^4 M \frac{(f_{44}^{\text{tot}})^2}{\alpha \rho}\right)^2}{\rho \gamma}. \quad (5.29)$$

or

$$\pm \sqrt{\frac{\rho \gamma (\omega^2 - \omega_A^2)(\omega^2 - \omega_O^2)}{q^2}} = f_{44}^{\text{tot}} + q^2 M \frac{(f_{44}^{\text{tot}})^2}{\alpha \rho}. \quad (5.30)$$

We used formula (5.30) with ω corresponding to the fitted TA branch to find f_{44} and M . The lhs of (5.30) is shown in figure 5.4. From Eq. (5.30) and Fig. 5.4 one can see the coefficients

5.2. Determination of flexoelectric tensors using phonon dispersion

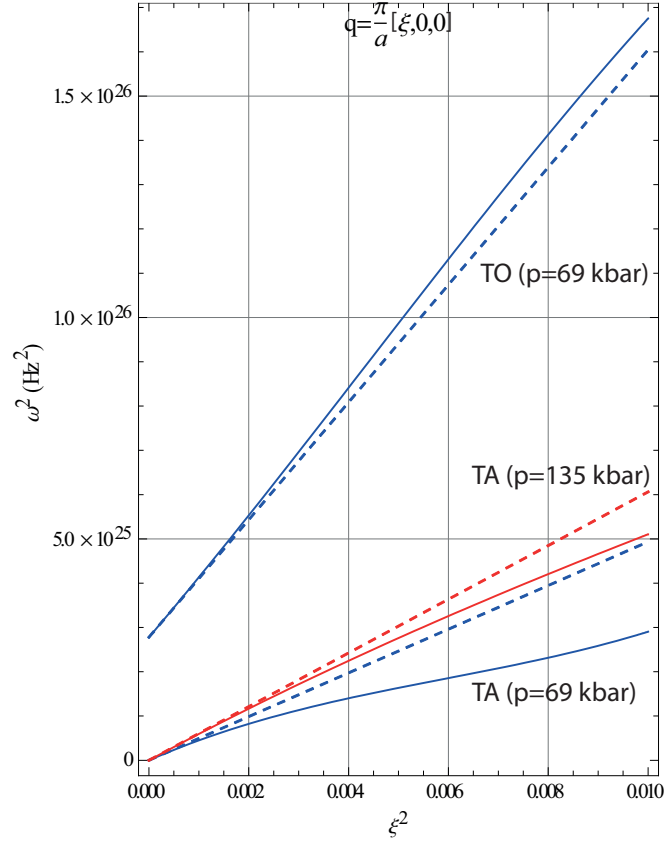


Figure 5.3: Calculated dependence of square of phonon frequency on square of wave vector of transverse acoustic (TA) and soft-mode transverse optic (TO) branches with wavevector $q = \frac{\pi}{a}(\xi, 0, 0)$ for cubic SrTiO₃ stabilized by pressure. Blue and red lines correspond to the hydrostatic pressure 69 kBar and 135 kBar correspondingly. The red TO branch (high pressure) is out of the figure.

can be found within the sign ambiguity, however we know the relative sign.

It is possible to find other components of the static flexoelectric tensor analyzing the phonon dispersion curves in other directions of the wavevector. Let us consider phonon dispersion with the q -vector directed along the [110] direction. From equations (5.18) and (5.19) by applying the zero determinant condition we get two different transverse modes: one with displacement and polarisation vectors parallel to [001] direction is described by expression (5.23) already considered above and the other with displacement and polarisation vectors parallel to $[1\bar{1}0]$ expressed by

$$(\omega^2 - \omega_A^2)(\omega^2 - \omega_O^2) = \frac{(\omega^2 M - q^2 f^{\text{eff}})^2}{\rho\gamma}, \quad (5.31)$$

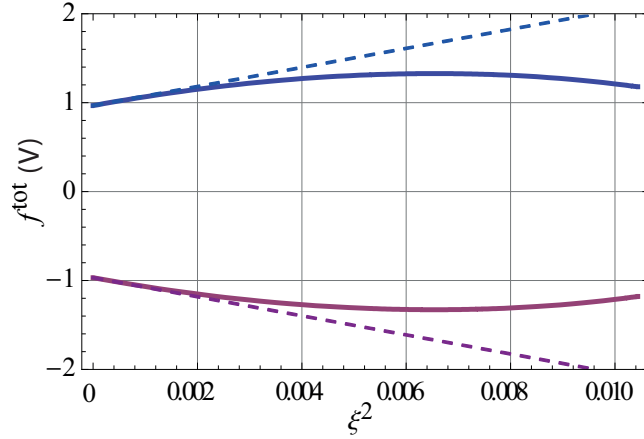


Figure 5.4: The lhs of the expression (5.30) with the ω corresponding to the TA branch with wavevector $q = \frac{\pi}{a}(\xi, 0, 0)$ for cubic SrTiO₃ stabilized by 69 kBar hydrostatic pressure. Blue and purple curves correspond to the "+" and "-" signs in (5.30), correspondingly. The dashed lines are tangent lines, which were used to find M coefficient.

with new ω_A and ω_O :

$$\omega_A^2 = \frac{c^{\text{eff}} q^2}{\rho}, \quad (5.32)$$

$$\omega_O^2 = \frac{\alpha + g^{\text{eff}} q^2}{\gamma}, \quad (5.33)$$

where

$$\begin{aligned} c^{\text{eff}} &= \frac{1}{2}(c_{11} - c_{12}) \\ g^{\text{eff}} &= \frac{1}{2}(g_{11} - g_{12}) \\ f^{\text{eff}} &= \frac{1}{2}(f_{11} - f_{12}) \end{aligned} \quad (5.34)$$

Figure 5.5 shows the calculated phonon dispersion curves for direction of the wavevector $q = \frac{\pi}{a}(\xi, \xi, 0)$. The two modes, with displacement and polarisation vectors parallel to [001] direction (TA1 and TO1) and with displacement and polarisation vectors parallel to [1 $\bar{1}$ 0] (TA2 and TO2), are shown with orange and green colours correspondingly. Analysing the orange curves (TA1 and TO1) and using formula (5.23) we can double check the value of already obtained coefficients f_{44} and M . Using expression (5.31) and the fit of the green dispersion curves (TA2 and TO2) we can find $f^{\text{eff}} = \frac{1}{2}(f_{11} - f_{12})$ and M . However, one can see that the TA2 branch little deviates from the straight dashed line indicating a very small interaction between

5.2. Determination of flexoelectric tensors using phonon dispersion

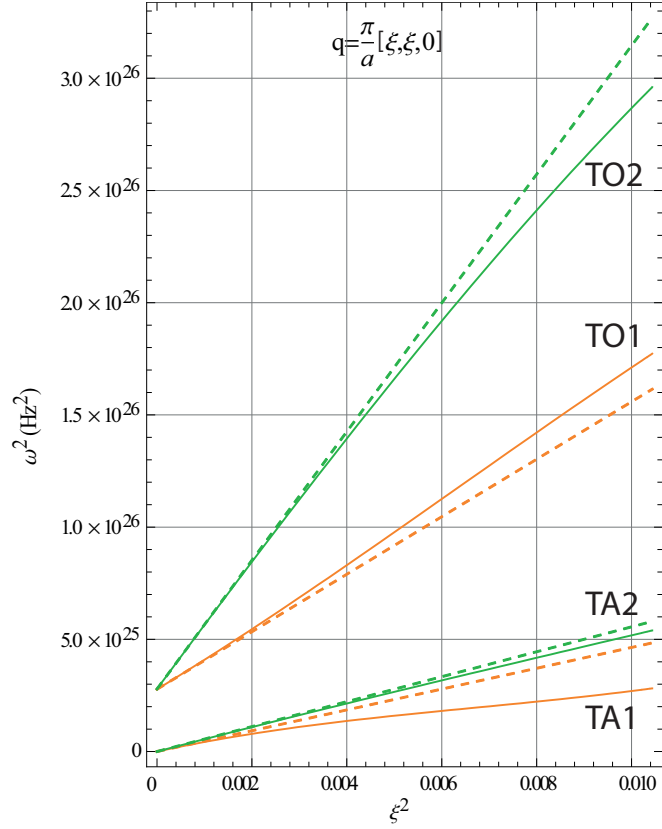


Figure 5.5: Calculated dependence of square of phonon frequency on square of wave vector of transverse acoustic (TA) and soft-mode transverse optic (TO) branches for cubic SrTiO₃ for direction [110], $q = \frac{\pi}{a}(\xi, \xi, 0)$. The two modes, with displacement and polarisation vectors parallel to [001] direction (TA1 and TO1) and with displacement and polarisation vectors parallel to [1 $\bar{1}$ 0] (TA2 and TO2), are shown with orange and green colours correspondingly.

branches, i.e.

$$f_{11} - f_{12} \approx \frac{c_{11} - c_{12}}{\rho} M. \quad (5.35)$$

It can be shown that the analysis of dispersion curves of other directions of wavevector will not resolve other components of flexoelectric tensor, i.e. we will always have combination of $f_{11} - f_{12}$ and f_{44} . For instance, for [111] direction of q-vector we can write the same expression (5.31) with

$$\begin{aligned} c^{\text{eff}} &= \frac{1}{3}(c_{11} - c_{12} + c_{44}) \\ g^{\text{eff}} &= \frac{1}{3}(g_{11} - g_{12} + g_{44}) \\ f^{\text{eff}} &= \frac{1}{3}(f_{11} - f_{12} + f_{44}) \end{aligned} \quad (5.36)$$

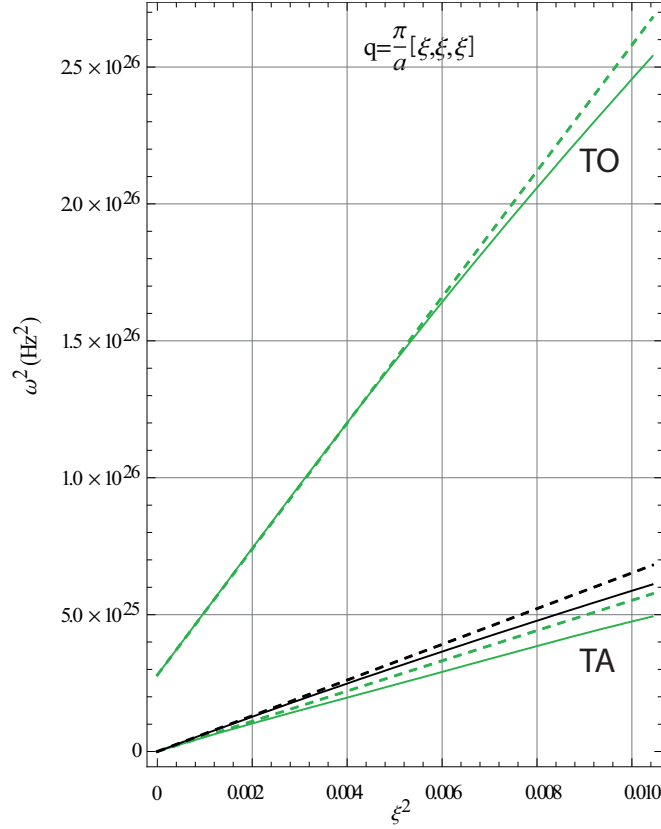


Figure 5.6: Calculated dependence of square of phonon frequency on square of wave vector of transverse acoustic (TA) and soft-mode transverse optic (TO) branches for cubic SrTiO₃ for direction [111], $q = \frac{\pi}{a}(\xi, \xi, \xi)$. Green lines correspond to the low pressure ($p = 69$ kBar), black lines - high pressure ($p = 135$ kBar).

which can be used only to confirm previously obtained values. Figure 5.6 shows the dependence of square of phonon frequency on square of wave vector of the TA and TO branches for [111] direction of q -vector. One can see that the flexoelectric coupling is again small, which means

$$f_{11} - f_{12} + f_{44} \approx \frac{c_{11} - c_{12} + c_{44}}{\rho} M. \quad (5.37)$$

Referring to the flexoelectric coupling as small we actually mean that bending of the TA branch because of the flexoelectric coupling is of the same magnitude as the self dispersion of the branch related to other effects. It can be seen in Fig. 5.6 where lowering of the TA dispersion curves at low (green line) and high (black line) pressure (no flexoelectric coupling) is practically the same, which is contrary to the situation shown in Fig. 5.3.

The results of analysis of dispersion curves in different directions of q -vector can be summa-

5.3. Determination of flexoelectric tensors using lattice dynamics

rized as

$$\begin{aligned}
 [100] \text{ direction of } \mathbf{q} \text{ vector: } f_{100}^{\text{tot}} = f_{44}^{\text{tot}} &= f_{44} - \frac{c_{44}}{\rho} M, \\
 [110] \text{ direction of } \mathbf{q} \text{ vector: } f_{110}^{\text{tot}} = f^{\text{tot}} &= \frac{f_{11} - f_{12}}{2} - \frac{c_{11} - c_{12}}{2\rho} M, \\
 [111] \text{ direction of } \mathbf{q} \text{ vector: } f_{111}^{\text{tot}} = f^{\text{tot}} &= \frac{f_{11} - f_{12} + f_{44}}{3} - \frac{c_{11} - c_{12} + c_{44}}{3\rho} M.
 \end{aligned} \tag{5.38}$$

If only information on f^{tot} is available, for example, due to the precision of phonon dispersion curves, one can use three Eqs. (5.38) to find three unknown values f_{44} , $f_{11} - f_{12}$, and M . We also used these equations to check the agreement of the obtained values.

	[100]	[110] (TA1)	[110] (TA2)	[111]
$c^{\text{eff}} (\times 10^{11} \frac{\text{N}}{\text{m}^2})$	$c_{44} = 0.98$	$c_{44} = 0.96$	$\frac{1}{2}(c_{11} - c_{12}) = 1.12$	$\frac{1}{3}(c_{11} - c_{12} + c_{44}) = 1.09$
$f^{\text{tot}} (\text{V})$	± 1.0	± 1.0	< 0.3	< 0.3
$M, \times 10^{-8} \frac{\text{Vs}^2}{\text{m}^2}$	± 6.3	± 7.0	± 7.4	undefined
$\frac{c^{\text{eff}}}{\rho} M (\text{V})$	± 1.2	± 1.3	± 1.5	undefined
$f_{44} (\text{V})$	± 2.2	± 2.2		
$f_{11} - f_{12} (\text{V})$			$\pm 2.4 \pm 0.3$	$\pm 2 \pm 0.3$

Table 5.1: Material parameters obtained from analysis of phonon dispersions of cubic STO ($a = 3.89 \text{ \AA}$) under pressure 69 kBar. c^{eff} is effective value of mechanical stiffness obtained from the tangent of the TA branch at Γ -point. f and M are static and dynamic flexocoupling coefficients. ρ is the density of STO, $\rho = 5174 \frac{\text{kg}}{\text{m}^3}$, calculated by the mass of atoms in the unit cell divided by the volume.

The values of the static and dynamic bulk flexoelectric tensor for STO which were extracted from the phonon dispersion curves, are given in Table 5.1. The f^{tot} coefficients are found within the sign ambiguity due to the quadric character of flexoelectric coupling in (5.23) and (5.31). As it was expected, the dynamic flexoelectric coefficient, $\frac{c_{44}}{\rho} M = \pm 1.2 \text{ V}$ ($M = \pm 6.3 \times 10^{-8} \frac{\text{Vs}^2}{\text{m}^2}$), is comparable with total flexoelectric coefficient. This way one can see a 100% difference between static and total flexoelectric coefficients which confirms the fact of the necessity of including the dynamic contribution.

The discussed above procedure can be readily used with the real phonon spectrum based on experimental data.

5.3 Determination of flexoelectric tensors using lattice dynamics

The discussed above method based on the processing of dispersion curves is suitable to obtain flexoelectric coefficients, however within this method two things are missing. First, the coefficients can be only defined within the sign ambiguity and, second, the method cannot resolve the difference $f_{11} - f_{12}$.

Actually, it is possible to find static and dynamic and flexocoupling tensors using microscopic theories. For the static flexoelectric tensor, it was done by Maranganti and Sharma [35] for some semiconductor and ferroelectric materials including STO. Here, we are mainly interested in M coefficient and suitability of standard DFT calculation schemes for static flexocoupling tensor.

5.3.1 Introduction

The microscopic theory of the bulk flexoelectric effect has been developed by Tagantsev [36]. Here, we will consider a point-charge approximation, but instead of treating the ions as point charges, we will use more exact Born charges. This is a good approximation for calculating the flexoelectric response for materials with high dielectric constant, e.g. ferroelectrics, where the lattice contribution is dominant. We used the so-called long-wavelength method, originally introduced into the lattice dynamics theory by Born and Huang [97]. In this method, one considers a sinusoidal wave of elastic deformation with a wavelength which is much larger than the typical interatomic distance and calculates the amplitude of the induced polarization wave, based on lattice mechanics of crystals and the basic definition of polarization. Then, the microscopic expressions for the flexoelectric tensor can be found by comparing the results of these calculations with the amplitude of the induced polarization wave calculated within the basic constitutive equation (5.1).

While the complete description of the method can be found in refs. [24, 36] here we show the expressions which link the phenomenological values of flexocoupling tensors with microscopic bulk properties.

For f^* defined by the equation of motion

$$E_i = \chi_{ij}^{-1} P_j + f_{ijkl}^* \frac{\partial^2 U_j}{\partial r_k \partial r_l} + M_{ij} \ddot{U}_j \quad (5.39)$$

the static bulk flexoelectric tensor can be found as

$$\chi_{ij} f_{ijkl}^* = -\frac{1}{v} Q_{i,j,p} N_{j,p}^{klm}, \quad (5.40)$$

where v is the volume of the unit cell, $Q_{i,j,p}$ are the Born charges. We would like to draw attention that the flexocoupling tensors f and f^* are actually defined differently (compare (5.39) and (5.6)). Using the relation

$$\frac{\partial^2 U_j}{\partial x_k \partial x_l} = \frac{\partial u_{jl}}{\partial x_k} + \frac{\partial u_{jk}}{\partial x_l} + \frac{\partial u_{kl}}{\partial x_j} \quad (5.41)$$

it can be shown that

$$f_{ijkl} = -\left(f_{kilj}^* + f_{kijl}^* + f_{klji}^*\right). \quad (5.42)$$

5.3. Determination of flexoelectric tensors using lattice dynamics

The dynamic flexocoupling tensor can be found from the relationship:

$$\chi_{ij} M_{jk} = -\frac{1}{\nu} Q_{i,j,p} G_{j,p}^k \quad (5.43)$$

One can also obtain the expression for dielectric susceptibility

$$\chi_{ij} = \frac{1}{\nu} Q_{i,k,p} \Gamma_{kp,lp'} Q_{j,l,p'} \quad (5.44)$$

which is instructive for us while comparing the results obtained from phonon dispersion and microscopic lattice dynamic. The tensors Γ , N , and G can be calculated in terms of lattice dynamics theory [36, 97]. Following Tagantsev [36], we write microscopic expressions for N and G :

$$N_{i,p}^{jkl} = \sum_{p''} \Gamma_{ip,i'p'} \tilde{T}_{i'p',jp''}^{kl} \quad (5.45)$$

with

$$\tilde{T}_{ip,i'p'}^{jl} = T_{ip,i'p'}^{jl} - \frac{\delta_{pp'}}{s} \sum_{p''p'''} T_{ip'',i'p'''}^{jl} \quad (5.46)$$

and

$$G_{i,p}^j = -\Gamma_{ip,i'p'} \mu_{p'}, \quad \mu_p = m_p - \frac{1}{s} \sum_i m_i \quad (5.47)$$

where Γ is the inverse matrix, defined in a special way [96], to the singular matrix $A_{ip,i'p'}^{(0)}$ (a dynamic matrix at Γ -point, which contains zero eigenvalues corresponding to acoustic phonons), m_p is the mass of p -th atom, s is the number of atoms in the unit cell. For the cubic material, where all atoms are inversion centers, $T_{ip,i'p'}^{kl}$ can be found as

$$T_{ip,i'p'}^{jl} = \frac{1}{2} A_{ip,i'p'}^{(2)jl} \quad (5.48)$$

The matrices $A_{ip,i'p'}^{(0)}$ and $A_{ip,i'p'}^{(2)jl}$ are:

$$A_{ip,i'p'}^{(0)} = \sum_{n-n'} \Phi_{ip,i'p'}^{nn'} \quad (5.49)$$

$$A_{ip,i'p'}^{(2)jl} = - \sum_{n-n'} \Phi_{ip,i'p'}^{nn'} (\vec{R}_p^n - \vec{R}_{p'}^{n'})_j (\vec{R}_p^n - \vec{R}_{p'}^{n'})_l \quad (5.50)$$

where the summation is done over all unit cells (numbered with n), \vec{R}_p^n is the radius-vector of the p -th atom in the n -th unit cell, and $\Phi_{ip,i'p'}^{nn'}$ are Interatomic Force Constants (IFCs), which is a matrix consisting of potential energy second partial derivatives with respect to atomic

displacements with the macroscopic field contribution being excluded. Once IFCs are known, for instance, from first principles calculations, one can find the flexoelectric tensors following the theory discussed above.

5.3.2 Ab initio calculations of interatomic force constants

IFCs were calculated using PHonon program as it was already described in section 5.2.2. We used a 10x10x10 automatic Monkhorst-Pack grid of q-points, hence we know the IFCs for the supercell representing an array of 10x10x10 cells (225000 values of IFCs). The IFCs were calculated for exactly the same system as the previously obtained phonon dispersion curves: cubic STO under low pressure $p = 69$ kBar with lattice constant $a = 3.89$ Å, moreover it was extracted from the same run of ph.x code. Summing the IFCs and using (5.49) and (5.49) we obtained matrices $A_{ip,i'p'}^{(0)}$ and $A_{ip,i'p'}^{(2)jl}$.

5.3.3 Results

Dynamic flexocoupling coefficient

Knowing the $A_{ip,i'p'}^{(0)}$ matrix and the Born charges for STO (also obtained with QE)

$$\begin{aligned}
 Q_{\text{Sr}} &= \begin{pmatrix} 2.45 & 0 & 0 \\ 0 & 2.45 & 0 \\ 0 & 0 & 2.45 \end{pmatrix} \\
 Q_{\text{Ti}} &= \begin{pmatrix} 7.34 & 0 & 0 \\ 0 & 7.34 & 0 \\ 0 & 0 & 7.34 \end{pmatrix} \\
 Q_{\text{O1}} &= \begin{pmatrix} -2.00 & 0 & 0 \\ 0 & -2.00 & 0 \\ 0 & 0 & -5.75 \end{pmatrix} \\
 Q_{\text{O2}} &= \begin{pmatrix} -2.00 & 0 & 0 \\ 0 & -5.75 & 0 \\ 0 & 0 & -2.00 \end{pmatrix} \\
 Q_{\text{O3}} &= \begin{pmatrix} -5.75 & 0 & 0 \\ 0 & -2.00 & 0 \\ 0 & 0 & -2.00 \end{pmatrix}
 \end{aligned} \tag{5.51}$$

we calculated χ using formulas (5.44) and (5.44), as well as M coefficient using (5.43) and (5.47).

We got an agreement for dielectric constant and the absolute value of the dynamic flexoelectric coefficient, which are shown in Table 5.2. The microscopic method allows to resolve the sign

5.3. Determination of flexoelectric tensors using lattice dynamics

	Phonon dispersion	IFCs
χ/ϵ_0	3140	3050
$M (\times 10^{-8} \frac{\text{Vs}^2}{\text{m}^2})$	± 6.3	6.0

Table 5.2: Dielectric suitability, χ , and dynamic flexocoupling coefficient, M , obtained from the analysis of phonon dispersion curves and calculated from Interatomic Force Constants (IFCs).

of M and therefore the signs of previously obtained f_{44} and $f_{11} - f_{12}$ which are eventually positive.

Comments on the finding of the static flexocoupling tensor

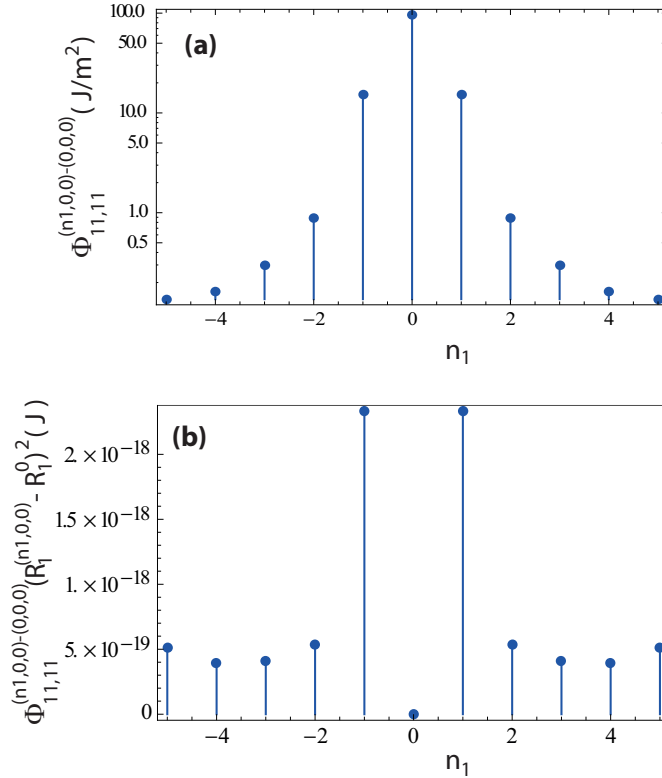


Figure 5.7: Convergence of IFCs (a) and momentum of IFCs (b) with the cell number n_1 . $\Phi_{11,11}^{(n_1,0,0)-(0,0,0)}$ represents a IFC between atom "1" (Sr) in the direction Ox_1 sitting in the $(n_1, 0, 0)$ cell and second atom "1" in the direction Ox_1 being in the "central" $(0, 0, 0)$ cell. $R_p^{(n_1,0,0)}$ is a radius vector to p -th atom in the $(n_1, 0, 0)$ cell. $n_1 = \pm 5$ corresponds to a cell at the edge of supercell.

One can find the static flexocoupling tensor using the matrix of momentums $A_{ip,i'p'}^{(2)jl}$, as it was done by Maranganti and Sharma [35]. However, we noticed that our result depends on the edge of the supercell or on the way we count the atoms in the sum (5.50). The matter

is explained as following. Since all such ab initio calculations give a finite number of IFCs one has to have a proper convergence of results with respect to the total number of IFCs considered. The χ and M coefficients are actually defined by the $A_{ip,i'p'}^{(0)}$ matrix (5.49), i.e. by the dynamic matrix at Γ -point. The f tensor is defined by $A_{ip,i'p'}^{(2)jl}$ containing not only IFCs but their momenta (5.50). Figure 5.7(a) shows the convergence of IFCs, $\Phi_{11,11}^{(n_1,0,0)-(0,0,0)}$, along Ox_1 direction between the atoms of Sr (atom "1" in the unit cell): one is sitting in the cell (0,0,0), the other - in the cell $(n_1,0,0)$, with the cell number n_1 . We numerate the cells with three indexes, $n = (n_1, n_2, n_3)$, since we work with 10x10x10 supercell. One can see a substantial decrease of IFCs with n_1 which insures the convergence of values of the $A_{ip,i'p'}^{(0)}$ matrix. However in Fig. 5.7(b) one can see that momenta of IFCs, do not reach convergence within the range of the used n . The divergence at the end of the supercell (large n) takes place because of DFT calculation limitations, namely because of periodic boundary conditions: the considered supercell actually "feels" the presence of infinite number of other supercells. This effect is magnified at the border of the supercell.

We demonstrate the divergence of the results, counting differently the momentums (Eq. (5.50)) of Sr atoms at the edge of the supercell, see Fig. 5.8. We obtain the following values for the f tensor:

$$f = \begin{pmatrix} -16.5 & 2.43 & 2.43 & 0 & 0 & 0 \\ 2.43 & -16.5 & 2.43 & 0 & 0 & 0 \\ 2.43 & 2.43 & -16.5 & 0 & 0 & 0 \\ 0 & 0 & 0 & -3.21 & 0 & 0 \\ 0 & 0 & 0 & 0 & -3.21 & 0 \\ 0 & 0 & 0 & 0 & 0 & -3.21 \end{pmatrix} \quad (5.52)$$

if the moments for the cells with $n_1, n_2, n_3 = \pm 5$ (the edge cells) are counted in the sum (5.50);

$$f = \begin{pmatrix} -3.1 & -1.48 & -1.48 & 0 & 0 & 0 \\ -1.48 & -3.1 & -1.48 & 0 & 0 & 0 \\ -1.48 & -1.48 & -3.1 & 0 & 0 & 0 \\ 0 & 0 & 0 & 0.62 & 0 & 0 \\ 0 & 0 & 0 & 0 & 0.62 & 0 \\ 0 & 0 & 0 & 0 & 0 & 0.62 \end{pmatrix} \quad (5.53)$$

if the moments for the edge cells are counted with the factor 1/2;

$$f = \begin{pmatrix} 6.19 & -3. & -3. & 0 & 0 & 0 \\ -3. & 6.19 & -3. & 0 & 0 & 0 \\ -3. & -3. & 6.19 & 0 & 0 & 0 \\ 0 & 0 & 0 & 1.96 & 0 & 0 \\ 0 & 0 & 0 & 0 & 1.96 & 0 \\ 0 & 0 & 0 & 0 & 0 & 1.96 \end{pmatrix} \quad (5.54)$$

5.4. Discussion and comparison with experiment

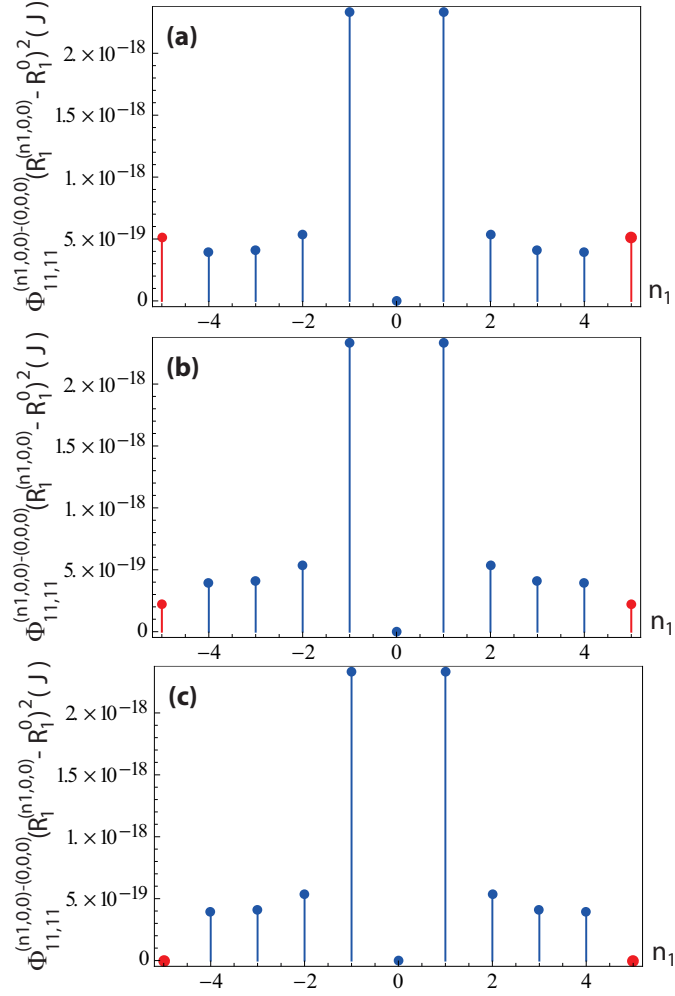


Figure 5.8: Convergence of momentum of IFCs with the cell number n_1 . $\Phi_{11,11}^{(n_1,0,0)-(0,0,0)}$ represents a IFC between atom "1" (Sr) in the direction Ox_1 sitting in the $(n_1, 0, 0)$ cell and second atom "1" in the direction Ox_1 being in the "central" $(0, 0, 0)$ cell. $R_p^{(n_1,0,0)}$ is a radius vector to p -th atom in the $(n_1, 0, 0)$ cell. $n_1 = \pm 5$ corresponds to a cell at the edge of supercell. (a) the moments of the edge cells are counted in the sum (5.50), (b) the moments of the edge cells are counted with the factor 1/2, (c) the moments of the edge cells are not counted.

if if the moments for the edge cells are not counted. From (5.52)-(5.54) one can see the drastic change of the obtained f values depending on the edge.

This way, using the standard precision of ab initio phonon dispersion calculations ($10 \times 10 \times 10$ q-point grid), we were not able to find reliably the static flexocoupling tensor components. Therefore, to have a reliable result one should consider a bigger supercell omitting some values of IFC at the edge.

χ/ϵ_0	3100
$M, \times 10^{-8} \frac{\text{Vs}^2}{\text{m}^2}$	6.3
$f_{11} - f_{12} \text{ (V)}$	2.0
$f_{44} \text{ (V)}$	2.2
$\mu_{11} - \mu_{12}, \frac{\text{nC}}{\text{m}}$	56
$\mu_{44}, \frac{\text{nC}}{\text{m}}$	61

Table 5.3: Material parameters of STO obtained joining the two methods based on phonon dispersions and IFCs. χ/ϵ_0 is relative dielectric susceptibility. f and M are static and dynamic flexocoupling coefficients. μ is static flexoelectric tensor.

5.4 Discussion and comparison with experiment

The results obtained with two above approaches are summarized in Table 5.3. The values of the static flexoelectric tensor, μ , are calculated using the Table 5.1 and Eq. (5.8).

Maranganti and Sharma [35] found static bulk flexoelectric tensor for some semiconductor and ferroelectric materials including STO using first principles calculations and the theory developed in [36]. They obtained for STO

$$\mu_{11} = 3.7 \frac{\text{nC}}{\text{m}}, \quad \mu_{12} = 0.3 \frac{\text{nC}}{\text{m}}, \quad \mu_{44} = 3.6 \frac{\text{nC}}{\text{m}}. \quad (5.55)$$

Unfortunately, they show only the values of flexoelectric tensor (not flexocoupling tensor), which is not informative, because flexoelectric coefficients depend on χ (Eq. (5.8)), and since the latter is highly temperature dependent, the values of μ obtained at 0 K can substantially change for the room temperature. Since they do not give the value of the dielectric susceptibility, we cannot make the comparison in terms of the flexoelectric coefficients. At the same time, we can compare the $(\mu_{11} - \mu_{12})/\mu_{44}$ ratio, which is about 0.94 for Maranganti and Sharma (see (5.55)) and 0.9 for us. However, there are strong arguments giving us right to doubt the validity of the results obtained by Maranganti and Sharma, since, to calculate phonon dispersion of STO, they used 6x6x6 grid of q-point which is insufficient for convergence as it was shown above.

It is also interesting to have a look on the previously obtained experimental results. Tagantsev et al [6] determined total flexoelectric coefficients, $|f_{44}^{\text{tot}}| = 2.2 \text{ V}$, for crystalline STO based on experimental data of Brillouin scattering by Hehlen et al [94]. The information on the flexoelectric coupling can also be obtained from a treatment of the low-energy phonon spectrum of a crystal probed with the neutron scattering technique. In this case, the energy resolution is much lower than in the Brillouin scattering technique but the spectrum is available in the whole Brillouin zone. However, this analysis was done with the contribution of the dynamic flexoelectric effect being omitted. Thus, such a treatment of a spectrum gives some effective values of the flexocoupling coefficients f^{eff} . For STO it was obtained $|f_{44}^{\text{tot}}| = 1.2 - 2$ and $|f_{11}^{\text{tot}} - f_{12}^{\text{tot}}| = 1.2 - 1.4 \text{ V}$ [24]. The spread of obtained values indicates a low precision of neutron

scattering based experiments. In addition, as was indicated in the preceding subsection, this technique does not yield the sign of flexoelectric components.

Zubko et al [31] employed a bending method to characterize the flexoelectric response in single crystals of STO. To get all the three independent coefficients characterizing the flexoelectric response of cubic STO the authors performed bending experiments with different orientations of the beam. We cannot compare our results with that by Zubko, since these experiments have a substantial drawback, which is the presence of surface contribution to bulk flexoelectric response [24], which strongly changes the bulk flexoelectric values. Additionally, pure bending experiments yield only two independent equations for the three components of the flexoelectric tensor and the authors combined their data with the component $f_{44} = 2.2$ V of the flexocoupling tensor taken from the Brillouin scattering to find $f_{11} = 0.08$ V and $f_{12} = 2.6$ V. Such a combination should not be done, since flexocoupling tensor taken from the Brillouin scattering is actually a total flexocoupling coefficient containing both f_{44} and M , therefore one should not combine total and static coefficient whose values can drastically differ.

5.5 Conclusions

Summing up this chapter we would like to highlight some essential moments. It was shown with the example of STO that we can use 0 Kelvin DFT calculations stabilizing the perovskites structure with pressure. Moreover, it is possible to greatly change the dielectric constant of the material providing analog to Curie-Weiss law.

To calculate static and dynamic flexoelectric tensors, we used ab initio calculations and two phenomenological methods based on the calculated dynamical matrices. The first method consists of the analysis of phonon dispersion curves. It gives f and M tensors within the sign ambiguity and it is not able to resolve the $f_{11} - f_{12}$ difference. The obtained values are comparable with previously reported. The considered analysis can be used with real experimental data of phonon dispersion to find flexoelectric coefficients.

The second method uses microscopic parameters of the material, i.e. IFC. This method can, in principle, provides all components of f and M tensors. With this method the dynamic flexoelectric coefficient was for the first time calculated for cubic STO. As expected from previous estimations, M has a significant contribution to f^{tot} and should be taken into account. However, within this method the standard precision for dispersion curves calculations (10x10x10 q-point mesh) is not enough to find f tensor. To calculate static flexoelectric tensor the method requires smaller mesh of q-points (more atoms in the supercell).

6 Ferroelectric antiphase boundaries in antiferroelectric materials

Since this thesis is mainly focused on DFT calculations of ferroelectrics, it is interesting to see what first principles methods can offer if we study domain boundaries of ferroelectrics and antiferroelectrics. In this chapter, using ab initio modelling we will show that antiphase boundaries in antiferroelectric PbZrO_3 (PZ) may possess ferroelectricity supporting the transmission electron-microscopy (TEM) experiments by Wei et al. [98].

6.1 Introduction

Domain boundaries make an intriguing and challenging research subject due to their distinctive properties and promising perspective in designing nanoelectronic devices. A typical example is the discovery of electronic conductivity at ferroelectric domain walls in multiferroic oxides such as BiFeO_3 [99–101] and ErMnO_3 [102]. Charged domain walls in the ubiquitous BaTiO_3 ferroelectric showed electron-gas like conductivity while the individual domains remained excellent insulators [103]. Large photovoltages were generated by domain walls, attractive for photovoltaic devices [104]. These properties are particularly attractive because domain walls can be created, annihilated, rewritten and displaced electrically inside the material, potentially leading to agile nano-electronics.

Recently, the polarity of twin boundaries in centro-symmetric CaTiO_3 was shown [105]. Possible polarity of domain boundaries in non-polar materials and, to a greater extent, local ferroelectricity in such boundaries make these objects attractive for both fundamental science and possible practical future applications.

How to identify materials with ferroelectric boundaries? Based on a Landau theory treatment, one can show that antiphase boundaries in antiferroelectrics are likely ferroelectric. Implementing this result and using an atomic scale experimental study of the prototypical antiferroelectric lead zirconate [98], exploiting a negative spherical-aberration imaging (NCSI) technique [106] in an aberration-corrected TEM, it can be demonstrated that antiphase boundaries with a π phase-shift of the order parameter exhibit polarity, which, in view of the

symmetry of the system, implies the existence of local ferroelectricity.

6.2 Theory of ferroelectricity in antiferroelectric domain walls

Antiferroelectrics constitute a large group of dielectric materials which can be experimentally recognized by a structural phase transition between two non-polar phases with a strong dielectric anomaly at the high temperature side of the transition [107–109]. Antiferroelectricity is a result of the interruption of an imminent ferroelectric phase transition having Curie temperature of T_0 by a structural phase transition [110] at a slightly higher temperature T_A . This interruption occurs due to repulsive interaction between polarization and a structural order parameter appearing at T_A .

A simple two instabilities Landau-type theory [110–113] rationalizes the antiferroelectric behaviour using the following free energy expansion in terms of polarization, P , and structural order parameter, ξ ,

$$F(P, \xi) = \frac{A}{2}(T - T_0)P^2 + \frac{\eta}{2}P^2\xi^2 + F_A(\xi) \quad (6.1)$$

Here the coefficient $\eta > 0$ controls the repulsive biquadratic coupling between polarization and structural order parameter. The transition at T_A is described by the contribution to the free energy $F_A(\xi)$, implying softening of a lattice mode associated with the order parameter ξ . For the low-temperature phase where the order parameter of the transition, ξ , acquires a spontaneous value of ξ_0 , the susceptibility, defined as

$$\chi = 1 / \frac{\partial^2 F}{\partial P^2}, \quad (6.2)$$

takes the form

$$\chi = \frac{1}{A(T - T_0) + \eta\xi_0^2}. \quad (6.3)$$

Equation (6.3) corresponds to antiferroelectric-type anomaly if $A(T - T_0) + \eta\xi_0^2$ increases on cooling. This is possible if the increase of ξ_0 with lowering temperature dominates the behaviour of this term, which can be assured by large enough coupling constant η .

The above scenario suggests that domain boundaries provide favorable conditions for the development of local ferroelectricity. This can be elucidated considering the simplest type of ferroic domain boundary, the so-called Ising wall. In such wall the order parameter ξ passes through zero in the middle of the boundary. Thus, in the middle of the boundary, the suppressing effect of the structural ordering (with respect to the ξ -parameter) on the ferroelectric instability vanishes, creating favorable conditions for the development of local ferroelectricity at $T < T_0$.

6.2.1 Antiphase boundaries in lead zirconate - candidates for ferroelectricity

The concept presented above can be applied to PZ. However, in PZ the situation is more complicated. At high temperatures, PZ has the ideal cubic perovskite structure shown in Fig. 6.1(a). After cooling through a first order phase transition at $T_A \sim 500$ K, the structure changes from cubic $m\bar{3}m$ to orthorhombic mmm . The structural changes at the transition can be presented as a combination of displacements in two lattice modes [114], one corresponding to the Σ point (the wave vector $\vec{k}_\Sigma = \frac{2\pi}{a_c}(1/4, 1/4, 0)$; a_c is the lattice constant of the high-temperature cubic phase) in the Brillouin zone and the other corresponding to the R point ($\vec{k}_R = \frac{2\pi}{a_c}(1/2, 1/2, 1/2)$). The distortions associated with the Σ point are mainly related to displacements of lead ions (Fig. 6.1(b)) while those associated with the R point derive from antiphase rotations of the oxygen octahedra (Fig. 6.1c) about the crystallographic axes of the cubic phase. Thus, the transition is governed by a mixed order parameter, containing Σ -point and R -point-related components.

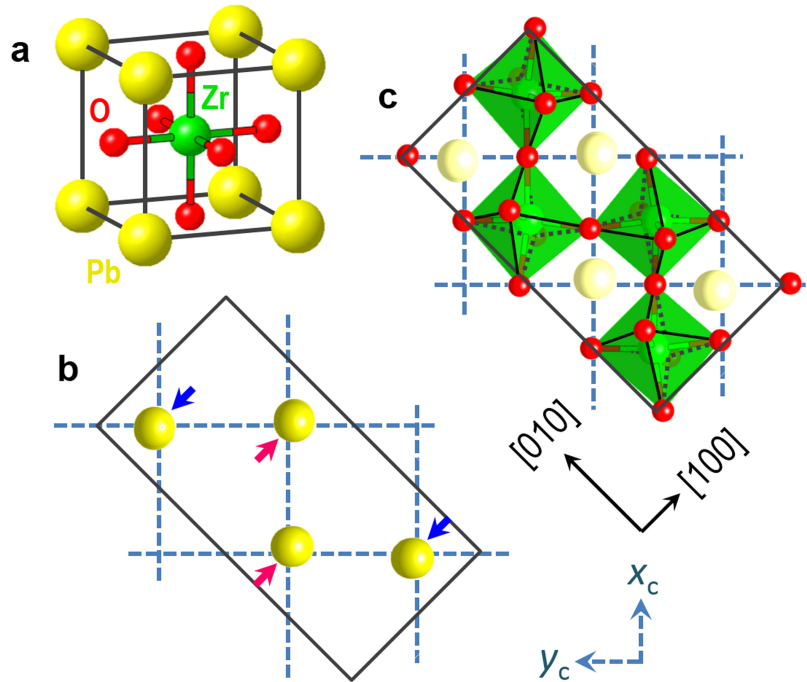


Figure 6.1: Structure of lead zirconate. a. The cubic unit cell. Lattice modes relevant to the phase transition into the orthorhombic phase: b. Lead displacements in the Σ -mode. c. Oxygen-octahedron rotations in the R -mode. In b and c, the projections of the orthorhombic unit cells onto the ab plane (rectangles) are shown. The crystallographic axes of the orthorhombic phase ($[100]$ and $[010]$) and of the pseudo-cubic phase (x_c and y_c) are shown.

The possibility of local ferroelectricity in domain boundaries can be discussed referring to the Σ -point-related component of the order parameter, corresponding to the so-called Σ_3 mode

of the parent cubic structure, with lead displacements having the form [110, 115]

$$r_{\text{Pb}} \propto \begin{pmatrix} -1 \\ 1 \\ 0 \end{pmatrix} \cos\left(\frac{\pi}{2a_c}(x_c + y_c) + \phi\right) \quad (6.4)$$

where $x_c = n_1 a_c$, $y_c = n_2 a_c$ (n_1 and n_2 are integers) are the coordinates in the cubic lattice frame and ϕ is the phase of the modulation.

The condensation of the order parameter linked to this mode is associated with a 4-fold increase of the number of atoms per unit cell as schematically depicted in Fig. 6.1(b). As a result, two types of domain states form: orientational and translational [116]. The orientational states (ferroelastic twins) differ by the orientation of the atomic displacements. The translational domain states that correspond to a given orientational state can be turned from one to another by shifting the lattice by a_c , $2a_c$, or $3a_c$, corresponding to a fraction of a lattice translation vector of the low-temperature phase. In view of the quadrupling of the unit cell, there are 4 translational domain states for each orientational state. In terms of Eq. (6.4), lead displacements in these states corresponds to $\phi = \pi/4, 3\pi/4, 5\pi/4$ and $7\pi/4$ [110]. These states can be visualized in the plane of the complex order parameter $\xi = \rho e^{i\phi}$, corresponding to the points marked with four circles (Fig. 6.2(a)), where ϕ is the phase of the order parameter and ρ is its modulus, proportional to the magnitude of lead displacements.

Three types of translational boundaries, corresponding to phase shifts of $\pi/2$, π , and $3\pi/2$ can separate the four translational states. The mappings of these translational boundaries are schematically shown in Fig. 6.2(a) with solid lines. Mapping "3" is of a particular interest for the appearance of the local ferroelectricity. It corresponds to a π -wall, (so-called antiphase boundary (APB)) i.e. having a phase shift of π , at the middle of which the order parameter passes through the zero point hence the suppressing effect of the order parameter on to the ferroelectric instability is reduced. Following this argument one might contemplate a $\pi/2$ translational domain boundary where the order-parameter passes as well through zero (mapping "2" in Fig. 6.2(b)) and wonder if also in this case the ferroelectric instability is favoured. No theory of translational domain boundaries in PZ is available at present to quantitatively address this problem. However, such a problem has been addressed for an improper ferroelectric by Fouskova and Fousek [117]. These authors compared the energies of two variants of a domain wall in gadolinium molybdate (GMO), which have mapping onto the plane of the two-component order-parameter (q_1, q_2) marked with solid lines "1" and "2" in 6.2(b). They demonstrated that the variant corresponding to mapping "2", which passes though the origin is energetically unfavorable compared to the rotational variant, corresponding to mapping "1". The problem in GMO is isomorphous to that in PZ to within the substitution ($\text{Re } \xi, \text{Im } \xi$) for (q_1, q_2). The results obtained for GMO enables speculating that passing through zero of the order parameter in a $\pi/2$ translational domain boundary in PZ is quite improbable. On the same lines, in orientational (twin) domain boundaries, which are also comparable to the walls treated by Fousek and Fouskova, the order parameter is not

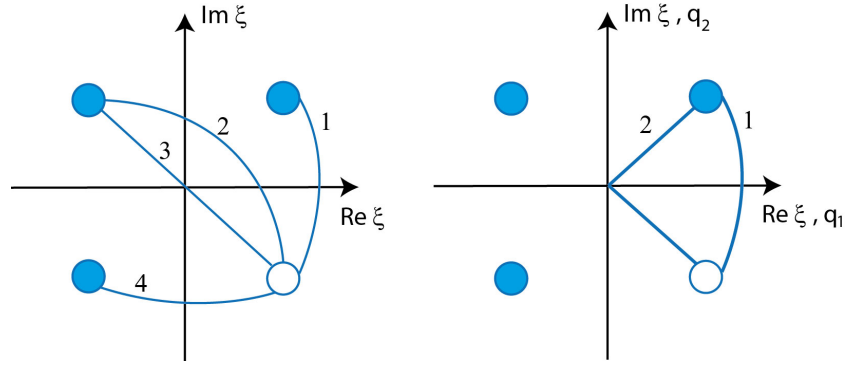


Figure 6.2: Mapping of the translational domain states and boundaries inside a single orientational domain of PbZrO_3 onto the plane of the complex order parameter. Circles - translational domain states. Lines - translational boundaries. The boundaries linking the domain state marked by empty circle with the other states are shown with numbered lines. (a) Naturally expected translational boundaries. The phase shifts $\Delta\phi$ of the modulation of the lead displacements in the walls are: line 1 - the $\pi/2$ wall, $\Delta\phi = \pi/2$; lines 2 and 3 - the π walls (antiphase boundary), $\Delta\phi = \pi$; line 4 - the $3/2\pi$ wall, $\Delta\phi = 3/2\pi$. In the π -wall (line "3") the order parameter passes through zero. In view of the above discussion, in such wall the suppressing effect of the order parameter on the ferroelectric instability is minimal making the π -wall the most favorable for the occurrence of local ferroelectricity. (b) Mappings of possible $\pi/2$ walls onto the plane ($\text{Re } \xi, \text{Im } \xi$) of the complex amplitude of the order parameter in PZ - solid lines 1 and 2. Mappings of possible ferroelectric walls onto the plane (q_1, q_2) of the two-component order parameter in GMO - solid lines 1 and 2.

expected to pass through zero in the wall neither. This implies that there is no special reason for the appearance of local ferroelectricity in twin boundaries, though such event cannot be excluded. It is therefore the π wall which is promising for the local ferroelectricity. This way, APBs in PZ, i.e. translational boundaries with phase shifts of π , are good candidates for the occurrence of local ferroelectricity.

6.2.2 The thickness of antiphase boundaries in ferroics

The above discussion motivates experimental search for ferroelectricity in APBs in PZ. For such research, it seems appropriate to specify the notion APB in ferroics, which not fully identical to that commonly used in non-ferroic materials.

By definition, any two elementary unit cells in a perfect crystalline structure can be superimposed by translation with an elementary vector belonging to the set of the lattice translation vectors of the structure. Some crystals exhibit distinct neighboring regions, where a unit cell in one can superimpose a unit cell in the other by the application of a vector differing from an allowed lattice translation vector by approximately half of an elementary lattice translation vector. In this case the boundary separating the two regions is called antiphase boundary. Hereafter, the aforementioned translation vector is called an APB vector. This

primary definition of the APB is termed *definition-0*.

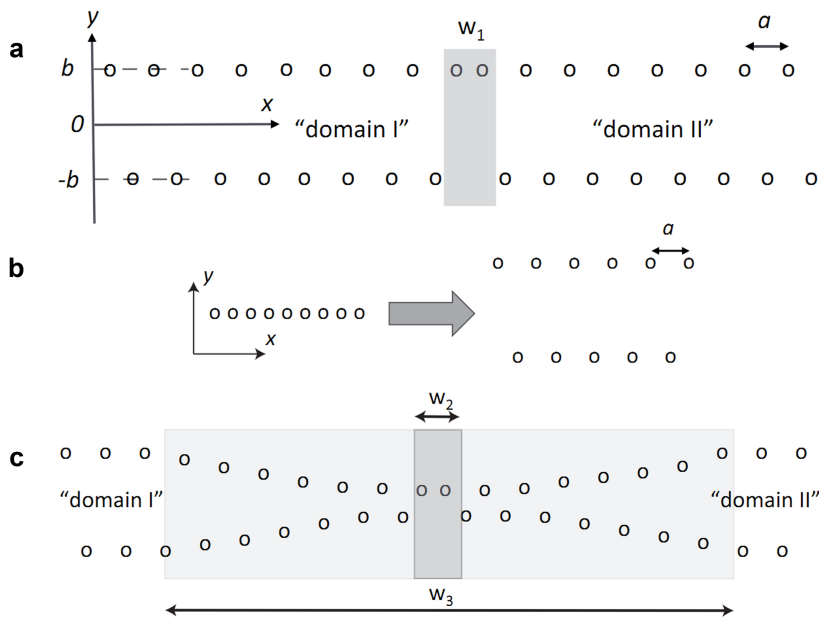


Figure 6.3: Antiphase boundary (APB) in a "non-ferroic" vs. APB in a ferroic. (a) 2D schematic of an APB in a "non-ferroic". Here only one chain of atoms parallel to the Ox direction is shown and the whole 2D "crystal" can be obtained by repeating this chain in the Oy direction with a period c . Regions "domain I" and "domain II" have both a perfect crystalline structure with period a . Yet, in order to superpose elementary cell of region I onto region II, a vector is needed, which differs from a translational vectors by $a/2$. This vector does not belong to the set of elementary lattice translation vectors of the structure, all equal na , n being integer numbers. The antiphase boundary w_1 is marked grey and its width is about $a/2$. (b) 2D schematic of a structural phase transition in a ferroic. In each phase, only one chain of atoms is shown; the whole 2D "crystal" can be obtained by repeating the chain in the perpendicular direction with the period c . At the transition, the period in the direction of the chain changes from $a/2$ to a . (c) Schematic of an APB in the 2D ferroic introduced in Fig. 6.2(b). The thickness of the APB consistent with its primary definition (*definition-0*) is w_3 . According to *definition-1* one would attribute to the APB the thickness w_2 .

Figure 6.3(a) shows a 2D schematic of an APB. Here only one chain of atoms parallel to the Ox direction is shown and the whole 2D "crystal" can be obtained by repeating the chain in the Oy direction with a period c . In this drawing, the APB vector differs from a lattice translation vector exactly by $a/2$, i.e. by a half of the elementary translation vector. In a more realistic model, the separation between the neighboring "atoms" in the Ox directions should be $a/2$ only inside regions of "domain I" and "domain II" of the structure while at the APB it should evidently be slightly different from this value.

For the model depicted in Fig. 6.2(b), another definition of the APB (termed hereafter *definition-1*) can be introduced based on *definition-0* given above. Specifically, it is seen that the regions "I" and "II" can be characterized by the alternation of the signs of the atomic

6.2. Theory of ferroelectricity in antiferroelectric domain walls

displacements along the Oy direction, which are either b or $-b$. As is clear from Fig. 6.3(a), one can identify the presence of the APB by a shift of the phase of this alienation and ascribe the position of the APB to the place where this phase shift takes place. For the model depicted in Fig. 6.3(a), the APB can be viewed as a layer which is $a/2$ thick in the Ox direction. In terms of *definition-0*, by removing away this layer, the periodicity throughout the whole system, which was violated by the presence of the APB, is restored. In terms of *definition-1*, at this layer, the regular alternation of the atomic displacements in the Ox direction is violated. Based on any of the two definitions, one can attribute to the APB the width of a and speak about its location with the accuracy of the interatomic distance. *Definition-1* is more convenient in practical work compared to *definition-0*.

The model depicted in Fig. 6.3(a), corresponds to the situation in non-ferroic crystals. Meanwhile, for ferroics, that situation is, in general, different and requires a special treatment. The new features are as follows: (i) *definition-1* is not consistent any more with the primary *definition-0*, and (ii) a thickness equal to the correlation length rather than the interatomic distance should be ascribed to the APB. This situation is discussed next.

In ferroics, APBs occur once a structural phase transition is accompanied with a unit cell multiplication. Figure 6.3(b) shows the evolution of the structure at such a phase transition in a ferroic "material" where the unit cell volume is doubled at the transition and the period in the Ox direction changes from $a/2$ to a . Specifically, the structural evolution shown in this figure corresponds to the case, where, in the ordered phase, the structure is in a single domain state. It is seen that that such single domain structure is equivalent to that inside regions "I" and "II" of the non-ferroic 2D crystal shown in Fig. 6.3(a).

In such a ferroic 2D crystal, APBs may readily occur, separating between so-called translational domains. Specifically, for a ferroic having a second order phase transition or of a first order close to the second order transition (the typical situation which enables the Landau-theory treatment), in an APB, the structure evolves gradually between the two translational domains on a spatial scale of about the correlation length ζ . The primary statement of the Landau theory is that ζ is much larger than the lattice constant of the material. In practice, due to an interplay of numerical factors such difference may not be very large, however, conceptually, ζ should be larger than the lattice constant. A ferroic "material" exhibiting two translational domains marked with "I" and "II", which are separated by an APB, is schematically depicted in Fig. 6.3(c).

Now, there is a question of the thickness and position of a ferroic APB. Using *definition-0*, one treats the APB as the area different from the translational invariant domains "I" and "II". Note that the translational invariance requires not only the periodicity in the Ox direction but also the identity of the atomic displacements in the Oy direction. Thus, one considers the antiphase boundary as an object having the thickness $w_3 \cong \zeta$. The APB is the whole region, with the thickness of about ζ , where the lattice periodicity is violated. Once the APB contains many distorted unit cells, one can say that, in an APB, the modulus of the order parameter

deviates from its bulk value.

Can one apply *definition-1* to an APB in ferroics? In *definition-1*, one considered the APB to be atomically thin (in Fig. 6.3(c) it is w_2) and specified its location to within the interatomic distance. However in ferroics this definition loses its essential feature. Specifically, in non-ferroics *definition-1* is equivalent to the primary *definition-0*. On the contrary, in ferroics, *definition-1* is in conflict with the primary *definition-0*. In a ferroic material, two unit cells separated just by the APB of *definition-1* cannot be superimposed by any translational vector at all, thus it is impossible to speak about a phase shift at it. Thus, strictly speaking, when applied to ferroics, *definition-1* of the APB does not correspond to the term "APB" itself.

To summarize, APBs in ferroics are objects of a finite volume, not just a stepwise break of the periodicity.

6.3 Electron microscopy experiments

Following the above analysis, Wei et al [98] investigated PZ to search for local polarity in its domain boundaries. Employing the NCSI technique [106] in an aberration-corrected TEM combined with quantum-mechanical and optical simulation, they imaged and measured the atomic positions, including those of oxygen.

Figure 6.4(a) is a dark-field image of a PZ crystal, showing translational domains separated by domain walls (dark line contrast). These translational domains correspond to a single orientational domain. The topological nature of the domain walls, allows reactions between them, provided the conservation of the total phase shift (topological charge) is kept. Encircled and marked "1", "2", and "3" are annihilation of two APBs, annihilation of one APB and two $\pi/2$ walls, and split of an APB into two $\pi/2$ walls, respectively.

A high-resolution TEM image of APB is shown in Fig. 6.4(b). It was recorded under NCSI condition with the electron beam along the crystallographic [001] direction. One readily checks that the two highlighted unit cells exhibit a π shift in the phase of the order parameter. The identity of these two unit cells can be checked with lead displacements. Passing a pair of rows in the [010] direction, the sign of lead displacements alternates as shown with the blue/pink arrows in Fig. 6.4(b), following the law of the alienation dictated by Eq. (6.4). The number of lead containing rows between the two highlighted unit cells is 10 (and not a multiple of 4), evidencing the π phase shift and the existence of the APB region. Based on image simulation, the atomic positions corresponding to the experimental image are obtained from the model structure.

A violation of the correlation in the antipolar in-plane Pb displacements is clearly seen in the APB area (Fig. 6.5(a)). Due to the depolarizing effect, polarity is expected only in the boundary plane, i.e along the [100] orthorhombic axis. Scrutinizing the x -atomic displacements shown in Fig. 6.5(b), they find a systematic unipolar displacements of Zr in 7 elementary cubes

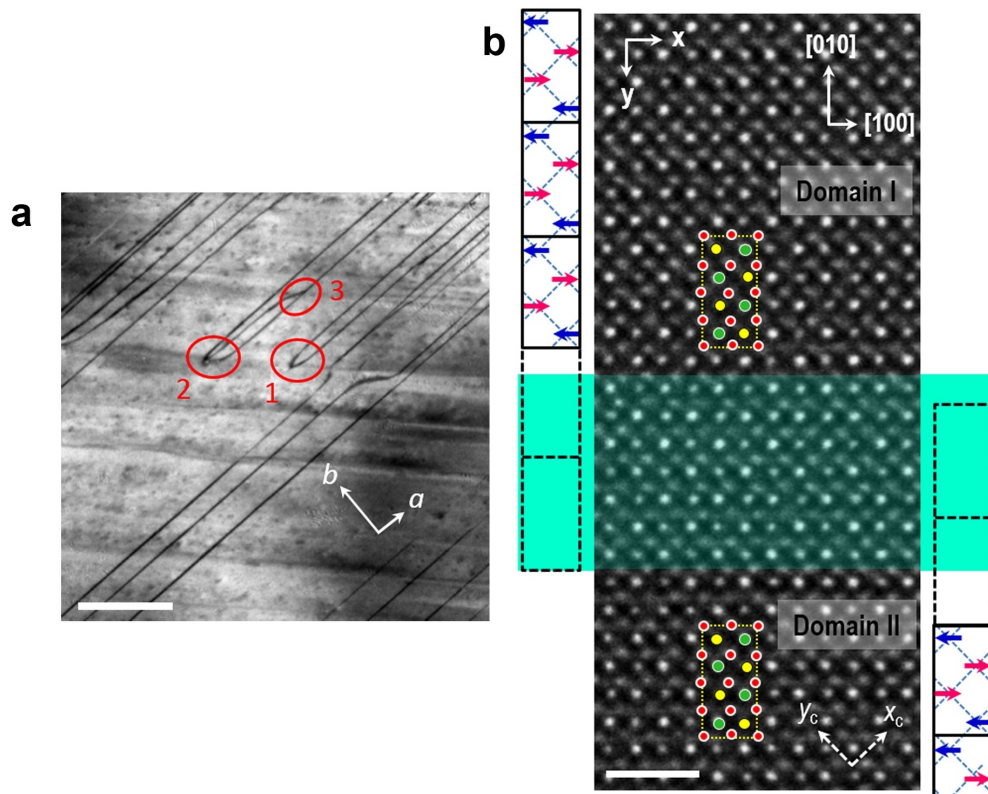


Figure 6.4: Morphology of translational boundaries in the antiferroelectric PZ crystal. (a) Dark-field image with superposed orthorhombic axes shows morphology of the translational boundaries (dark lines). Topological features of these boundaries are marked by the red circles: "1" - annihilation of two antiphase boundaries (APBs), "2" - annihilation of one APB and two $\pi/2$ walls, and "3" - split of an APB into two $\pi/2$ walls. (b) Atomic-resolution image of an APB between two translational domains recorded under NCSI conditions with the incident electron beam parallel to the [001] direction. In two domains, two identically defined orthorhombic unit cells are highlighted. Lead atom displacements are represented in the schematic orthorhombic blocks to the left (domain I) and the right (domain II) of the image. By shifting the orthorhombic cell, the APB (the shaded cyan area) can be evidenced by the conflict of half a unit cell in between these two domains. The scale bar in (a,b) is 200 nm and 1 nm, respectively.

(pseudo-cubic unit cells) with an average value of about 8pm. This hints to a dipole moment inside the wall, having a dipole moment density of about $11 \mu\text{C cm}^{-2}$, obtained taking $a_c = 0.413 \text{ nm}$ and 6 electron charges for the Zr Born charge.

To evaluate the polarity of the APB, Wei et al used the following approach: they calculated the dipole moments based on the displacements of all the ions from their positions in the cubic phase associated with their Born charges. Then, they averaged these moments over the projection of the orthorhombic unit cell onto the ab plane using a "sliding" unit cell. By the "sliding" cell they mean the orthorhombic cell of 40 atoms shifted each time along [010] axis

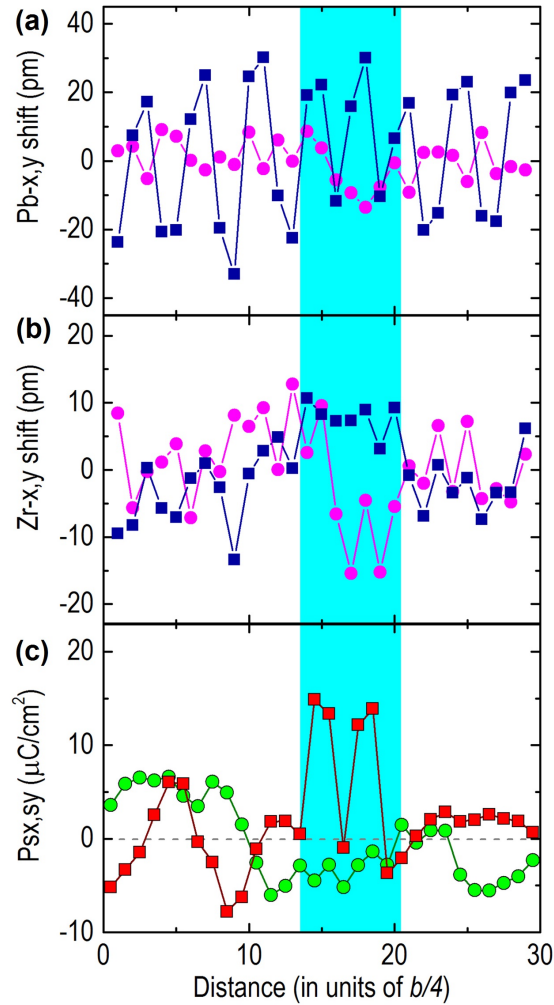


Figure 6.5: Atomic displacements of translational boundaries in the antiferroelectric PZ crystal. (a) and (b) displacements of Pb and Zr atoms with respect to the atomic positions of the cubic phase, averaged over the planes along x direction as function of the plane positions along y direction. Blue squares: in-plane (the x direction, [100] in Fig. 6.1) displacements parallel to the wall; pink circles: out-of-plane (the y direction, [010] in Fig. 6.1) displacements normal to the wall. (c) Dipole moment density obtained by averaging the dipole moments of a "sliding" orthorhombic unit cell plotted as a function of the centers of the sliding cells. Red squares: in-plane polarity; green circles: out-of-plane polarity.

by $b/4$ (Fig. 6.6).

Figure 6.5(c) shows the dipole moment density obtained this way, as a function of the center of the sliding unit cells. Note that this figure shows a deviation from zero polarity in the centro-symmetric domain-bulk. This deviation indicates the measurement errors (standard deviation $\sigma < 5 \mu\text{C cm}^{-2}$) of the polarization calculated this way. This relatively low accuracy is not surprising when calculating the dipole moments of a 40 atom unit cell of the orthorhombic PZ. Importantly, one can ascribe in-plane polarity to the APB area, corresponding to some

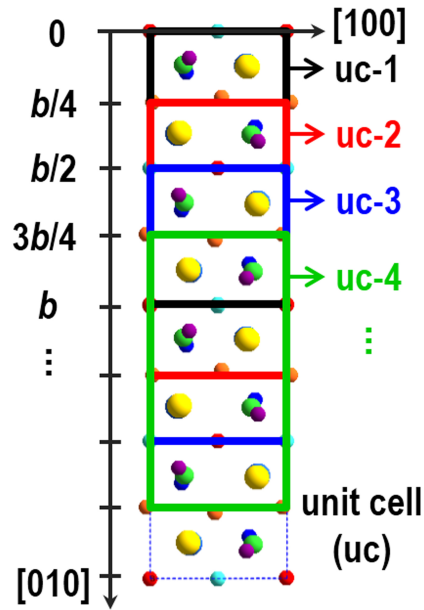


Figure 6.6: Schematic diagram of the "sliding" orthorhombic unit cell. Based on the structure model derived from the image simulation, the spontaneous polarization is calculated for each unit cell, then the cell is shifted by $b/4$.

$14 \mu\text{C cm}^{-2}$, definitely exceeding the "noise" level. The contribution of B-site to the polarity in the wall can be taken as an indication that the B-site atoms contribute to the ferroelectric soft mode of the material. From Fig. 6.5(c), it is also clear that no polarity normal to the boundary can be ascribed to APB, which is consistent with the expected manifestation of the depolarizing effect.

6.4 Ab initio simulations

Following the TEM experiments by Wei et al, we investigated the presence of local polarity in the APB in PZ by first principles calculations.

To perform first principles full relaxation calculations we used PWSCE. The calculations were performed within the GGA with PBE exchange-correlation functional using ultrasoft pseudopotentials by Vanderbilt [80]. The kinetic energy cutoff for wavefunctions was 60 Ry (816 eV). The kinetic energy cutoff for charge density and pseudo potential was 720 Ry. The remained force after ionic minimization was about 10^{-3} a.u. (21 meV \AA^{-1}) for the bulk PZ and 10^{-2} a.u. (0.21 eV \AA^{-1}) for the supercell simulating APB in PZ.

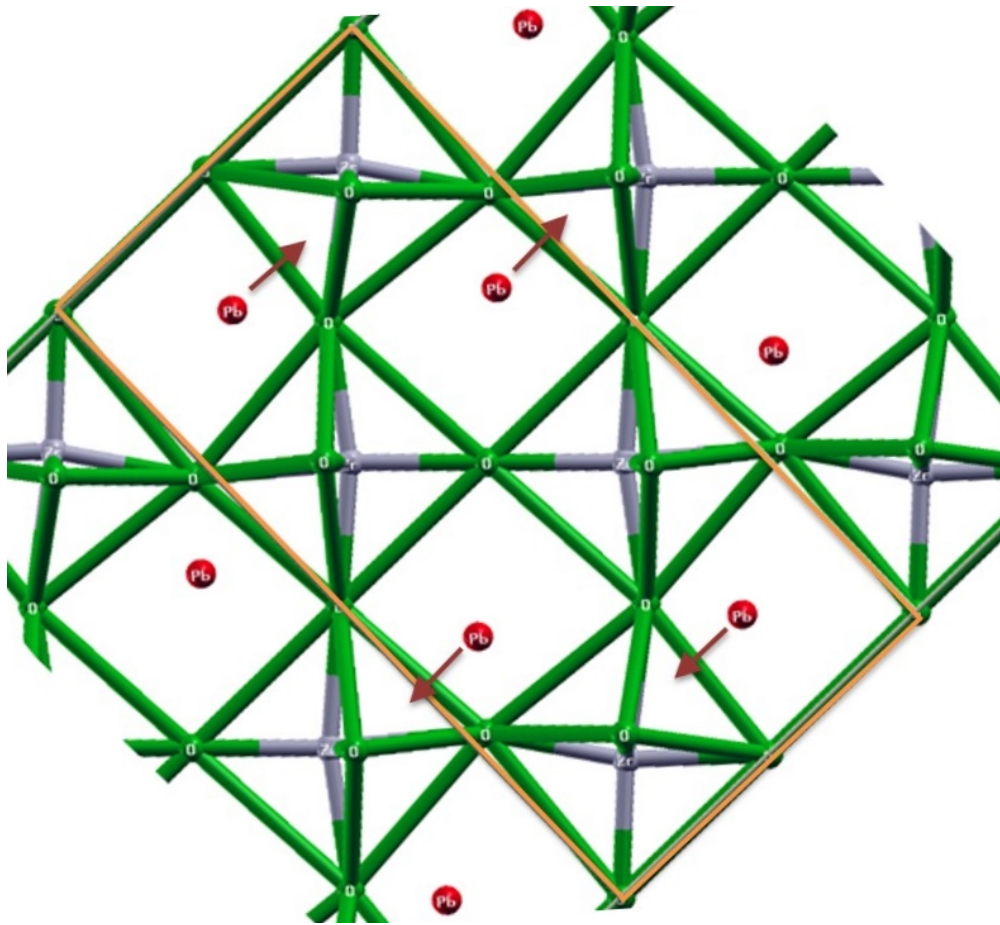


Figure 6.7: Calculated bulk structure of PZ. The calculations reproduce the features of the real material such as antiparallel lead atom displacements and antiphase correlated rotation of the oxygen octahedra. The displacements of Pb atoms are schematically shown with arrows.

6.4.1 *Ab initio* calculations of bulk lead zirconate

As a starting point for the calculations we obtained a relaxed PZ orthorhombic cell of 40 atoms with $a = 6.056 \text{ \AA}$, $b = 11.954 \text{ \AA}$ and $c = 8.334 \text{ \AA}$ (experimental values are $a = 5.884 \text{ \AA}$, $b = 11.787 \text{ \AA}$, $c = 8.231 \text{ \AA}$ [118]) exhibiting all the specific features of the structure, such as 8 times multiplication of the cubic unit cell, antiparallel Pb atom displacements, and O octahedron rotations (compare Figs. 6.7 and 6.1). This result is consistent with first principles results obtained by Waghmare and Rabe [119].

6.4.2 *Ab initio* calculations of APB in lead zirconate

Further, we constructed a 220 atoms supercell (5.5 orthorhombic cells) simulating a π phase shift in APB corresponding to the TEM experiment. The two end cells of the supercell had a fixed orthorhombic structure corresponding to that of the PZ inside the adjacent domains and

the inner 3.5 orthorhombic cells were relaxed (Fig. 6.8).

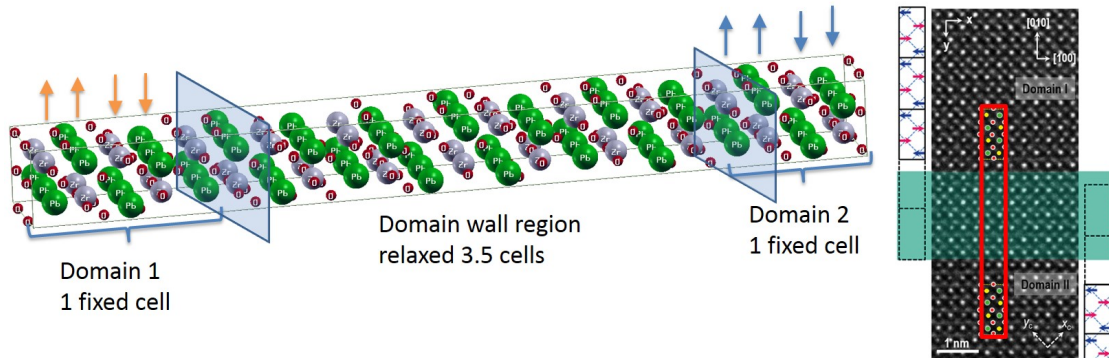


Figure 6.8: Ab initio calculation of antiphase boundary in PZ. The two end cells of the supercell have a fixed orthorhombic structure corresponding to that of the PZ inside the adjacent domains. The inner 3.5 orthorhombic cells are relaxed. The displacements of Pb atoms are schematically shown with arrows.

We calculated the polarization of the APB using the "sliding" cell by atom displacements with respect to the cubic phase multiplied by Born charges, calculated with PWSCF (for [100] direction, $Z_{\text{Pb}} = 3.889$, $Z_{\text{Zr}} = 5.996$, $Z_{\text{O}1,\text{O}2} = -2.464$, $Z_{\text{O}3,\text{O}4,\text{O}5} = -3.718$). The corresponding atom displacements and polarity are shown in Fig. 6.9. Because of depolarizing field, the out-of-plane polarity (green circles) has much smaller values than the in-plane polarity (red squares), which is similar to the experimental behaviour (Fig. 6.5). We would like to underline that we calculate polarization using Born charges (and not Berry phase approach) on purpose. The reason for this is that we show our ab initio results in comparison with the experiment, namely, we compare the atomic behaviour in the APB region using experimental data and first principles calculations. The "experimental" polarization was calculated by atomic displacements and Born charges (Wei et al. took the values of Born charges from our first principles calculations), this way we believe that it is worth calculating the "ab initio" polarization using the same approach for a clearer comparison with the experiment. The ab initio results confirmed the observed with TEM polarity and agreed qualitatively with the experimental results. The width of the APB region was found to be about 2 orthorhombic cells.

We estimated the surface formation energy of the π -wall considered above. We compared the energies of the super cell (5.5 orthorhombic cells) simulating the APB region and of the 5.5 cells of the bulk PZ. The value of the surface formation energy was found to be about 190 mJ m^{-2} .

Our simulations also demonstrated the bistability of the polar state of APBs in PZ. The energy of the two configurations of atom displacements shown for lead atoms in Fig. 6.10 was found to be equivalent (they have the same energy). Thus, the structure was found to be bistable. Hence the ab initio calculations showed both, the presence of local polarity, and the possibility of polarization switching, supporting the ferroelectric nature of APB.

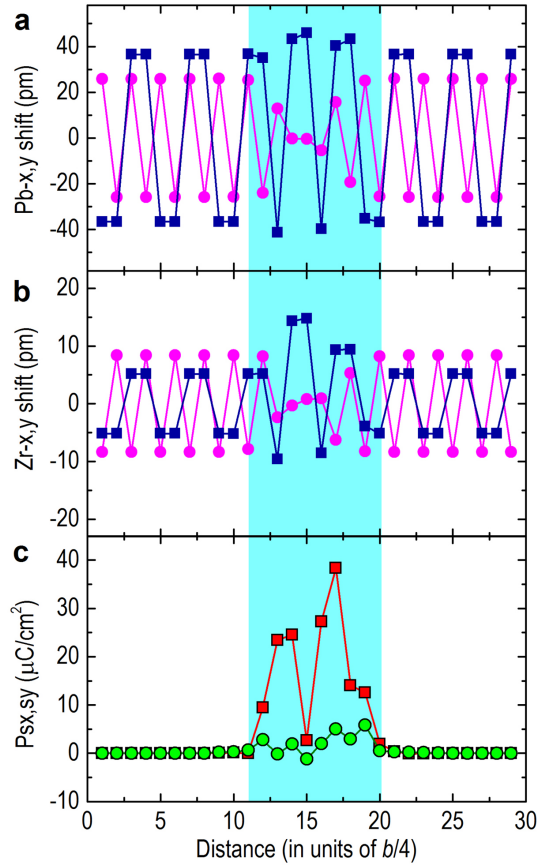


Figure 6.9: Results of ab initio calculations. (a) and (b) Displacements of Pb and Zr atoms with respect to the atomic positions of the cubic structure, squares: in-plane (x direction) displacements parallel to the wall, circles: out-of-plane (y direction) displacements normal to the wall. (c) Dipole moment density for the "sliding" orthorhombic unit cell plotted as a function of the centers of the sliding cells; squares: in-plane polarity, circles: out-of-plane polarity.

6.5 Discussion

The performed ab initio calculations give a further support to the experimental observations by Wei which provide experimental evidence for the anticipated polarity in APBs in the centrosymmetric PZ. As the observed polarity is the result of spontaneous symmetry breaking, the phenomenon observed at the APB is a signature of local ferroelectricity. This is supported by first principle calculations which reveals the bi-stability of the polarity at the APB. Although the switchability of the polarity was not demonstrated, the moderate values of the spontaneous polarization found in the APB suggest moderate values of its thermodynamic coercive field, which behaves as the cube of spontaneous polarization [116], promising that the polarity is not only bistable but also switchable.

The polar antiphase domain boundaries studied above are expected to be bistable and mobile.

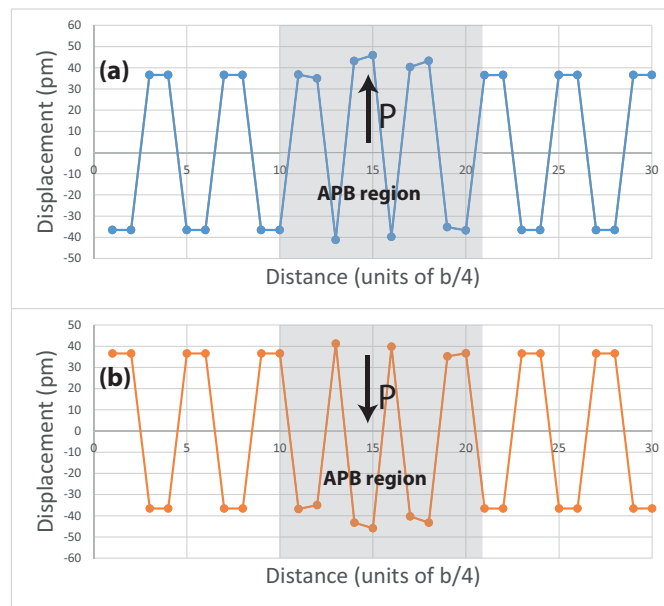


Figure 6.10: Pb atom displacements from cubic positions along [100] direction in the APB region. There are 2 equivalent configurations (a) and (b) corresponding to the same energy confirming the bistability of the structure.

The bistability of polar domain walls in a non-polar material is readily expected in view of the symmetry arguments. Understanding the mobility of the APBs is less evident. Since translational domains are identical in terms of all materials tensors no macroscopic stimulus can change the energy of the domains. However, under electric field, \vec{E} , the dipole moment density in the wall is associated with the energy density $-\vec{P}\vec{E}$. This implies force acting on the wall once the electric field is inhomogeneous, e.g. when electric field gradient is applied across the wall.

Ferroelectric antiphase domain boundaries in antiferroelectrics can be viewed as functional elements, 1-10 nm wide, which carry information. Unlike twin domain walls, the polar translational walls are non-ferroelastic, which makes them strain-free, thus even more appealing for potential information-carrying elements. In comparison with the attractive magnetic domain-wall memory [120], they do not require current for operation and are an order of magnitude thinner, thus adding potentially a new element for future high-density information storage.

7 Conclusions and Outlook

7.1 Conclusions

This work points out to the importance of high-order electromechanical couplings in the physics of ferroelectrics. Until recently, only the piezoelectric and low-order electrostrictive electromechanical couplings were taken into account in the physical models and used into the devices. However, the recent developments in the field have revealed that the high-order electromechanical couplings and corresponding electromechanical effects become increasingly important. High-order electromechanical couplings can be roughly divided into two groups, the non-linear electrostrictive couplings and couplings related to the flexoelectric effect.

It was shown that an adequate Landau theory treatment of thermodynamics of ferroelectric thin films requires taking into account high-order electromechanical couplings and non-linear elasticity. The high-order electromechanical couplings were for the first time calculated for classical ferroelectric crystal of BTO, using first principles methods. The above analysis suggests that all Landau theory based simulation of ferroelectric thin films should take into account not only customarily incorporated ordinary electrostriction coupling, but also the high-order electromechanical interactions.

A high-order electrostrictive coefficients are important for antiresonance frequency tuning of tunable FBARs. The high-order electrostrictive coefficients for BTO and STO materials were, for the first time, calculated using ab initio methods. Since the obtained values were found close to each other for the both materials, we determined the m_{111} coefficient for BST compositions using a linear interpolation. Based on the results obtained with first principles calculations, we simulated the resonance and antiresonance tuning of the BST based tunable FBARs. It was established that there is a compensation of linear and non-linear electrostrictive contributions to the antiresonance tuning which leads to the fact that the tuning was found to be smaller than expected from previously made estimations.

It was shown that classical cubic perovskite ferroelectrics exhibit deviations from the "ex-

tension along the field and contraction perpendicular to it" behaviour if the sample is cut obliquely to the cubic crystallographic directions. Specifically, a remarkable behaviour along the [111] crystallographic cubic direction is predicted for the perovskite in the paraelectric phase. In this case, an electric field parallel to [111] direction causes a expansion along all its three dimensions of the sample. This phenomenon may be of interest for actuators based on the electrostrictive effect, transducers, and detectors.

There exist a manifestation of the angular dependance of electrostriction in the phase diagrams of ferroelectric thin films. It was found that there is a shift of the phase transition temperature depending on the film orientation. Remarkably, for some film orientations, a compressive strain does not always increase T_C . Depending on the film orientation the phase transition temperature can be less than that in the bulk material. The use of differently orientated thin films provides a broader range of operating temperatures for thin film based devices, which allows more flexibility for engineering.

Then, the flexoelectric effect with the example of STO was studied using the analysis of phonon dispersion and microscopic lattice dynamics. The phonon dispersion curves as well as microscopic parameters (IFCs) were obtained using first principles calculations for cubic STO. The structure was stabilized by applied pressure, since cubic STO material is unstable within first principles methods using GGA, which is actually an expected behaviour. Moreover, varying the pressure, it is possible to greatly change the dielectric constant of the material providing an analog to Curie-Weiss law.

To calculate static and dynamic flexoelectric tensors two methods were used. The first method represents the analysis of phonon dispersion curves. It gives f and M tensors within the sign ambiguity and it is not able to resolve the $f_{11} - f_{12}$ difference. The obtained values are in a qualitative agreement with previously made estimations. The considered analysis can be used with real experimental data of phonon dispersion to find flexoelectric coefficients. The second method uses microscopic parameters of the material, i.e. IFC. This method can, in principle, provides all components of f and M tensors. With this method the dynamic flexoelectric coefficient was for the first time calculated for STO. As expected, M has a significant contribution to f^{tot} and, therefore, should be taken into account. However, it was shown the standard precision of such calculations is not enough to find f tensor.

Being mainly focused on DFT calculations of ferroelectrics, the thesis also contains first principles study of domain boundaries of antiferroelectric PZ. Using DFT full relaxation calculations it was shown that translational antiphase boundaries in antiferroelectric PZ possess local polarity. The bistability of polar domain walls in a non-polar material, which was expected in view of the symmetry arguments, was also established. Hence, the ab initio calculations showed both, the presence of local polarity, and the possibility of polarization switching, supporting the ferroelectric nature of APB. Ferroelectric translational antiphase boundaries could make a new type of non-volatile memory. In comparison with the attractive magnetic domain-wall memory, they do not require current for operation and are an order

of magnitude thinner, adding potentially a new element for future high-density information storage.

7.2 Outlook

We have showed the importance of high-order electromechanical couplings for ferroelectric materials. In view of our findings, an experimental evaluation of high-order electromechanical couplings in ferroelectrics seems to be a task of primary importance. There are several obstacles which complicate the evaluation of the high-order electromechanical coefficients using ab initio methods. Namely, one often needs a high precision of calculations. To reliably calculate high-order electrostrictive coefficients, the full relaxation DFT calculations should be done with a good accuracy. The calculations of flexoelectric tensors requires a very dense mesh of q-point to be able to plot phonon spectrum with the correct behaviour near the Γ -point.

Bibliography

- [1] N. A. Pertsev, Z. G. Zembilgotov, and A. K. Tagantsev. Equilibrium states and phase transitions in epitaxial ferroelectric thin films. *Ferroelectrics*, 223(1-4):79–90, 1999.
- [2] A. Gruverman, B. J. Rodriguez, A. I. Kingon, R. J. Nemanich, A. K. Tagantsev, J. S. Cross, and M. Tsukada. Mechanical stress effect on imprint behavior of integrated ferroelectric capacitors. *Applied Physics Letters*, 83(4):728–730, 2003.
- [3] John Y. Fu, Wenyi Zhu, Nan Li, Nadine B. Smith, and L. Eric Cross. Gradient scaling phenomenon in microsize flexoelectric piezoelectric composites. *Applied Physics Letters*, 91(18), 2007.
- [4] O. G. Vendik, S. P. Zubko, and M. A. Nikol'ski. Microwave loss-factor of $\text{Ba}_x\text{Sr}_{1-x}\text{TiO}_3$ as a function of temperature, biasing field, barium concentration, and frequency. *Journal of Applied Physics*, 92(12):7448–7452, 2002.
- [5] Tomoaki Yamada. Electromechanical properties of oxygen-octahedra ferroelectric crystals. *Journal of Applied Physics*, 43(2):328–338, 1972.
- [6] Alexander K. Tagantsev, Eric Courtens, and Ludovic Arzel. Prediction of a low-temperature ferroelectric instability in antiphase domain boundaries of strontium titanate. *Phys. Rev. B*, 64:224107, 2001.
- [7] M. Adachi, Y. Akishige, T. Asahi, K. Deguchi, K. Gesi, K. Hasebe, T. Hikita, T. Ikeda, and Y. Iwata. *Landolt-Bornstein, Numerical Data and Functional Relationships in Science and Technology, New Series*, volume III/36, Ferroelectrics and Related Substances: Oxides. Springer-Verlag, Berlin Heidelberg New-York, 2001.
- [8] J. D. Axe, J. Harada, and G. Shirane. Anomalous acoustic dispersion in centrosymmetric crystals with soft optic phonons. *Phys. Rev. B*, 1:1227–1234, Feb 1970.
- [9] Don Berlincourt and Hans Jaffe. Elastic and piezoelectric coefficients of single-crystal barium titanate. *Phys. Rev.*, 111:143–148, 1958.
- [10] HF Kay and P Vousden. Symmetry changes in barium titanate at low temperatures and their relation to its ferroelectric properties. *Philosophical Magazine*, 40(309):1019–1040, 1949.

Bibliography

- [11] T. Yamada. Electromechanical properties of oxygen-octahedra ferroelectric crystals. *Journal of Applied Physics*, 43(2):328–338, 1972.
- [12] K. Uchino. *Ferroelectric Devices*. Marcel Decker, New York, 2000.
- [13] P. Muralt, R. G. Polcawich, and S. Trolier-McKinstry. Piezoelectric thin films for sensors, actuators, and energy harvesting. *Mrs Bulletin*, 34(9):658–664, 2009.
- [14] Y. B. Jeon, R. Sood, J. H. Jeong, and S. G. Kim. Mems power generator with transverse mode thin film pzt. *Sensors and Actuators a-Physical*, 122(1):16–22, 2005.
- [15] Alexander K. Tagantsev, Vincent Meunier, and Pradeep Sharma. Novel electromechanical phenomena at the nanoscale: Phenomenological theory and atomistic modeling. *Mrs Bulletin*, 34(9):643–647, 2009.
- [16] Nikolai K. Yushin. Nonlinear electroacoustical effect in ferroelectrics. *Ferroelectrics*, 175(1):251–260, 1996.
- [17] N. A. Pertsev, A. G. Zembilgotov, and A. K. Tagantsev. Effect of mechanical boundary conditions on phase diagrams of epitaxial ferroelectric thin films. *Physical Review Letters*, 80(9):1988–1991, 1998.
- [18] N. A. Pertsev, A. K. Tagantsev, and N. Setter. Phase transitions and strain-induced ferroelectricity in srtio3 epitaxial thin films. *Physical Review B*, 61(2):R825–R829, 2000.
- [19] J. H. Haeni, P. Irvin, W. Chang, R. Uecker, P. Reiche, Y. L. Li, S. Choudhury, W. Tian, M. E. Hawley, B. Craigo, A. K. Tagantsev, X. Q. Pan, S. K. Streiffer, L. Q. Chen, S. W. Kirchoefer, J. Levy, and D. G. Schlom. Room-temperature ferroelectricity in strained SrTiO₃. *Nature*, 430(7001):758–761, 2004.
- [20] A. K. Tagantsev, N. A. Pertsev, P. Muralt, and N. Setter. Strain-induced diffuse dielectric anomaly and critical point in perovskite ferroelectric thin films. *Phys. Rev. B*, 65:012104, 2001.
- [21] S Gevorgian, T Lewin, H Jacobsson, and A Vorobiev. A tunable resonator, 2006. Patent Pub. No.: WO/2006/004470, International Application No.: PCT/SE2004/001099.
- [22] Irina B. Vendik, Pavel A. Turalchuk, Orest G. Vendik, and John Berge. Modeling tunable bulk acoustic resonators based on induced piezoelectric effect in BaTiO₃ and Ba_{0.25}Sr_{0.75}TiO₃ films. *Journal of Applied Physics*, 103(1):014107, 2008.
- [23] Andreas Noeth, Tomoaki Yamada, Alexander K. Tagantsev, and Nava Setter. Electrical tuning of dc bias induced acoustic resonances in paraelectric thin films. *Journal of Applied Physics*, 104(9):094102, 2008.
- [24] P. V. Yudin and A. K. Tagantsev. Fundamentals of flexoelectricity in solids. *Nanotechnology*, 24(43), 2013.

- [25] S. M. Kogan. Piezoelectric effect during inhomogeneous deformation and acoustic scattering of carriers in crystals. *Soviet Physics-Solid State*, 5(10):2069–2070, 1964.
- [26] A. K. Tagantsev. Electric polarization in crystals and its response to thermal and elastic perturbations. *Phase Transitions*, 35(3-4):119–203, 1991.
- [27] E V Bursian and O I Zaikovskii. Changes in the curvature of a ferroelectric film due to polarization. *Sov. Phys. - Solid State*, 10:1121, 1968.
- [28] E V Bursian and Trunov N N. Nonlocal piezoelectric effect. *Sov. Phys. - Solid State*, 10: 760, 1974.
- [29] L. E. Cross. Flexoelectric effects: Charge separation in insulating solids subjected to elastic strain gradients. *Journal of Materials Science*, 41(1):53–63, 2006.
- [30] John Y. Fu, Wenyi Zhu, Nan Li, and L. Eric Cross. Experimental studies of the converse flexoelectric effect induced by inhomogeneous electric field in a barium strontium titanate composition. *Journal of Applied Physics*, 100(2), 2006.
- [31] P. Zubko, G. Catalan, A. Buckley, P. R. L. Welche, and J. F. Scott. Strain-gradient-induced polarization in SrTiO₃ single crystals. *Physical Review Letters*, 99(16), 2007.
- [32] H. Lu, C.-W. Bark, D. Esque de los Ojos, J. Alcala, C. B. Eom, G. Catalan, and A. Gruverman. Mechanical writing of ferroelectric polarization. *Science*, 336(6077):59–61, 2012.
- [33] N. D. Sharma, R. Maranganti, and P. Sharma. On the possibility of piezoelectric nanocomposites without using piezoelectric materials. *Journal of the Mechanics and Physics of Solids*, 55(11):2328–2350, 2007.
- [34] M. S. Majdoub, P. Sharma, and T. Cagin. Enhanced size-dependent piezoelectricity and elasticity in nanostructures due to the flexoelectric effect. *Physical Review B*, 77(12), 2008.
- [35] R. Maranganti and P. Sharma. Atomistic determination of flexoelectric properties of crystalline dielectrics. *Phys. Rev. B*, 80:054109, Aug 2009.
- [36] A. K. Tagantsev. Piezoelectricity and flexoelectricity in crystalline dielectrics. *Phys. Rev. B*, 34:5883–5889, Oct 1986.
- [37] Jiawang Hong, G Catalan, J F Scott, and E Artacho. The flexoelectricity of barium and strontium titanates from first principles. *Journal of Physics: Condensed Matter*, 22(11): 112201, 2010.
- [38] I. Ponomareva, A. K. Tagantsev, and L. Bellaiche. Finite-temperature flexoelectricity in ferroelectric thin films from first principles. *Phys. Rev. B*, 85:104101, Mar 2012.
- [39] Jiawang Hong and David Vanderbilt. First-principles theory of frozen-ion flexoelectricity. *Phys. Rev. B*, 84:180101, Nov 2011.

Bibliography

- [40] Massimiliano Stengel. Flexoelectricity from density-functional perturbation theory. *Phys. Rev. B*, 88:174106, Nov 2013.
- [41] Richard M. Martin. Piezoelectricity. *Phys. Rev. B*, 5:1607–1613, Feb 1972.
- [42] Raffaele Resta. Towards a bulk theory of flexoelectricity. *Phys. Rev. Lett.*, 105:127601, Sep 2010.
- [43] Traian Dumitrica, Chad M. Landis, and Boris I. Yakobson. Curvature-induced polarization in carbon nanoshells. *Chemical Physics Letters*, 360(1–2):182 – 188, 2002. ISSN 0009-2614.
- [44] Sergei V. Kalinin and Vincent Meunier. Electronic flexoelectricity in low-dimensional systems. *Phys. Rev. B*, 77:033403, Jan 2008.
- [45] Alexander K. Tagantsev and Alexander S. Yurkov. Flexoelectric effect in finite samples. *Journal of Applied Physics*, 112(4):044103, 2012.
- [46] V L Indenbom, E B Loginov, and M A Osipov. Flexoelectric effect and the structure of crystals. *Kristallografija*, 26:1157, 1998.
- [47] Eugene A. Eliseev, Anna N. Morozovska, Maya D. Glinchuk, and R. Blinc. Spontaneous flexoelectric/flexomagnetic effect in nanoferroics. *Phys. Rev. B*, 79:165433, Apr 2009.
- [48] Tagantsev A K. Theory of flexoelectric effects in crystals. *Journal of Experimental and Theoretical Physics*, 88:2108, 1985.
- [49] Y. L. Li, S. Y. Hu, Z. K. Liu, and L. Q. Chen. Phase-field model of domain structures in ferroelectric thin films. *Applied Physics Letters*, 78(24):3878–3880, 2001.
- [50] Oswaldo Diéguez, Silvia Tinte, A. Antons, Claudia Bungaro, J. B. Neaton, Karin M. Rabe, and David Vanderbilt. *Ab initio* study of the phase diagram of epitaxial BaTiO₃. *Phys. Rev. B*, 69:212101, 2004.
- [51] V. G. Koukhar, N. A. Pertsev, and R. Waser. Thermodynamic theory of epitaxial ferroelectric thin films with dense domain structures. *Phys. Rev. B*, 64:214103, 2001.
- [52] K. J. Choi, M. Biegalski, Y. L. Li, A. Sharan, J. Schubert, R. Uecker, P. Reiche, Y. B. Chen, X. Q. Pan, V. Gopalan, L. Q. Chen, D. G. Schlom, and C. B. Eom. Enhancement of ferroelectricity in strained BaTiO₃ thin films. *Science*, 306(5698):1005–1009, 2004.
- [53] J. F. Nye. *Physical Properties of Crystals*. Oxford University Press, USA, 1985.
- [54] G. Kresse and J. Furthmuller. Efficient iterative schemes for ab initio total-energy calculations using a plane-wave basis set. *Physical Review B*, 54(16):11169–11186, 1996.
- [55] John P. Perdew, J. A. Chevary, S. H. Vosko, Koblar A. Jackson, Mark R. Pederson, D. J. Singh, and Carlos Fiolhais. Atoms, molecules, solids, and surfaces: Applications of the generalized gradient approximation for exchange and correlation. *Phys. Rev. B*, 46: 6671–6687, Sep 1992.

- [56] G. Kresse and D. Joubert. From ultrasoft pseudopotentials to the projector augmented-wave method. *Physical Review B*, 59(3):1758–1775, 1999.
- [57] H. J. Monkhorst and J. D. Pack. Special points for brillouin-zone integrations. *Physical Review B*, 13(12):5188–5192, 1976.
- [58] Walter J. Merz. The electric and optical behavior of BaTiO₃ single-domain crystals. *Phys. Rev.*, 76:1221–1225, 1949.
- [59] Y. L. Wang, A. K. Tagantsev, D. Damjanovic, N. Setter, V. K. Yarmarkin, A. I. Sokolov, and I. A. Lukyanchuk. Landau thermodynamic potential for BaTiO₃. *Journal of Applied Physics*, 101(10):9, 2007.
- [60] W. Zhong, David Vanderbilt, and K. M. Rabe. Phase transitions in BaTiO₃ from first principles. *Phys. Rev. Lett.*, 73:1861–1864, 1994.
- [61] María-Isabel Rocha-Gaso, Carmen March-Iborra, Ángel Montoya-Baides, and Antonio Arnau-Vives. Surface generated acoustic wave biosensors for the detection of pathogens: A review. *Sensors*, 9(7):5740–5769, 2009.
- [62] Marc-Alexandre Dubois and Paul Muralt. Properties of aluminum nitride thin films for piezoelectric transducers and microwave filter applications. *Applied Physics Letters*, 74(20):3032–3034, 1999.
- [63] Jae Yoeng Park, Hee Chul Lee, and Seong Jong Cheon. Design and fabrication of integrated film bulk acoustic resonator and filter on silicon nitride membrane. *Microwave and Optical Technology Letters*, 48(11):2230–2233, 2006.
- [64] F. Martin, M.-E. Jan, B. Belgacem, M.-A. Dubois, and P. Muralt. Shear mode coupling and properties dispersion in 8ghz range aln thin film bulk acoustic wave (baw) resonator. *Thin Solid Films*, 514(1-2):341 – 343, 2006.
- [65] Ramin Matloub, Alvaro Artieda, Cosmin Sandu, Evgeny Milyutin, and Paul Muralt. Electromechanical properties of Al_{0.9}Sc_{0.1}N thin films evaluated at 2.5 ghz film bulk acoustic resonators. *Applied Physics Letters*, 99(9):092903, 2011.
- [66] Z. Yan, X. Y. Zhou, G. K. H. Pang, T. Zhang, W. L. Liu, J. G. Cheng, Z. T. Song, S. L. Feng, L. H. Lai, J. Z. Chen, and Y. Wang. ZnO-based film bulk acoustic resonator for high sensitivity biosensor applications. *Applied Physics Letters*, 90(14):143503, 2007.
- [67] G. Ferblantier, F. Maily, R. Al Asmar, A. Foucaran, and F. Pascal-Delannoy. Deposition of zinc oxide thin films for application in bulk acoustic wave resonator. *Sensors and Actuators A: Physical*, 122(2):184 – 188, 2005.
- [68] K. Hashimoto. *RF Bulk Acoustic Wave Filters for Communications*. Artech House Microwave Library, Norwood MA, 2009.

Bibliography

- [69] Joshua Zepess Steve Mahon and Mark Andrews. Baw flip-chip switched filter bank delivers dramatic form factor reduction. *High Frequency Electronics*, 7(8):24–28, 2008.
- [70] Spartak Sh. Gevorgian, Alexander K. Tagantsev, and Andrei K. Vorobiev. *Tuneable Film Bulk Acoustic Wave Resonators*. Springer, 2013.
- [71] John Berge, Martin Norling, Andrei Vorobiev, and Spartak Gevorgian. Field and temperature dependent parameters of the dc field induced resonances in $\text{Ba}_x\text{Sr}_{1-x}\text{TiO}_3$ -based tunable thin film bulk acoustic resonators. *Journal of Applied Physics*, 103(6):064508, 2008.
- [72] J. Berge and S. Gevorgian. Tunable bulk acoustic wave resonators based on $\text{Ba}_{0.25}\text{Sr}_{0.75}\text{TiO}_3$ thin films and a $\text{HfO}_2/\text{SiO}_2$ bragg reflector. *Ultrasonics, Ferroelectrics and Frequency Control, IEEE Transactions on*, 58(12):2768–2771, 2011.
- [73] A. Vorobiev and S. Gevorgian. Tunable thin film bulk acoustic wave resonators with improved q-factor. *Applied Physics Letters*, 96(21):212904, 2010.
- [74] Andreas Noeth, Tomoaki Yamada, Vladimir O. Sherman, Paul Mural, Alexander K. Tagantsev, and Nava Setter. Tuning of direct current bias-induced resonances in micro-machined $\text{Ba}_{0.3}\text{Sr}_{0.7}\text{TiO}_3$ thin-film capacitors. *Journal of Applied Physics*, 102(11):114110, 2007.
- [75] E. Defay, N. Ben Hassine, P. Emery, G. Parat, J. Abergel, and A. Devos. Tunability of aluminum nitride acoustic resonators: a phenomenological approach. *Ultrasonics, Ferroelectrics and Frequency Control, IEEE Transactions on*, 58(12):2516–2520, 2011.
- [76] O.G. Vendik, E.K. Hollmann, A.B. Kozyrev, and A.M. Prudan. Ferroelectric tuning of planar and bulk microwave devices. *Journal of Superconductivity*, 12:325–338, 1999.
- [77] J. F. Rosenbaum. *Bulk Acoustic Wave Theory and Devices*. Artech House, 1988.
- [78] Paolo Giannozzi, Stefano Baroni, Nicola Bonini, Matteo Calandra, Roberto Car, Carlo Cavazzoni, Davide Ceresoli, Guido L Chiarotti, Matteo Cococcioni, Ismaila Dabo, Andrea Dal Corso, Stefano de Gironcoli, Stefano Fabris, Guido Fratesi, Ralph Gebauer, Uwe Gerstmann, Christos Gougousis, Anton Kokalj, Michele Lazzeri, Layla Martin-Samos, Nicola Marzari, Francesco Mauri, Riccardo Mazzarello, Stefano Paolini, Alfredo Pasquarello, Lorenzo Paulatto, Carlo Sbraccia, Sandro Scandolo, Gabriele Sclauzero, Ari P Seitsonen, Alexander Smogunov, Paolo Umari, and Renata M Wentzcovitch. Quantum espresso: a modular and open-source software project for quantum simulations of materials. *Journal of Physics: Condensed Matter*, 21(39):395502 (19pp), 2009.
- [79] John P. Perdew, Kieron Burke, and Matthias Ernzerhof. Generalized gradient approximation made simple. *Phys. Rev. Lett.*, 77:3865–3868, 1996.
- [80] David Vanderbilt. Soft self-consistent pseudopotentials in a generalized eigenvalue formalism. *Phys. Rev. B*, 41:7892–7895, 1990.

- [81] A. Noeth, T. Yamada, A.K. Tagantsev, and N. Setter. Effect of mechanical loading on the tuning of acoustic resonances in BST thin films. *Journal of Electroceramics*, 24:237–244, 2010.
- [82] R Lakes. Foam structures with a negative poissons ratio. *Science*, 235(4792):1038–1040, 1987.
- [83] RH Baughman, JM Shacklette, AA Zakhidov, and S Stafstrom. Negative Poisson’s ratios as a common feature of cubic metals. *Nature*, 392(6674):362–365, 1998.
- [84] A Yeganehhaeri, DJ Weidner, and JB Parise. Elasticity of alpha-cristobalite - a silicon dioxide with a negative poissons ratio. *Science*, 257(5070):650–652, 1992.
- [85] Zachary G. Nicolaou and Adilson E. Motter. Mechanical metamaterials with negative compressibility transitions. *Nature Materials*, 11:608 – 613, 2012.
- [86] Darrell G. Schlom, Long-Qing Chen, Chang-Beom Eom, Karin M. Rabe, Stephen K. Streiffer, and Jean-Marc Triscone. Strain tuning of ferroelectric thin films. *Annual Review of Materials Research*, 37:589–626, 2007.
- [87] G. N. Saddik, D. S. Boesch, S. Stemmer, and R. A. York. dc electric field tunable bulk acoustic wave solidly mounted resonator using SrTiO₃. *Applied Physics Letters*, 91(4): 043501, 2007.
- [88] John Berge, Andrei Vorobiev, William Steichen, and Spartak Gevorgian. Tunable solidly mounted thin film bulk acoustic resonators based on Ba_xSr_{1-x}TiO₃ films. *IEEE Microwave and Wireless Components Letters*, 17(9):655–657, 2007.
- [89] E Fukada. History and recent progress in piezoelectric polymers. *IEEE Transactions on Ultrasonics, Ferroelectrics, and Frequency Control*, 47(6):1277–1290, 2000.
- [90] VV Kochervinskii. Piezoelectricity in crystallizing ferroelectric polymers: Poly(vinylidene fluoride) and its copolymers (A review). *Crystallography Reports*, 48(4):649 – 675, 2003.
- [91] Huaping Wu, Aiping Liu, Linzhi Wu, and Shanyi Du. Orientation dependence of dielectric behavior of ferroelectric bilayers and multilayers. *Applied Physics Letters*, 93:242909, 2008.
- [92] J. Wang, J. B. Neaton, H. Zheng, V. Nagarajan, S. B. Ogale, B. Liu, D. Viehland, V. Vaithyanathan, D. G. Schlom, U. V. Waghmare, N. A. Spaldin, K. M. Rabe, M. Wuttig, and R. Ramesh. Epitaxial BiFeO₃ multiferroic thin film heterostructures. *Science*, 299 (5613):1719–1722, 2003.
- [93] G. Shirane, J. D. Axe, J. Harada, and J. P. Remeika. Soft ferroelectric modes in lead titanate. *Phys. Rev. B*, 2:155–159, Jul 1970.

Bibliography

- [94] B. Hehlen, L. Arzel, A. K. Tagantsev, E. Courtens, Y. Inaba, A. Yamanaka, and K. Inoue. Brillouin-scattering observation of the ta-to coupling in SrTiO₃. *Phys. Rev. B*, 57:R13989–R13992, Jun 1998.
- [95] A. Yamanaka, M. Kataoka, Y. Inaba, K. Inoue, B. Hehlen, and E. Courtens. Evidence for competing orderings in strontium titanate from hyper-raman scattering spectroscopy. *Europhysics Letters*, 50(5):688–694, 2000.
- [96] V. G. Vaks. *Introduction into Microscopic Theory of Ferroelectrics*. Nauka, Moscow, 1973.
- [97] M Born and K Huang. *Dynamical Theory of Crystal Lattices*. Oxford University Press, Oxford, 1962.
- [98] Xian-Kui Wei, Alexander K. Tagantsev, Alexander Kvasov, Krystian Roleder, Chun-Lin Jia, and Nava Setter. Ferroelectric translational antiphase boundaries in nonpolar materials. *Nature Communications*, 5(3031), 2014.
- [99] J. Seidel, L. W. Martin, Q. He, Q. Zhan, Y. H. Chu, A. Rother, M. E. Hawkrigde, P. Maksymovych, P. Yu, M. Gajek, N. Balke, S. V. Kalinin, S. Gemming, F. Wang, G. Catalan, J. F. Scott, N. A. Spaldin, J. Orenstein, and R. Ramesh. Conduction at domain walls in oxide multiferroics. *Nature Materials*, 8(3):229–234, 2009.
- [100] S. Farokhipoor and B. Noheda. Conduction through 71 degrees domainwalls in BiFeO₃ thin films. *Physical Review Letters*, 107(12):127601, 2011.
- [101] Peter Maksymovych, Anna N. Morozovska, Pu Yu, Eugene A. Eliseev, Ying-Hao Chu, Ramamoorthy Ramesh, Arthur P. Baddorf, and Sergei V. Kalinin. Tunable metallic conductance in ferroelectric nanodomains. *Nano Letters*, 12(1):209–213, 2012.
- [102] D. Meier, J. Seidel, A. Cano, K. Delaney, Y. Kumagai, M. Mostovoy, N. A. Spaldin, R. Ramesh, and M. Fiebig. Anisotropic conductance at improper ferroelectric domain walls. *Nature Materials*, 11(4):284–288, 2012.
- [103] Tomas Sluka, Alexander K. Tagantsev, Petr Bednyakov, and Nava Setter. Free-electron gas at charged domain walls in insulating BaTiO₃. *Nature communications*, 4:1808, 2013.
- [104] S. Y. Yang, J. Seidel, S. J. Byrnes, P. Shafer, C. H. Yang, M. D. Rossell, P. Yu, Y. H. Chu, J. F. Scott, III Ager, J. W., L. W. Martin, and R. Ramesh. Above-bandgap voltages from ferroelectric photovoltaic devices. *Nature Nanotechnology*, 5(2):143–147, 2010.
- [105] Sandra Van Aert, Stuart Turner, Remi Delville, Dominique Schryvers, Gustaaf Van Tendeloo, and Ekhard K. H. Salje. Direct observation of ferrielectricity at ferroelastic domain boundaries in CaTiO₃ by electron microscopy. *Advanced Materials*, 24(4):523, 2012.
- [106] C. L. Jia, M. Lentzen, and K. Urban. Atomic-resolution imaging of oxygen in perovskite ceramics. *Science*, 299(5608):870–873, 2003.

- [107] G. Shirane, E. Sawaguchi, and Y. Takagi. Dielectric properties of lead zirconate. *Physical Review*, 84(3):476–481, 1951.
- [108] V. A. Isupov. Ferroelectric and antiferroelectric perovskites $\text{PbB}'_{0.5}\text{B}''_{0.5}\text{O}_3$. *Ferroelectrics*, 289:131–195, 2003.
- [109] Xiaoli Tan, Cheng Ma, Joshua Frederick, Sarah Beckman, and Kyle G. Webber. The anti-ferroelectric \leftrightarrow ferroelectric phase transition in lead-containing and lead-free perovskite ceramics. *Journal of the American Ceramic Society*, 94(12):4091–4107, 2011.
- [110] A. K. Tagantsev, K. Vaideeswaran, S. B. Vakhrushev, A. V. Filimonov, R. G. Burkovsky, A. Shaganov, D. Andronikova, A. I. Rudskoy, A. Q. R. Baron, H. Uchiyama, D. Chernyshov, A. Bosak, Z. Ujma, K. Roleder, A. Majchrowski, J. H. Ko, and N. Setter. The origin of antiferroelectricity in PbZrO_3 . *Nature Communications*, 4:2229, 2013.
- [111] L. E. Cross. A thermodynamic treatment of ferroelectricity and antiferroelectricity in pseudo-cubic dielectrics. *Philosophical Magazine*, 1(1):76–92, 1956.
- [112] K. Okada. Phenomenological theory of antiferroelectric transition. i. second-order transition. *Journal of the Physical Society of Japan*, 27(2):420, 1969.
- [113] E. V. Balashova and A. K. Tagantsev. Polarization response of crystals with structural and ferroelectric instabilities. *Physical Review B*, 48(14):9979–9986, 1993.
- [114] T. Ostapchuk, J. Petzelt, V. Zelezny, S. Kamba, V. Bovtun, V. Porokhonsky, A. Pashkin, P. Kuzel, M. D. Glinchuk, I. P. Bykov, B. Gorshunov, and M. Dressel. Polar phonons and central mode in antiferroelectric PbZrO_3 ceramics. *Journal of Physics-Condensed Matter*, 13(11):2677–2689, 2001.
- [115] R. A. Cowley. Lattice dynamics and phase transitions of strontium titanate. *Physical Review a-General Physics*, 134(4A):A981, 1964.
- [116] A. K. Tagantsev, L. E. Cross, and Fousek. *Domains in ferroic crystals and thin films*. Springer, New York, 2010.
- [117] A. Fouskova and K. Fousek. Continuum theory of domain walls $\text{Gd}_2(\text{MoO}_4)_3$. *Phys. Stat. Sol. (a)*, 32:213, 1975.
- [118] D. L. Corker, A. M. Glazer, J. Dec, K. Roleder, and R. W. Whatmore. A re-investigation of the crystal structure of the perovskite PbZrO_3 by x-ray and neutron diffraction. *Acta Cryst.*, B53:135–142, 1997.
- [119] U. V. Waghmare and K. M. Rabe. Lattice instabilities, anharmonicity and phase transitions in PbZrO_3 from first principles. *Ferroelectrics*, 194:135–147, 1997.
- [120] Stuart S. P. Parkin, Masamitsu Hayashi, and Luc Thomas. Magnetic domain-wall race-track memory. *Science*, 320(5873):190–194, 2008.

List of publications

- [1] A.A. Kvasov, Yu.F. Markov, E.M. Roginskii, and M.B. Smirnov. Acoustic and optical phonons and their dispersion in model ferroelastics Hg_2Cl_2 . *Physics of the Solid State*, 51(7):1349–1352, 2009.
- [2] Michael A. Reshchikov, Alexander A. Kvasov, Marilyn F. Bishop, Tom McMullen, Alexander Usikov, Vitali Soukhoveev, and Vladimir A. Dmitriev. Tunable and abrupt thermal quenching of photoluminescence in high-resistivity Zn-doped GaN. *Physical Review B*, 84(7), 2011.
- [3] Alexander Kvasov and Alexander K. Tagantsev. Positive effective Q_{12} electrostrictive coefficient in perovskites. *Journal of Applied Physics*, 112(9), 2012.
- [4] E. M. Roginskii, A. A. Kvasov, Yu F. Markov, and M. B. Smirnov. Lattice dynamics and phonon dispersion in Hg_2Br_2 model ferroelastic crystals. *Technical Physics Letters*, 38(4): 361–364, 2012.
- [5] E. M. Roginskii, A. A. Kvasov, Yu F. Markov, and M. B. Smirnov. Phonons and their dispersion in model ferroelastics Hg_2Hal_2 . *Physics of the Solid State*, 54(5):900–904, 2012.
- [6] E. M. Roginskii, A. A. Kvasov, Yu F. Markov, and M. B. Smirnov. Dispersion of phonons and their pressure behavior in model ferroelastic Hg_2I_2 . *Ferroelectrics*, 444(1):33–39, 2013.
- [7] E. M. Roginskii, A. A. Kvasov, Yu F. Markov, and M. B. Smirnov. Lattice dynamics, force constants, and phonon dispersion in model ferroelastics Hg_2I_2 . *Technical Physics Letters*, 39(5):413–417, 2013.
- [8] Alexander Kvasov and Alexander K. Tagantsev. Role of high-order electromechanical coupling terms in thermodynamics of ferroelectric thin films. *Physical Review B*, 87(18), 2013.
- [9] Alexander Kvasov and Alexander K. Tagantsev. Thin film bulk acoustic wave resonators tuning from first principles. *Journal of Applied Physics*, 113(20), 2013.
- [10] Xian-Kui Wei, Alexander K. Tagantsev, Alexander Kvasov, Krystian Roleder, Chun-Lin Jia, and Nava Setter. Ferroelectric translational antiphase boundaries in nonpolar materials. *Nature Communications*, 5(3031), 2014.

Curriculum Vitae

Alexander Kvasov

[École Polytechnique Fédérale de Lausanne](#)

[Ceramics Laboratory](#)



Contact information

- Address: Chemin du Bochet 25, 1025 Saint-Sulpice, Switzerland
- Office phone: +41 21 693 5805
- Mobile phone: +41 78 7967047
- E-mail: alex.kvasov@gmail.com, alexander.kvasov@epfl.ch

Personal information

- Born: 16.02.1986, Leningrad, Russia
- Nationality: Russian
- Sex: male
- Marital status: single

Education

- 2010 – present: PhD at [École Polytechnique Fédérale de Lausanne](#), research assistant
- 2006 – 2010: research assistant at [A. F. Ioffe Physical-Technical Institute](#) of the Russian Academy of Sciences, Saint-Petersburg, Russia

Duties: work in Dr. Markov's lab, research, computation and modelling of crystals series Hg_2Hal_2 (Hal = Cl, Br, I): phonon dispersion curves, phonon density of states, sound velocity, elastic coefficients.

- 2007 – 2010 – graduate student of [Saint-Petersburg State University](#), [Department of Physics](#), Solid State Physics Division, Saint-Petersburg, Russia

January 2010 – Master's degree (master's thesis – “Dynamic properties of Hg_2Hal_2 (Hal = Cl, Br, I) crystals”)

- spring 2008, spring 2009 – research assistant appointment at [Virginia Commonwealth University](#), [Department of Physics](#), Richmond, Virginia, USA

Duties: work in the Dr. Reshchikov's group at Dr. Baski's lab, computation of electronic properties of wide-gap semiconductors GaN, ZnO

- 2003 – 2007 – undergraduate student of [Saint-Petersburg State University](#), [Department of Physics](#), Solid State Physics Division, Saint-Petersburg, Russia (Bachelor's degree with honour)
- 2000 – 2003 – Saint-Petersburg, school 239 specialized in physics and mathematics

Employment

- September 2008 – June 2010: software developer at [NCT Smart card and systems](#), Saint-Petersburg, Russia. Duties: software development for POS-terminals. Languages C, C++.
- May 2007 – March 2008: software developer [CJSC Scientific Instruments](#), Saint-Petersburg, Russia. Duties: 1) software development for X-ray diffractometers, set-up control, data and spectra processing; 2) X-rays registration, X-ray detectors study: gas and semiconductor detectors, CCD detectors and matrices. Languages C, C++.

Research and professional interests

- Materials science, ferroelectrics, thin films
- Modelling, ab initio calculations, IT, software development for physical models, devices and set-ups

Spoken languages

- Russian: native
- English: fluent
- French: fluent